University of Alberta

Ultra Low Frequency Waves and their Association with Magnetic Substorms and Expansion Phase Onset

by

Kyle R. Murphy

A thesis submitted to the Faculty of Graduate Studies and Research
in partial fulfillment of the requirements for the degree of

Master of Science

Physics

Fall 2009
Edmonton, Alberta

Examining Committee

Dr. Ian R. Mann, Physics

Dr. Richard D. Sydora, Physics

Dr. Roger W. Moore, Physics

Dr. Christopher D. Herd, Earth and Atmospheric Sciences

Abstract

This thesis concerns the study of Ultra Low Frequency (ULF) waves during magnetospheric substorms. A wavelet algorithm which characterises magnetic ULF waves during substorm onset is presented. The algorithm is validated by comparing the spatial and temporal location of ULF wave onset to space-based observations of the aurora. It is demonstrated that the onset of ULF wave power expands coherently away from an ionospheric epicentre during the substorm expansion phase.

Further, a case study of the time-domain causality of magnetotail plasma flows and ULF wave Pi2 pulsations is presented. Although highly correlated, it is demonstrated that the plasma flows cannot directly drive the ground magnetic waveforms but may be indirectly linked via a common source.

Finally, results from a statistical study of ULF wave power during onset are presented. It is concluded that there is no statistical difference between historical sub-classifications of ULF waves observed during substorms.

Acknowledgements

I would like to thank my Mom and Dad for their support, and for always being there when I needed someone to talk to.

Thanks to my friends and family, old and new, those who have always been there and those who will always be.

Special thanks to Dr. Jonathan Rae and my supervisor Dr. Ian Mann for their support, guidance, and encouragement, and especially for taking the time to listen. Their roles as both friends and mentors were invaluable in completing this thesis. Thanks to Dr. David Milling and Dr. Clare Watt for helpful discussions and for proofing sections of this thesis, and to the rest of the space physics group and my officemates for a wonderful two years, the odd beer, a good laugh and great friendships.

Finally, I wish to thank NSERC for partial funding throughout this degree.

Table of Contents

List of Figures

List of Tables

List of Abbreviations

ARIMA	autoregressive integrated moving average
ASI	all-sky imager
AWESOME	automated wavelet estimation of substorm onset and magnetic events
BBF	bursty bulk flow
CANMOS	Canadian Magnetic Observatory System
CANOPUS	Canadian Auroral Network for the OPEN Program Unified Study
CARISMA	Canadian Array for Realtime Investigations of Magnetic Activity
CD	current disruption
CPI	Comprehensive Plasma Instrument
CPS	central plasma sheet
DWT	discrete wavelet transform
FA	field aligned
FAC	field aligned current
FB	flow burst
FFT	fast Fourier transform
FGM	fluxgate magnetometer
FLR	field line resonance
FUV	Far-Ultraviolet Imager
GBO	ground-based observatory
GIMA	Geophysical Institute Magnetometer Array
IC	inertial current
IGPP	Institute of Geophysics and Planetary Physics
IMAGE	Imager for Magnetopause-to-Aurora Global Exploration
IMG	interplanetary magnetic field
ISAS	Institute of Space and Astronautical Science
JAXA	Japanese Aerospace and Exploration Agency
LEP	Low Energy Particle Instrument
MGF	Magnetic Field Instrument
MHD	magnetohydrodynamics
MLT	Magnetic local time
NASA	National Aerospace and Space Administration
NENL	near-Earth neutral line
NRCAN	Natural Resources Canada
PSBL	Plasma sheet boundary layer
PSD	power spectral density
SCW	substorm current wedge
SI	Spectrographic Imager
T96	Tsyganenko 96 field model
THEMIS	Time History of Events and Macroscale Interactions During Substorms
TR	transient response
ULF	Ultra Low Frequency
WIC	Wide-band Imaging Camera
WTS	westward travelling surge

List of Symbols

$\boldsymbol{A}$	A matrix
$\alpha_{j,k}$	Wavelet coefficient
$\boldsymbol{B}$	Magnetic Field
β_i	Plasma Beta
β_s	Impulse response coefficient
$C_{\mathrm{k},xy}$	Discrete coherence
c	Speed of light
c_s	Speed of sound
δ	Small amplitude perturbation
d/dt	Total derivative
Δlat	Relative latitude
$\Delta long$	Relative longitude
Δt	Sampling cadence
$\boldsymbol{E}$	Electric Field
e	Fundamental charge of an electron
ε_0	Permittivity of free space
$\boldsymbol{F}$	General Force
F_{k}	Discrete fast Fourier transform
f_{k}	Discrete frequency
γ	Constant
$H_n\,(x_n)$	Discrete Hilbert transform
i	Square root of negative 1
$\boldsymbol{j}$	Current density
j	Frequency wavelet integer
k	Temporal wavelet integer
k	Discrete wave number
$\boldsymbol{k}$	Wave vector
k_B	Boltzmann Constant
L	Characteristic length scale

l	Length of box model magnetosphere
Λ_{lat}	Latitudinal decay scale of PSD
Λ_{long}	Longitudinal decay scale of PSD
λ_D	Debye Length
m	Mass
μ_0	Permeability of free space
N	Length of a time series, integer
n	Discrete time
n_e	Electron number density
η_t	Stationary noise process
ω	Angular frequency
ω_a	Alfvénmode angular frequency
ω_c	Cyclotron frequency
ω_f	Fast mode angular frequency
P	Pressure
‖	Parallel to the magnetic field
⊥	Perpendicular to the magnetic field
φ	Magnetic declination
$\mathcal{P}_k$	Discrete Power
ϕ_n	Discrete Phase
PSD_k	Discrete Power Spectral Density
Q	Constant
q	Charge of an electron
R_M	Magnetic Reynolds number
R_E	Radius of the Earth
$R_\odot$	Radius of the Sun
r_c	Cyclotron radius
s	Lag
σ	Plasma conductivity
σ_α	Standard deviation of the wavelet coefficients
σ_w	Standard deviation of the residuals
T	Temperature

t	Discrete time
τ	Characteristic time scale
Θ	Angle between wave vector and magnetic field
$\boldsymbol{U}$	Generic vector
u	Characteristic velocity
V	Volume of a flux tube
$\boldsymbol{v}$	Velocity
$\boldsymbol{v}_a$	Alfvén velocity
$\boldsymbol{v_D}$	Drift velocity
$\boldsymbol{v_G}$	Gyro velocity
$\boldsymbol{v}_g$	Group velocity
$\boldsymbol{v}_p$	Phase velocity
$v_{\perp \mathrm{x}}$	Bulk plasma velocity perpendicular to the background magnetic field
W	Windowing correction factor
w_j	Wavelet width of the *j* coefficient
x_n	Discrete time series with respect to n
x_R	Location of field line resonance
x_T	Location of turning point
x_t	Discrete time series with respect to t
y_n	Discrete time series with respect to n
y_t	Discrete time series with respect to t

Chapter 1 The Sun-Earth Connection

1.1 Introduction

This thesis concerns the coupling between the output from the Sun, known as the solar wind, and the Earth's magnetosphere; a cavity formed through the interaction of the solar wind with the Earth's magnetic field. Primarily, this thesis concentrates on Ultra Low Frequency (ULF) magnetic waves observed during the onset of magnetospheric substorms; a consequence of solar-terrestrial coupling and the transfer of energy in the Sun-Earth system.

The first and second Chapters of this thesis introduce solar-terrestrial coupling and the magnetospheric substorm and Chapter 3 describes the instruments and analysis used throughout this thesis. Chapter 4 describes and tests three methods for characterising the onset of ULF waves during magnetosphere to determine the most viable method for characterising the ULF response to magnetic substorms. Chapter 5 details the further development of the prevailing method described in Chapter 4 as well as the application and automation of the algorithm for determining the onset and expansion of ULF waves during magnetic substorms. Chapter 6 discusses the relationship between ULF waves and plasma flows in the Earth's magnetotail and Chapter 7 details a statistical study of ULF waves observed during the onset of magnetospheric substorms. Finally Chapter 8 describes future work relating to magnetospheric substorms and ULF waves.

1.2 The Sun and Solar Wind

The Sun is the principal source of energy and driver of natural phenomena occurring on the surface of the Earth (e.g., photosynthesis), within the Earth's atmosphere (e.g., climate) and in near-Earth space (e.g., the aurora). The Sun is located at an average distance of 1.56×10^{11} km away from the Earth, has a radius of 6.96×10^{11} km ($R_{\odot}$),and a mass of approximately 1.99×10^{30} kg. The interior of the Sun is comprised of roughly 90% hydrogen, 10% helium and 0.1% heavier elements (e.g., carbon) by number [*Carroll and Ostlie*, 1996]. Its structure can be divided into three sections: the thermonuclear core, the radiative zone and the convective zone, as shown in Figure 1.1(a).

Nuclear fusion is the main source of energy in the solar interior and this provides the energy source for disturbances throughout the solar system (i.e., auroral phenomena and space weather). Fusion occurs within the solar interior when the compression of the core's constituents under the Sun's gravitational force converts hydrogen to helium via the pp chain. The net reaction of the pp chain converts four hydrogen atoms to one helium atom, two solar neutrinos, and energy as a result of the mass difference between the reactants and products. This energy, produced within the solar core, propagates outward through the sun driving solar activity on the surface of the Sun (e.g., solar flares) as well as space weather throughout the solar system.

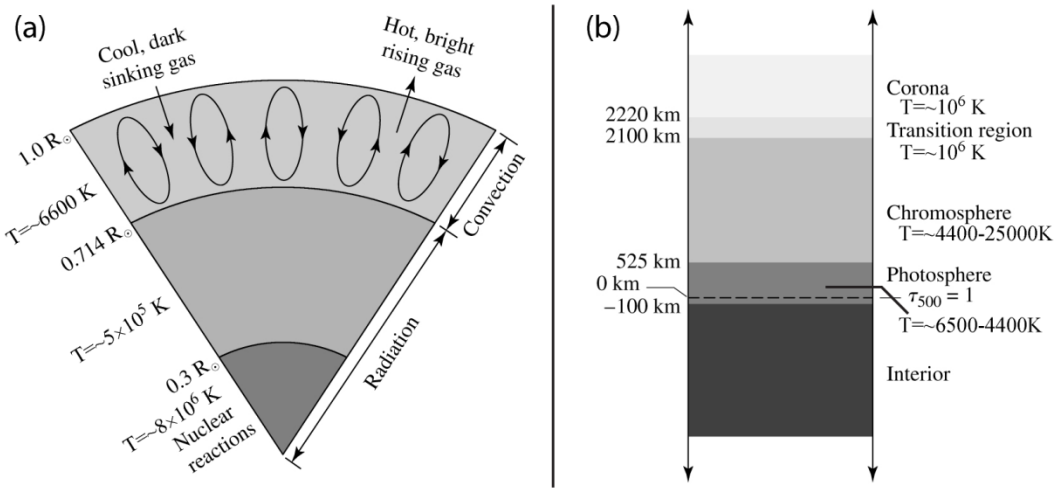

Figure 1.1: Schematic illustrating the regions of (a) the solar interior, and (b) the solar atmosphere. Adapted from Carroll and Ostlie [1996]

In the radiative zone the energy produced in the Sun's thermonuclear core is transported dominantly via the radiative motion of photons and in the convective zone energy is dominantly transported via the convective motion of plasma, the hot ionised gas which composes the sun. The edge of the convective zone lies close to the visible surface of the sun which itself marks the beginning of the solar atmosphere. Moving outward from the surface of the sun the solar atmosphere is divided into four sections, see Figure 1.1(b): the photosphere, where the observed optical photons are generated, the chromosphere, the low density region of the solar atmosphere where the temperature begins to increase with increasing height, the transition region, where the temperature drastically increases over a short distance, and the solar corona, the low-

density and anomalously high-temperature edge of the solar atmosphere. The corona is the region of the Sun's atmosphere which extends deep into the solar system and forms the solar wind which transports energy throughout the solar system.

The solar wind is a magnetised plasma which emanates from the Sun's upper atmosphere and flows into interplanetary space. The existence of a flowing solar wind was first postulated by Parker [1958]. Due to the pressure difference between the Sun's corona and the interplanetary medium, the plasma composing the Sun's outer atmosphere is able to escape the pull of the Sun's gravitational force and expand out into the solar system [*Parker*, 1958]. The solar wind also carries the Sun's magnetic field out into interplanetary space. Similar to the Earth, the Sun generates an internal magnetic field due to flows of plasma in the solar interior acting as a dynamo. Due to the high conductivity of the plasma the Sun's magnetic field is "frozen" to the solar wind (this is referred to as "frozen in flux" and is discussed in more detail in Chapter 2). The magnetic field that is carried by the solar wind is referred to as the Interplanetary Magnetic Field (IMF). Typically, near the orbit of the Earth, the solar wind has similar electron and proton number densities of ~7 cm^{-3} [*Kivelson and Russell*, 1995] and is supersonic (and super-Alfvénic, see Chapter 2, Section 2.4) with two characteristic velocity regimes; the slow solar wind, with velocities less than ~400 km s^{-1}, and the fast solar wind, with velocities of ~500-800 kms^{-1}.

If the Sun were not rotating, the solar wind and the IMF would propagate uniformly in all directions away from the Sun forming a pattern similar to a fluid streaming radially outward. However, due to the Sun's rotation the solar wind and IMF form a more complicated pattern. Plasma emitted from the same point on the sun moves radially outward but remains tied to the magnetic field which has a stationary "footprint" on the surface of the Sun. Thus as the Sun rotates, the IMF in the solar wind begins to form a spiral of expanding plasma and magnetic field; this is referred to as the Parker spiral [*Parker*, 1958], and is depicted in Figure 1.2(a). This spiral pattern is further complicated due to the orientation of the Sun's dipole axis with respect to its rotation axis which are not perfectly aligned. This offset forms a two sector magnetic field pattern in the Parker spiral where adjacent sectors have oppositely oriented magnetic fields, this pattern being analogous to a spinning ballerina skirt, see Figure 1.2(b). Note that in one solar

hemisphere the magnetic field in the solar wind is anti-parallel to the magnetic field in the solar wind protruding from the opposite hemisphere, thus a current sheet forms in approximately the equatorial plane of the solar wind between oppositely directed magnetic fields (where the gradient in magnetic field is large, Figure 1.2(b)).

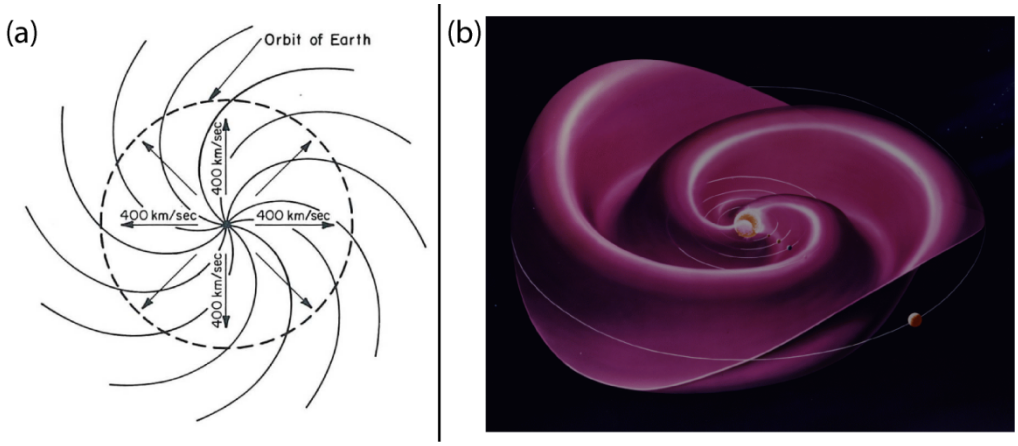

Figure 1.2: (a) Two dimensional schematic of the Parker spiral, adapted from Parker [1958]. (b) Three dimensional schematic of the Parker spiral and heliosperic current, adapted from "http://lepmfi.gsfc.nasa.gov/mfi/hcs/hcs_shape.html".

1.3 The Magnetosphere

If the Earth was isolated in a perfect vacuum, then the Earth's magnetic field would resemble that of a dipole, slightly titled with respect to the equatorial plane as the Earth's rotational and dipole axis are not perfectly aligned. However, interplanetary space is pervaded by both the solar wind and the IMF which interact with the Earth's magnetic field forming a more complicated magnetic topology known as the magnetosphere. When the solar wind impacts the Earth's magnetic field it compresses the day-side magnetic field and is diverted along the flanks onto the night-side. On the night-side of the Earth the diverted solar wind compresses the Earth's magnetic field forming the magnetotail, an elongated cavity which stretches away from the Earth.

When the super-Alfvénic solar wind encounters the Earth's magnetic field it is decelerated and diverted forming a shock upstream from the Earth called the bow shock – the region where the solar wind is heated and decelerated. The outer edge of the magnetosphere is referred to as the magnetopause; this is the boundary separating the

solar wind plasma and IMF from the terrestrial plasma and Earth's magnetic field. The magnetopause boundary is formed at the stagnation point where the solar wind ram and magnetic pressure is balanced by the Earth's magnetic field pressure. Typically the magnetopause forms at a distance of ~10 earth radii (R_E) upstream however during high-speed solar wind flows the solar wind ram pressure increases and the magnetopause boundary forms closer to the Earth. The plasma lying between the bow shock and the magnetopause is the magnetosheath and is in general hotter and denser than the plasma contained in the magnetosphere [*Baumjohann and Treumann*, 1997]. The topology of the magnetosphere and location of the bow shock and magnetosheath are shown schematically in Figure 1.3.

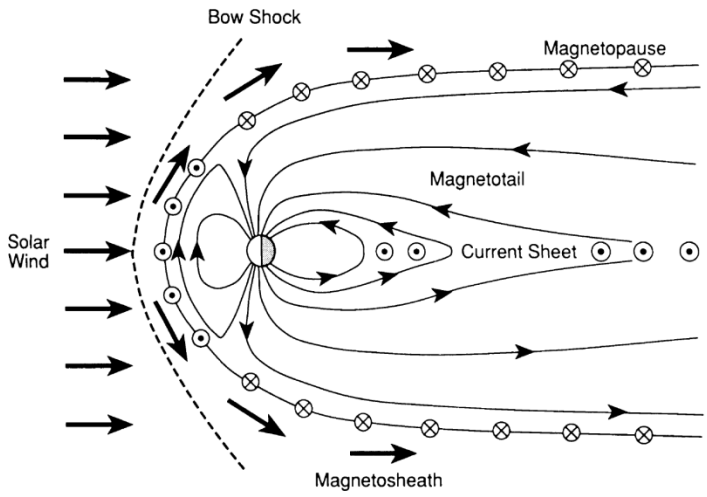

Figure 1.3: Topology of a simple closed magnetosphere. Figure from Kivelson and Russell [1995]

Figure 1.3 illustrates a simple closed magnetosphere where the IMF does not connect with the Earth's magnetic field. In 1961, Dungey proposed an "open" model of the magnetosphere, where the IMF and Earth's magnetic field are able to connect via the process of magnetic reconnection. When the plasma and magnetic field of a particular regime are frozen together they form a boundary where they come into contact with the plasma and magnetic field of another regime (e.g., the solar wind and IMF, and the Earth's magnetosphere). However on small scales the frozen in flux approximation breaks down, and the plasma and magnetic field can decouple such that the magnetic field is able to diffuse through the plasma and undergo magnetic reconnection (see

Chapter 2 for details). In these regions anti-parallel magnetic fields are able to participate in reconnection whereby the magnetic field in one regime is cut and reconnected to the magnetic field from a distinctly separate field regime, forming an entirely new and inter-connected magnetic field topology. Further, in the vicinity of magnetic reconnection plasma is able to diffuse across the previously closed boundary separating the two magnetic field topologies, allowing the exchange of mass, energy and momentum between two previously separate systems.

Figure 1.4 is a schematic of an open magnetosphere [*Dungey*, 1961]. A predominantly southward IMF reconnects with the northward field of the dayside magnetosphere, illustrated by 1 and 1'. This creates two new open magnetic field lines; one emanating from the northern pole and the other from the south, shown as 2 and 2' respectively. The open magnetic field is then dragged by the solar wind from the day-side over the polar cap (region of open field lines) and onto the night-side (positions 3-5 and 3'-5') where the two open field lines once again may take part in reconnection, 6 and 6'. The now closed magnetic field convects into the inner magnetotail along the dawn and dusk flanks and then back to the day side where the process is repeated. The entire process is referred to as the Dungey cycle. The inset of Figure 1.4 depicts the motion of the footprints of magnetic field lines and plasma in the ionosphere, a region of imperfectly conducting plasma at altitudes between ~80 and 1000 km (see Section 1.4). The shaded region is referred to as the auroral zone, or the auroral oval, whilst the boundary between the polar cap and auroral oval represent the open-closed field line boundary.

It is important to note that the balance between day- and night-side reconnection is not in a steady state; this results in a temporally varying convection pattern of plasma and magnetic flux. Consequently an abundance of energy can be stored on the night-side as plasma and magnetic flux builds up in the magnetotail. When the night-side magnetosphere finally undergoes reconnection it can be abrupt and explosive, the magnetotail relaxing to lower energy state, and releasing the energy built up from the convection of plasma and magnetic from the day-side to the night-side. This energy release is referred to as a magnetospheric substorm and will be discussed in more detail in Section 1.5.

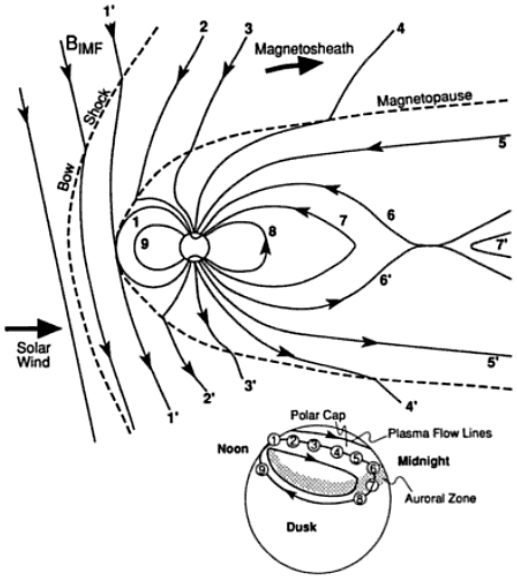

Figure 1.4: Schematic of the Dungey cycle and the resulting convection of plasma and magnetic field from the day-side to the night-side and back. The inset depicts the convection of magnetic footprints the magnetic field and plasma in the ionosphere. Adapted from Kivelson and Russell [1995].

1.4 The Ionosphere

The region between the lower edge of the magnetosphere and the Earth's neutral atmosphere is known as the ionosphere, consisting of a population of ionised particles where the aurora is typically generated. In general the ionosphere lies between ~80-1000 km above the Earth's surface and is formed through the interaction of the Earth's neutral atmosphere with both photons and precipitating energetic particles. The ionisation due to photons is referred to as photoionisation and typically occurs on the day-side where photons from the Sun are able to interact with the Earth's neutral atmosphere; this is the most efficient form of ionisation in the ionosphere. The latter typically occurs from the precipitation of energetic particles emanating from the magnetosphere. This is typically the dominant form ionisation on the night-side, where photons from the Sun are unable to interact with the neutral atmosphere. Note that ionisation from precipitating particles is inherently less efficient then photoionisation, thus, an asymmetry exists between the day- and night-side of the ionosphere such that the number of ionised particles is greater on the day-side than the night-side.

One of the central characteristics of the ionosphere is the ability to conduct electric currents perpendicular to the magnetic field and the presence of large scale ionospheric current systems referred to as electrojets. Most notably are the auroral zone electrojets referred to as the eastward electrojet and the westward electrojet, named after the direction in which the electrojet currents propagate in the ionosphere. The existence of the eastward and westward electrojets is a result of the Dungey cycle, Figure 1.4, and the convection of the Earth's magnetic field in the ionosphere. The motion of magnetic field lines over the poles onto the night-side and around the dawn and dusk flanks and back to the day-side generates a series of electric fields in the ionosphere. In the presence of crossed electric and magnetic fields the ions and electrons in the ionosphere undergo "E-cross-B" drift motion (see Chapter 2 for more details).This drift motion creates a two cell convection pattern of plasma in the ionosphere which mirrors the convection pattern of the magnetic field in the Dungey cycle. In a collisionless plasma both ions and electrons undergo the same "E-cross-B" drift; however, in reality, the ions typically drift more slowly due to collisions with other ions and neutral elements in the ionosphere. The differential drift between ions and electrons in the ionosphere thus creates a net current in the direction opposite the direction in which the ions and electrons "E-cross-B" drift, these currents are the eastward and westward electrojets.

Figure 1.5 is an idealised schematic showing the development of the eastward and westward electrojets in the northern hemisphere as a result of the convection of the magnetic field in the Dungey cycle during a predominantly southward IMF. The black lines depict the motion of the magnetic field over the pole and along the dawn and dusk flanks; note the magnetic field is directed into the page. The dotted circle represents the boundary between open and closed magnetic field, inside of which lies the polar cap. The grey arrows show the direction of the electric field, a result of the motion of the magnetic field, and the thick black arrows show the subsequent "E-cross-B" drift of ions and electrons. The red and blue arrows depict the eastward and westward electrojets, respectively, the current system generated as a result of the differential motion of the ions and electrons in the ionosphere. Note that both east and west electrojets are Hall currents since the current is perpendicular to both the electric and magnetic fields.

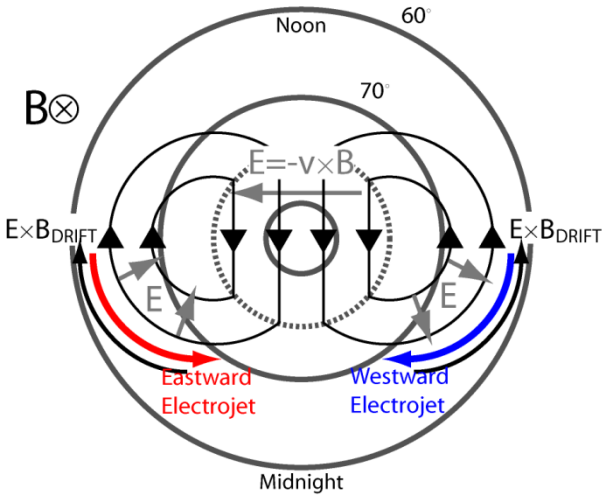

Figure 1.5: A schematic illustrating the generation of the eastward and westward electrojets in the ionosphere. See text for details.

1.5 Magnetospheric Substorms

1.5.1 Phenomenological Model of Substorms

Magnetospheric substorms (also referred to as magnetic substorms or simply substorms) are one of the many terrestrial and near-Earth phenomena driven by the solar wind and the coupling of solar energy into the Earth's magnetosphere. The magnetic substorm was originally characterised by a phenomenological model known as the auroral substorm based on observations of the aurora [*Akasofu*, 1964]. The auroral substorm paradigm describes a sequence of events characterising the dynamics and expansion of the aurora and the auroral oval as observed by ground-based all-sky imagers (ASIs). The auroral substorm is divided into three phases; the growth phase, the expansion phase and the recovery phase, though the original classification of the auroral substorm only considered the expansion and recover phases. Figure 1.6 is a schematic depicting the main features and phases of the auroral substorm.

The growth phase is characterised by the equatorward motion of the aurora and the auroral oval to lower latitudes. The expansion phase of the auroral substorm is characterised by the brightening of the most equatorward auroral arc [*Akasofu*, 1964] or by the formation of a new arc [*Akasofu*, 1977] in approximately the midnight sector. Subsequently the auroral arcs propagate poleward and then explosively expand toward both the evening (westward) and morning (eastward) sectors, becoming increasingly

vibrant and dynamic as they expand. The expansion phase lasts on the order of tens of minutes; the beginning of the expansion phase is referred to as the onset of the auroral substorm. The recovery phase of the auroral substorm is marked by the gradual dimming of aurora and the migration of the aurora back toward the equator and lower latitudes. This typically lasts on the order of hours. The expansion phase is characterised by panels (b)-(d) and the recovery phase by panels (e) and (f) of Figure 1.6. Panel (a) depicts the quiet time aurora prior to the onset of the expansion phase. The arrows in Figure 1.6 illustrate the motion of the aurora during each phase of the auroral substorm.

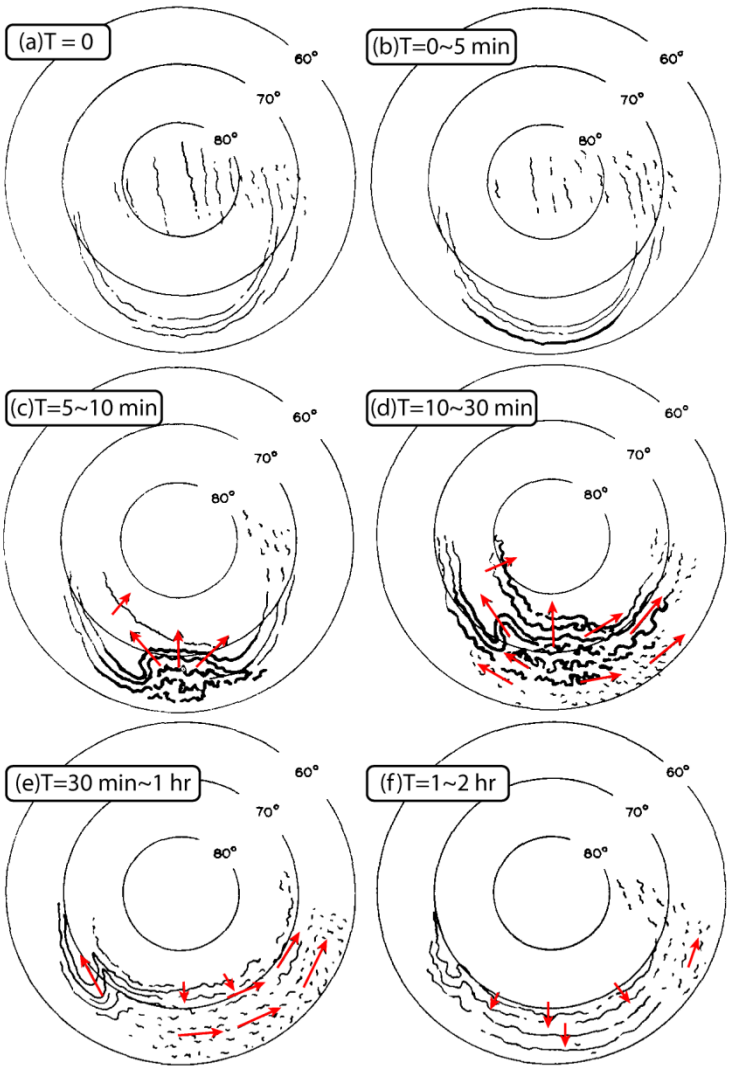

Figure 1.6: A schematic illustrating the phases of the auroral substorm. The sun is toward the top of the diagram, and the night-side toward the bottom. (a) Is the quiet time aurora. (b)-(d) the expansion phase and (e)-(f) the recovery phase. Adapted from Akasofu [1964]

Following Akasofu's [1964] development of the auroral substorm paradigm it was shown that the expansion of the aurora coincided with the enhancement of the ionospheric electrojets [*Akasofu et al.*, 1965], which was observed by ground-based magnetometers as large-scale deflections of the Earth's magnetic field. McPherron [1970] noted that many disturbances of the Earth's magnetic field, including impulsive ULF waves, weak deflections of the Earth's magnetic field, and the expansion of the polar cap and the auroral oval, occurred before the onset of the auroral substorm expansion phase. McPherron referred to this as the substorm growth phase [*McPherron*, 1970], which lead to the concept of the magnetospheric substorm, a phenomenological model describing a substorm as a sequence of events in the Earth's magnetosphere which were manifested in, and coupled to, the ionosphere.

As previously mentioned in Section 1.3, the solar wind is able to couple to the magnetosphere via magnetic reconnection on the day-side, transferring energy, momentum and mass from the solar wind to the Earth's magnetosphere. Reconnection on the day-side produces open field lines which are dragged onto the night-side by the solar wind. These open field lines stretch away from the Earth and are slowly compressed together forming the magnetotail. As day-side reconnection continues, energy is extracted from the solar wind and stored in the night-side magnetosphere. As additional magnetic flux and plasma convects onto the night-side, the size of both the polar cap and auroral oval gradually increase. The magnetotail becomes increasingly stretched and compressed, forming a current sheet in approximately the equatorial plane of the magnetotail between regions of anti-parallel stretched magnetic fields. This current sheet carries the cross-tail current which flows in the equatorial plane of the magnetotail from the dawn side toward the dusk side. The build up of energy in the night-side magnetosphere, and the formation of the stretched magnetotail, constitutes the growth phase of the magnetospheric substorm.

The substorm expansion phase is characterised by the explosive release of energy stored in the magnetotail during the growth phase. During the substorm expansion phase the magnetotail dipolarizes (magnetic topology becomes more dipolar) and the cross-tail current is diverted along magnetic field lines into the ionosphere enhancing the pre-existing westward electrojet, see Section 1.4. The current system that is

established by the diverted cross-tail current is known as the Substorm Current Wedge (SCW) and is composed of a downward field-aligned current (FAC) in the post-midnight sector, a westward electrojet in the ionosphere and an upward FAC in the pre-midnight sector. On the ground the formation of the SCW is observed by magnetometers as large-scale positive and negative deflections of the Earth's magnetic field referred to as substorm bays that are usually associated with the onset of ULF waves and with a westward expansion of the aurora in the upper atmosphere referred to as the Westward Traveling Surge (WTS). A schematic of the SCW and the North/South and East/West deflection of the magnetic fields observed by magnetometers is shown in Figure 1.7. Note that ground-based magnetometers cannot differentiate between line and distributed current systems, thus the SCW current system described above is an equivalent current system since it generates magnetic disturbances which are equivalent to those observed on the ground [e.g., *Kivelson and Russell*, 1995].

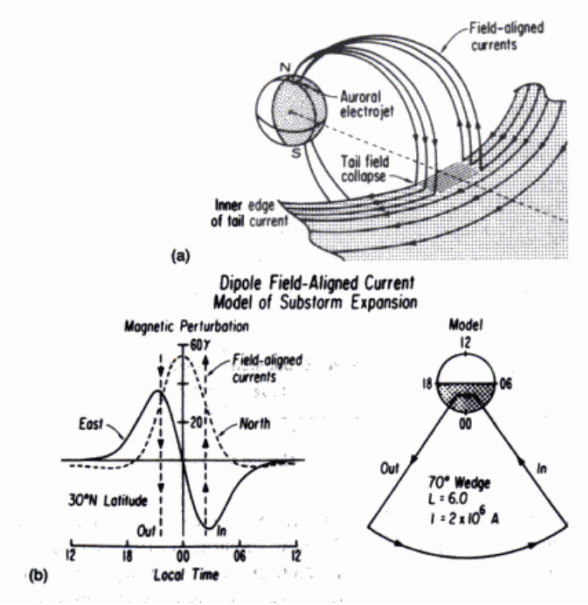

Figure 1.7: Schematic of the SCW. (a)The three dimensional structure of a simple current wedge in the magnetotail. (b)The local-time and latitudinal structure of magnetic perturbations (left) in the presence of a modeled SCW (right). Figure adapted from Clauer and McPherron [1974].

The explosive release of stored energy in the magnetotail is believed to follow reconnection in the tail, and is seen in the ionosphere as the brightening of the aurora. Reconnection in the magnetotail closes open field lines in turn causing the polar cap to

shrink and the aurora to expand toward the poles. This is observed on the ground and in the ionosphere as the poleward motion of the aurora, c.f. Figure 1.6 (c).

The development of the WTS and formation of the SCW is followed by longitudinal expansion of the aurora shown in Figure 1.6 (d). Subsequently, as the SCW begins to dissipate, auroral dynamics begin to subside and the polar cap and auroral oval move back toward lower latitudes as the night-side magnetosphere becomes increasingly more tail-like. This is the recovery phase of the magnetospheric substorm, c.f. Figure 1.6 (e) and (f). This completes the substorm sequence. Note that the substorm sequence may not always fully evolve as described above and in some cases the expansion phase may be quenched or interrupted. Such events are known as pseudo-breakups, and are often characterised by the limited development of a SCW and/or localised auroral activity [e.g., *Baker et al.*, 1996 and references therein].

1.5.2 The Substorm Expansion Phase

The onset of a magnetic substorm, at the beginning of the expansion phase, has been studied in depth for over forty years [*Akasofu*, 1964]. However, the physical mechanism triggering the onset of the substorm expansion phase continues to elude scientists and remains a topic of considerable debate and controversy in space physics. In the ionosphere, the substorm expansion phase is manifested as the brightening of the aurora and auroral breakup, and in the magnetotail, by the onset of reconnection and the disruption of the cross-tail current. The inability to adequately determine the relative start time of these signatures in the ionosphere and in the magnetosphere has continued to be a major pitfall in unambiguously determining the physical mechanism responsible for triggering the onset of the substorm expansion phase. Several phenomenological substorm models exist which suggest the physical mechanism responsible for triggering the onset of the substorm expansion phase and characterise the sequence of events observed during the expansion phase. However, in the last two decades two of these models have become particularly favoured by the substorm community: the Near Earth Neutral Line (NENL) model and the Current Disruption (CD) model.

In the NENL model, reconnection in the magnetotail at a distance of ~25 R_E (referred to as the Near-Earth Neutral Line) triggers the onset of the substorm expansion phase

[*Baker et al.*, 1996]. As reconnection in the magnetotail commences, open magnetic field lines are closed, the energy stored in the magnetotail is released and the night-side magnetotail dipolarizes. The energy released is believed to accelerate bursty bulk plasma flows (BBFs) toward the Earth [*Angelopoulos et al.*, 1992]. As these flows propagate inward they encounter a stronger and more dipolar magnetic field and decelerate [*Shiokawa et al.*, 1997]. The accumulation of plasma and the dipolarization of the Earth's magnetic field disrupts the cross-tail current, diverting it into the ionosphere and forming the SCW in the magnetotail [*Shiokawa et al.*, 1998]. Following reconnection and current disruption in the magnetotail, auroral breakup is then observed in the ionosphere. The sequence of events hypothesised by the NENL model is referred to as "outside-to-in" as the expansion phase onset is triggered in the mid-distant magnetotail, and is subsequently followed by current disruption and then auroral break up closer to the Earth. Figure 1.8 is a schematic illustrating auroral breakup, current disruption and reconnection during the expansion phase onset. The inset panel, (ii), depicts the sequence of events proposed in the NENL substorm paradigm.

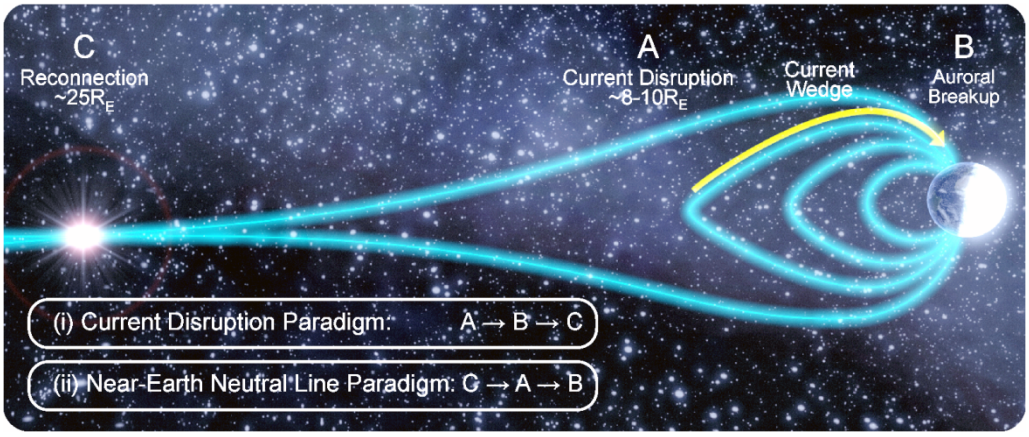

Figure 1.8: Schematic of the two substorm paradigms and the phenomena observed at the onset of the substorm expansion phase. The insets depict the sequence of events observed in the CD paradigm, (i), and the NENL paradigm, (ii). Figure adapted from Rae et al. [2009a].

In the CD model, the expansion phase onset is triggered by a localised plasma instability which disrupts the cross-tail current [*Lui*, 1996]. The plasma instability has been hypothesised to be a ballooning mode [e.g., *Roux et al.*, 1991], lower hybrid turbulence [e.g., *Huba et al.*, 1977], or a cross-field current instability in the central plasma sheet

[e.g., *Lui et al.*, 1995]. The formation of the SCW and auroral breakup is formed as a consequence of this current disruption. Following the initial disruption of the cross-tail current, a rarefaction wave is launched which propagates down the tail and subsequently triggers reconnection at the NENL [*Angelopoulos*, 2008]. The CD model is referred to as "inside-to-out" as the expansion phase onset is triggered in the inner magnetotail. The top inset, (i), of Figure 1.8 depicts the sequence of events observed in CD substorm model.

1.5.3 Ultra Low Frequency (ULF) Waves and Magnetospheric Substorms

Typically ULF waves are observed in the magnetosphere by in-situ magnetometer, plasma and electric field instruments onboard Earth orbiting spacecraft or on the ground by magnetometers which sense periodic ionospheric currents. In general, ULF waves can be driven by the solar wind exciting field line resonances (FLRs) [e.g., *Rae et al.*, 2005], by solar wind impulses impacting the Earth's magnetosphere [*Mathie and Mann*, 2000] or during impulsive energy release inside the magnetosphere such as at the onset of the substorm expansion phase [e.g., *Milling et al.*, 2008]. The former are referred to as continuous ULF waves, and are typically quasi-monochromatic, and can sometimes be observed for several hours of local time. The latter are referred to as impulsive ULF waves [*Jacobs et al.*, 1964]. Impulsive ULF waves are typically observed during magnetic substorms; typically these waves are observed as wavepackets or wavetrains, exhibit multiple phase skips and have a finite duration on the order of tens of minutes [e.g., *Bösinger et al.*, 1981; *Olson*, 1999]. The ULF waves studied and referred to throughout the rest of this thesis are impulsive ULF waves observed during magnetic substorms.

Irregular and impulsive ULF waves are known as Pi pulsations [*Jacobs et al.*, 1964] and are generally sub-classified into three groups. These groups are: Pi2 pulsations with periods of 40-150 s, Pi1 pulsations with periods of 1-40 s [*Jacobs et al.*, 1964] and PiB pulsations (also referred to as Pi1B pulsations) with periods less than ~10s [e.g., *Bösinger et al.*, 1981]. Some Pi2 pulsations have large amplitudes and occur in wavepackets associated with the initial disturbance forming the SCW [*Olson*, 1999]; these are discussed in detail in Chapter 6. Pi1 pulsations are typically smaller amplitude waves believed to be intimately connected with the onset of the substorm expansion

phase; however shorter period Pi2 waves have also been shown to exhibit similar characteristics as the Pi1 waves observed during the expansion phase onset [*Rae et al.*, 2009b]. These shorter period waves, the long period Pi1 waves and short period Pi2 waves, are discussed in detail in Chapter 5. Pi1B pulsations are usually broadband and bursty fluctuations of the Earth's magnetic field. These pulsations have been linked to auroral breakup and have been used as excellent indicators of substorm onset [*Posch et al.*, 2007]. However Pi1B waves are not discussed in detail in the remainder of this thesis. It is worth noting that in the original classification scheme of impulsive ULF waves there was no physical reason for separating the classification of Pi1 and Pi2 waves at 40 s [*Jacobs et al.*, 1964]. A superposed epoch analysis of the ULF power spectra observed during substorm expansion phase onset reveals statistically that there is no difference in the characteristics of Pi waves on either side of the 40 s boundary between Pi1 and Pi2 waves. This is the topic of Chapter 7.

Chapter 2 Plasma Theory and Magnetohydrodynamics

2.1 Introduction

In this thesis a plasma will be considered to be a quasi-neutral hot gas consisting of approximately equal numbers of ions and electrons. Typically plasmas such as those in solar wind and in the Earth's magnetosphere are assumed to be rarefied gases such that the plasma is assumed to be collisionless and are characterised by a characteristic length scale known as the Debye length,

$$\lambda_D^2 = \frac{\varepsilon_0 k_B T_e}{n_e e^2}, \tag{2.1}$$

where T_e is the temperature of the plasma, n_e is the number density of electrons in the plasma, k_B is the Boltzmann constant, ε_0 is the permittivity of free space and e is the charge of an electron. The Debye length defines the scale governing the shielding of electric fields for the charged species in the plasma. At length scales larger than λ_D, charge shielding occurs such that the electric field from a given charged particle is cancelled by the collective effects of neighbouring particles. At scales larger then λ_D, and in plasmas where the number of particles in the Debye sphere (a sphere of radius λ_D) is large such that there exists a large enough population of electrons and ions for shielding to occur, the plasma interacts as a collective body of particles experiencing long-range forces which can lead to universal drifts, oscillations and instabilities within the plasma.

This Chapter introduces the basic plasma theory required for understanding the physics of magnetospheric substorms and ULF waves. In particular, two types of plasma motion, single particle motion and magnetohydrodynamics or fluid motion of plasmas, are developed. These can be considered to be two extreme paradigms which describe the collective behaviour of a plasma. Additionally, the applicable plasma dynamics are considered in regard to ULF waves and substorms.

2.2 Single Particle Motion

Single particle motion describes the trajectory of a single plasma particle as a result of various forces such as gravity and electromagnetic forces. Despite the fact that only a single particle is considered, single particle motion provides remarkable insight into the collective behaviour of plasma species (e.g., ions or electrons) and the entire plasma

itself. Typically, self-consistent solutions to a general force equation describing the motion of a particle are difficult to obtain. Thus, this section considers only the relevant motions of a plasma particle in a specified magnetic and electric fields.

In the presence of a magnetic field ($\boldsymbol{B}$) and electric field ($\boldsymbol{E}$), the trajectory of a particle of mass m, charge q and velocity $\boldsymbol{v}$, is governed by the Lorentz force

$$\boldsymbol{F} = q\boldsymbol{E} + q\boldsymbol{v} \times \boldsymbol{B}. \tag{2.2}$$

Two cases of single particle motion will be developed for charged particles influenced by the Lorentz force. First, a charged particle in the presence of a uniform time-independent magnetic field, and second, the motion of a charged particle in a static and uniform electric and magnetic field, will be considered.

In the first case ($\boldsymbol{E}$=0) equation (2.2) simplifies to

$$m\frac{d\boldsymbol{v}}{dt} = q\boldsymbol{v} \times \boldsymbol{B}. \tag{2.3}$$

Aligning the magnetic field in Cartesian coordinates with the *z* direction and expanding gives

$$m\frac{dv_x}{dt} = qv_yB, \tag{2.4}$$

$$m\frac{dv_y}{dt} = qv_xB, \tag{2.5}$$

$$m\frac{dv_z}{dt} = 0. \tag{2.6}$$

Differentiating equations (2.4) and (2.5) and substituting gives

$$\frac{d^2v_i}{dt^2} = \left(\frac{qB}{m}\right)^2 v_i, for\ i = x, y. \tag{2.7}$$

This is equivalent to an equation for simple harmonic motion in both the *x* and *y* directions. Note that because the coordinate system can always be rotated such that $\boldsymbol{v}$ is parallel to the x direction equation (2.7) simplifies to the special case of circular motion in the *x*-*y* plane with an angular frequency (the cyclotron or Larmor frequency) and radius (the cyclotron or Larmor radius) defined by

$$\omega_c = \frac{qB}{m}, \tag{2.8}$$

$$r_c = \frac{v_\perp}{\omega_c} = \frac{mv_\perp}{qB}, \tag{2.9}$$

where $v_\perp$ is the magnitude of the velocity perpendicular to $\boldsymbol{B}$ in the x-y plane. Note that the direction of rotation is defined by the sign of q and thus electrons and ions in a plasma rotate about the magnetic field in opposite directions. This is referred to as gyromotion. The solution to equation (2.6) is constant v_z, equal to the initial z-component of the velocity of the charged particle.

In the second case, for uniform and static magnetic and electric fields, a charged particle still undergoes the gyromotion associated with a uniform magnetic field. However, this motion is superimposed on a drift path such that the center of the gyration drifts perpendicular to both the magnetic and electric fields. Consider a particle with velocity $\boldsymbol{v}$ which is composed of two components, one parallel to the background magnetic field, $v_\parallel$ and one perpendicular to background magnetic field, $\boldsymbol{v}_\perp$. Substituting $\boldsymbol{v}$ into equation (2.2) and decomposing into $\boldsymbol{v}_\perp$ and $v_\parallel$ we obtain

$$m\frac{dv_\parallel}{dt} = qE_\parallel, \tag{2.10}$$

$$m\frac{d\boldsymbol{v}_\perp}{dt} = q\boldsymbol{E}_\perp + q\boldsymbol{v}_\perp \times \boldsymbol{B}. \tag{2.11}$$

The parallel component of the velocity, equation (2.10), is easily solved, the solution of which is an accelerating particle with the acceleration equal to $q\boldsymbol{E}_\parallel$. The perpendicular component of the velocity, as previously mentioned, is composed of the gyromotion of the particle, $\boldsymbol{v_G}$, superposed on a constant perpendicular drift velocity, $\boldsymbol{v_D}$. Assuming that $|\boldsymbol{v_G}| \gg |\boldsymbol{v_D}|$, then equation (2.11) can be broken into two equations, one describing the gyromotion (2.12) and the other the drift motion (2.13):

$$m\frac{d\boldsymbol{v_G}}{dt} = q\boldsymbol{v_G} \times \boldsymbol{B}, \tag{2.12}$$

$$0 = q\boldsymbol{E}_\perp + q\boldsymbol{v_D} \times \boldsymbol{B}. \tag{2.13}$$

Crossing both sides with $\boldsymbol{B}$ and solving for $\boldsymbol{v_D}$gives

$$\boldsymbol{v_D} = \frac{\boldsymbol{E}_\perp \times \boldsymbol{B}}{B^2}. \tag{2.14}$$

This drift velocity is referred to as the "E cross B" drift and is independent of the mass and charge of a particle. Thus all charged particles in a plasma in the absence of collisions undergo the same E cross B in the same direction. The E cross B drift is responsible for the formation of both the eastward and westward ionospheric electrojets (see Section 1.4).

In general, a charged particle subjected to any perpendicular force experiences a perpendicular drift velocity superimposed onto the particle's gyromotion. This generalised drift velocity of a charged particle in the presence of a force $\boldsymbol{F}$ is given by

$$\boldsymbol{v_D} = \frac{1}{q}\frac{\boldsymbol{F} \times \boldsymbol{B}}{B^2}. \tag{2.15}$$

This generalised drift also results in drift velocities due to gradients in either magnetic field or thermal pressure, due to the curvature of the magnetic field, and due to the force of gravity [see e.g. Table 2.7, *Chen*, 1984]. Note that if $\boldsymbol{F}$ is independent of q then the ions and electrons within a plasma drift in opposite directions.

2.3 Plasma Theory and Governing Equations

Single particle motion can describe many of the features of the collective properties of plasma motion. However, on macroscopic scales plasmas are more readily described as a conducting fluid. This is known as magnetohydrodynamic theory or MHD and enables a self-consistent approach to plasma motion and dynamics. Note that like fluid mechanics, MHD is only valid on spatial and temporal scales where the motion of individual particles on kinetic scales can be neglected. These scales are typically the largest kinetic scale of the plasma and in space plasmas are roughly defined by the Debye length and Larmor radius and the gyro-period of the ions within the plasma. Further, in MHD, as stated earlier, the plasma is assumed to be quasi-neutral. The following subsections introduce the equations governing MHD and further develop some basic properties of an MHD plasma. In Section 2.4, these equations are used to

develop the wave modes observed in an MHD plasma and which are discussed in the context of ULF waves and substorms throughout the remainder of this thesis.

2.3.1 Continuity Equation

The continuity equation describes the conservation of mass, and is given by

$$\frac{\partial \rho}{\partial t} + \nabla \cdot (\rho \boldsymbol{v}) = 0, \tag{2.16}$$

where ρ is the density of the fluid element and $\boldsymbol{v}$ is the fluid elements flow velocity. The first term on the left hand side of (2.16) describes the temporal rate of change of mass for a given fluid element, this is balanced by the second term, the mass flux into this fluid element.

2.3.2 Equation of Motion

The equation of motion is Newton's second law applied to a fluid element of a plasma and describes the change in momentum per unit time. The equation of motion for a collisionless plasma, and ignoring gravity, is given by

$$\rho \frac{d\boldsymbol{v}}{dt} = \boldsymbol{j} \times \boldsymbol{B} - \nabla P, \tag{2.17}$$

where $\boldsymbol{j}$ is the current density, $\boldsymbol{B}$ is the magnetic field, P is the pressure, and d/dt is the total, or convective derivative of a vector $\boldsymbol{U}$, defined as

$$\frac{d\boldsymbol{U}}{dt} = \frac{\partial \boldsymbol{U}}{\partial t} + (\boldsymbol{U} \cdot \nabla)\boldsymbol{U}. \tag{2.18}$$

2.3.3 Equation of State

A plasma can also be described by an equation of state relating pressure to the temperature and density of the fluid. Typically, the equation of state of a plasma is assumed to be of the form

$$\frac{d}{dt}(P\rho^{-\gamma}) = 0, \tag{2.19}$$

where γ is a constant dependent on the type of plasma. For an adiabatic process, γ is taken to be 5/3.

2.3.4 Ohm's Law

Because we have made the assumption that a plasma is a conducting medium we must consider the effects of the electric and magnetic field on the current density. This can be specified by a generalised form of Ohm's Law

$$\boldsymbol{j} = \sigma(\boldsymbol{E} + \boldsymbol{v} \times \boldsymbol{B}), \tag{2.20}$$

where σ is the conductivity of the plasma.

2.3.5 Maxwell's Equations

Maxwell's equations relate the electric field, magnetic field and current density of a system in four equations and provide closure to the system of equations governing the motion of a plasma. In a quasi-neutral plasma Maxwell's equations can be written as:

$$\nabla \cdot \boldsymbol{E} = 0 \qquad \text{Gauss' Law} \tag{2.21}$$

$$\nabla \times \boldsymbol{E} = -\frac{\partial \boldsymbol{B}}{\partial t} \qquad \text{Faraday's Law} \tag{2.22}$$

$$\nabla \cdot \boldsymbol{B} = 0 \tag{2.23}$$

$$\nabla \times \boldsymbol{B} = \mu_0 \boldsymbol{j} + \varepsilon_0 \mu_0 \frac{\partial \boldsymbol{E}}{\partial t} \qquad \text{Ampere's Law} \tag{2.24}$$

Note that for low frequency waves and non-relativistic plasmas the second term on the right hand side of Amperes law, referred to as the displacement current, can be neglected. If L and τ are characteristic length and time scales of any perturbation of the plasma, than the ratio of the displacement current to the curl of the magnetic field can be written as [*Kivelson and Russell*, 1995],

$$\frac{\left|\varepsilon_0 \mu_0 \frac{\partial \boldsymbol{E}}{\partial t}\right|}{|\nabla \times \boldsymbol{B}|} \cong \frac{\varepsilon_0 \mu_0 \frac{|\boldsymbol{E}|}{\tau}}{\frac{|\boldsymbol{B}|}{\boldsymbol{L}}} = \frac{\varepsilon_0 \mu_0 \frac{\boldsymbol{L}|\boldsymbol{B}|}{\tau^2}}{\frac{|\boldsymbol{B}|}{\boldsymbol{L}}} = \frac{L^2}{c^2 \tau^2} = \frac{u^2}{c^2}, \tag{2.25}$$

where u is a characteristic velocity of the plasma and c is the speed of light. For the plasmas considered here, $u/\,c \ll 1$, and thus the displacement current in equation (2.24) can be ignored.

2.3.6 Induction Equation

Utilising the above equations, an expression can be obtained which describes the rate of change of the magnetic field of a plasma with respect to time. By combining equations (2.20) and (2.24), eliminating the current density and substituting equation (2.22) for the electric field gives

$$\nabla \times \nabla \times \boldsymbol{B} = \mu_0 \sigma \left(-\frac{\partial \boldsymbol{B}}{\partial t} + \nabla \times \boldsymbol{v} \times \boldsymbol{B} \right), \tag{2.26}$$

which can be simplified using the vector identity

$$\nabla \times \nabla \times \boldsymbol{A} = \nabla(\nabla \cdot \mathbf{A}) - \nabla^2 \boldsymbol{A}, \tag{2.27}$$

and equation (2.23) to obtain

$$\frac{\partial \boldsymbol{B}}{\partial t} = \nabla \times \boldsymbol{v} \times \boldsymbol{B} + \frac{1}{\mu_0 \sigma} \nabla^2 \boldsymbol{B}. \tag{2.28}$$

This is referred to as the induction equation. The first term on the right hand side of the induction equation is referred to as the advective term, and the second as the diffusive term. The dominant term in the induction equation characterises the prevailing motion and evolution of the magnetic field and plasma in a given system. The magnetic Reynolds number, the ratio of the advective term to the diffusive term, is a dimensionless number which quantifies which term on the right hand side of the induction equation is dominant. The magnetic Reynolds number is given by

$$R_M = \frac{\nabla \times \boldsymbol{v} \times \boldsymbol{B}}{\frac{1}{\mu_0 \sigma} \nabla^2 \boldsymbol{B}}. \tag{2.29}$$

This can be simplified by approximating ∇ to be ~$1/L$, where L defines the spatial length scale in which the plasma and magnetic field change, giving

$$R_M = \mu_0 \sigma v L. \tag{2.30}$$

If the Reynolds number is sufficiently large, $|R_M| \gg 1$, then the advective term of the induction equation dominates and equation (2.28) simplifies to

$$\frac{\partial \boldsymbol{B}}{\partial t} = \nabla \times \boldsymbol{v} \times \boldsymbol{B}. \tag{2.31}$$

This is referred to as the advective limit and occurs in media where the conductivity or the velocity of the plasma is high, or when the magnetic field has little to no spatial gradient (L is large). Note that in the advective limit the magnetic field and the plasma velocity are coupled, such that the magnetic flux through any closed contour moving with the plasma is constant. Simply stated, the plasma is tied to the magnetic field and vice-versa, both traveling with the same velocity. This is referred to as the frozen in flux theorem, introduced in Section 1.2, and is responsible for coupling the solar wind plasma to the IMF.

When $|R_M| \ll 1$, the diffusion term dominates and equation (2.28) becomes

$$\frac{\partial \boldsymbol{B}}{\partial t} = \frac{1}{\mu_0 \sigma} \nabla^2 \boldsymbol{B}. \tag{2.32}$$

This is the diffusion limit of the induction equation. In this limit the plasma and magnetic field are decoupled and the magnetic field is able to diffuse through the plasma, analogous to heat diffusing in a metal rod. The diffusion term is typically dominant at the boundary between two plasma regimes where the magnetic field can vary quickly over short distances such that both L and R_M are small. The diffusive limit of the induction equation is important when considering magnetic reconnection, and is discussed in the following subsection.

2.3.7 Magnetic Reconnection

Magnetic reconnection is the process by which two distinct plasma or magnetic field regimes are able to interact, enabling the energy stored in the magnetic field to be converted to thermal and kinetic energy. For simplicity, this section will consider a two dimensional model of magnetic reconnection and will use the concepts derived to qualitatively describe a model which can be used to understand the Dungey cycle and the energy release observed during magnetic substorms.

Consider the magnetic field topology shown in Figure 2.1. Above the x-axis the magnetic field points in the negative *x* direction, and points in the positive *x* direction below the x-axis. In the region separating the anti-parallel magnetic fields, the divergence of the

magnetic field is non-zero and an infinitely thin current sheet forms along the x-axis. In this region, the magnetic field rapidly changes over a small distance so the magnetic Reynolds number (R_M) is small and both the advective and diffusive terms are required in the induction equation. However, if the plasma is stationary ($\boldsymbol{v}$=0) then we are able to consider only the diffusive term in the induction equation and the induction equation becomes (c.f. equation 1.29)

$$\frac{\partial B_x}{\partial t} = \frac{1}{\mu_0 \sigma} \frac{\partial B_x^2}{\partial z^2}, \tag{2.33}$$

a solution of which is

$$B_x(z) = B_0 erf\left[\left(\frac{\mu_0 \sigma}{2\mathrm{t}}\right)^{1/2} z\right], \tag{2.34}$$

where *erf* is the error function, B_0 is the magnetic field strength at t = 0 and z is the distance away from the x-axis. In the above solution the magnetic field above and below the x-axis diffuses toward x=0 where it is annihilated as the anti-parallel fields encounter each other. As the magnetic field annihilates, energy stored in the magnetic field is converted to thermal and kinetic energy, heating the local plasma.

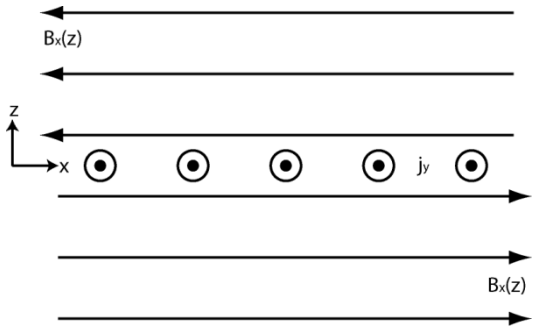

Figure 2.1: Schematic of the magnetic field $B_x(z)$ and j_y and current sheet used to describe a simple model of magnetic reconnection.

Note that the above description of reconnection is self limiting; as the magnetic field continues to annihilate the gradient decreases resulting in a slower diffusion rate and in turn slowing the entire process. In order to achieve steady state reconnection magnetic field must be continually introduced into the system. This can be achieved if an electric field parallel to the current sheet exists. The resulting E cross B drift continually

introduces new plasma as well as magnetic field (frozen in flux) into the system transporting it from z=$\pm\infty$ to the the x-axis (z=0) where the magnetic field is annihilated. Though this adequately describes a steady state of magnetic reconnection, the scenario is physically inconsistent. Both plasma and magnetic field are continually introduced into the system and the added field is annihilated along the current sheet. However nothing happens to the inflowing plasma which should pile up at z=0. For steady state reconnection we require an inflowing plasma, however to be physically consistent we also require an outflowing plasma which carries away the plasma brought in from z=$\pm\infty$.

A physically consistent system of steady state magnetic reconnection can be developed by considering reconnection at a single point rather than along the plane define by the current sheet. This is referred to as the X-line (or neutral line) model of reconnection and is shown schematically in Figure 2.2. Both plasma and magnetic field flow inward toward the origin (U_{in}) where the magnetic field breaks and reconnects with the field flowing in from the opposite direction. This is similar to the magnetic reconnection described above, however, in the region (length L) where the magnetic field undergoes reconnection the diffusive term in the advection equation dominates, the inflowing plasma is no longer frozen to the field, and is thus able to diffuse across the boundary and flow outward from the point of reconnection (U_{out}) along a path defined by the E cross B drift. Figure 2.2 shows the direction of the inflowing (U_{in}) and outflowing plasma (U_{out}) and magnetic field (white arrows) as well the current sheet and the diffusion region (highlighted in grey). Note that the magnetic field direction (black arrows) is opposite to the field shown in Figure 2.1, and in this model both the electric field and direction of the current are directed into the page.

The X-line model of reconnection is sufficient for qualitatively understanding reconnection in the magnetosphere and moreover reconnection during magnetic substorms. It is important to note however that reconnection in the magnetosphere is far more complicated. In the magnetosphere reconnection is variable, being strongly dependent on the topology of the magnetic field, and is often bursty or episodic leading to a non-steady convection of plasma and magnetic field in both the day- and night-side magnetosphere. On the day-side the Earth's magnetic field is predominantly northward,

and hence in order for reconnection to occur the IMF must have a southward magnetic field component. Day-side reconnection is therefore largely dependent on the solar wind and the topology and direction of the IMF. On the night-side, reconnection is sporadic and is believed to be triggered, possibly by a instability in the night-side magnetosphere [*Lui*, 1996]. Non-steady reconnection on both the day- and night-side inherently leads to the potential build up of magnetic field, plasma, and energy stored in the night-side magnetosphere as the tail becomes increasingly stretched and elongated. When reconnection is finally triggered in the night-side magnetosphere the energy stored in the magnetotail is released, plasma is accelerated toward the earth, the magnetotail dipolarizes, and the aurora expands in the ionosphere. Non-steady reconnection in both the day- and night-side magnetosphere results in the different phases of a magnetic substorm, described in detail in Section 1.5.

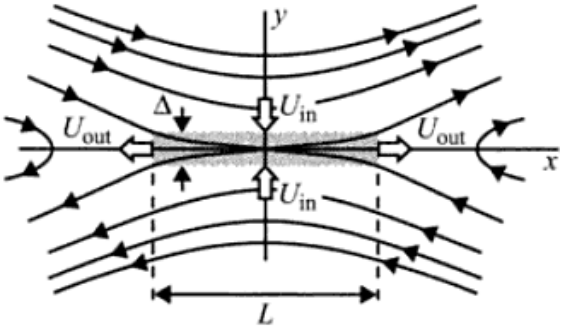

Figure 2.2: Schematic of X-line reconnection. See text for details. Adapted from Gurnett and Bhattacharjee [2005]

2.4 MHD Wave Modes

Using the MHD equations outlined in the previous section it is possible to investigate the properties of various waves supported in a plasma described by MHD. ULF waves, introduced in the previous Chapter, are a class of MHD waves with periods roughly between 0.2-600 s. This section will provide the context and theory required to understand the ULF waves considered in the latter portions of this thesis. For simplicity we will consider linear (first order) plane wave solutions of the form

$$\begin{aligned} \boldsymbol{B} &= \boldsymbol{B}_0 + \boldsymbol{B}_1, \\ \boldsymbol{E} &= \boldsymbol{E}_0 + \boldsymbol{E}_1, \end{aligned} \tag{2.35}$$

$$\boldsymbol{v} = \boldsymbol{v}_0 + \boldsymbol{v}_1,$$
$$\rho = \rho_0 + \rho_1,$$
$$P = P_0 + P_1,$$

where the subscript *0* represents a uniform, time independent background quantity and the subscript *1* represents a small amplitude perturbation superimposed on the background. Further, it is assumed that there is no internal background electric field and that the background plasma is stationary such that $\boldsymbol{E_0} = \boldsymbol{v_0} \equiv 0$.

Substituting the above into the continuity equation (2.16), the equation of motion (2.17), the equation of state (2.19), Faradays law (2.22), simplifying and ignoring second order and higher terms we obtain

$$\frac{\partial \rho_1}{\partial t} + \nabla \cdot (\rho_0 \boldsymbol{v}_1) = 0, \tag{2.36}$$

$$\rho_0 \frac{\partial \boldsymbol{v}_1}{\partial t} = -\nabla P + \frac{1}{\mu_0}(\nabla \times \boldsymbol{B}_0 \times \boldsymbol{B}_1), \tag{2.37}$$

$$\frac{\partial \boldsymbol{B}_1}{\partial t} = \nabla \times \boldsymbol{v}_1 \times \boldsymbol{B}_0, \tag{2.38}$$

$$P_1 = c_s^2 \, \rho_1, \tag{2.39}$$

$$c_s^2 = \gamma \frac{P_0}{\rho_0}, \tag{2.40}$$

where c_s defines the speed of sound in the plasma.

The above differential equations can be further simplified by assuming a Fourier representation of the plane wave solutions for the perturbed quantities of the form

$$Q_1 = \delta Q exp[i(\boldsymbol{k} \cdot \boldsymbol{r} - \omega t)], \tag{2.41}$$

such that

$$\nabla \rightarrow i\boldsymbol{k}, \tag{2.42}$$

$$\frac{\partial}{\partial \mathrm{t}} \rightarrow -i\omega, \tag{2.43}$$

$$\boldsymbol{v}_p = \frac{\omega}{\boldsymbol{k}}, \tag{2.44}$$

$$\boldsymbol{v}_g = \nabla_{\boldsymbol{k}} \omega, \tag{2.45}$$

where $\boldsymbol{k}$ is the wave vector, and ω is the angular frequency. Here $\boldsymbol{v}_p$ is the phase velocity and defines the direction and speed of constant phase fronts and $\boldsymbol{v}_g$ is the group velocity defining the propagation of the wavepacket and the direction in which energy is transported.

Using the above and simplifying equations (2.36) to (2.40), we obtain a single governing equation for the velocity perturbation $\delta\boldsymbol{v}$, (2.46), which can also be written in matrix form, equation (2.47), where the matrix $\boldsymbol{A}$ is a function of $\boldsymbol{B}_0$, ρ_0, c_s, ω,and $\boldsymbol{k}$. Note that both equations (2.46) and (2.47) are no longer dependent on spatial or temporal derivatives and can be readily solved algebraically.

$$\begin{aligned} -\rho_0\omega\delta\boldsymbol{v} &= \frac{-\rho_0 c_s^2}{\omega}(\boldsymbol{k}\cdot\delta\boldsymbol{v})\boldsymbol{k} \\ &+ \frac{1}{\mu_0\omega}[(\boldsymbol{k}\cdot\boldsymbol{B}_0)(\boldsymbol{k}\cdot\delta\boldsymbol{v})\boldsymbol{B}_0 - (\boldsymbol{k}\cdot\boldsymbol{B}_0)^2\delta\boldsymbol{v} \\ &- (\boldsymbol{k}\cdot\delta\boldsymbol{v})B_0^2\boldsymbol{k} + (\boldsymbol{k}\cdot\boldsymbol{B}_0)(\boldsymbol{B}_0\cdot\delta\boldsymbol{v})\boldsymbol{k}] \end{aligned} \tag{2.46}$$

$$\boldsymbol{A}\delta\boldsymbol{v} = 0 \tag{2.47}$$

The above has non-trivial solutions if and only if the determinant of the matrix $\boldsymbol{A}$ is non-zero. This leads to the generalised dispersion relation, relating the angular frequency to the wave vector.

In order to simplify the above we introduce a field-aligned Cartesian coordinate system. Consider a generic magnetic field, $\boldsymbol{B}_0$, and wave vector $\boldsymbol{k}$. In the field-aligned coordinate system the magnetic field is parallel to the z-axis. Further, we can force the projection of the wave vector in the *x*-*y* plane to align with the x-axis (this is simply a rotation of the *x*-*y* plane about the z-axis) giving

$$\boldsymbol{B}_0 = (0,0,B_z), \tag{2.48}$$

$$\boldsymbol{k} = (k_x,0,k_z) \equiv \big(ksin(\theta),0,kcos(\theta)\big), \tag{2.49}$$

where θ is the angle between the *z*-axis and $\boldsymbol{k}$. Substituting the above into equation (2.46), dividing through by k^2 and writing the resulting equation in the form of (2.47) we obtain the matrix equation shown in (2.50) and the generalised dispersion relation defined by equation (2.51),

$$\begin{bmatrix} v_p^2 - c_s^2 sin^2(\theta) - v_a^2 & 0 & -c_s^2 sin^2(\theta)cos^2(\theta) \\ 0 & v_p^2 - v_a^2 cos^2(\theta) & 0 \\ -c_s^2 sin^2(\theta)cos^2(\theta) & 0 & v_p^2 - c_s^2 cos^2(\theta) \end{bmatrix} \begin{bmatrix} \delta v_x \\ \delta v_y \\ \delta v_z \end{bmatrix} = 0, \quad (2.50)$$

$$\det(\boldsymbol{A}) = \left(v_p^2 - v_a^2 cos^2(\theta)\right)\left[v_p^4 - v_p^2(v_a^2 + c_s^2) + v_a^2 v_s^2 cos^2(\theta)\right] = 0, \quad (2.51)$$

where $\boldsymbol{v}_a$ is the Alfvén speed defined

$$\boldsymbol{v}_a = \frac{\boldsymbol{B}_0}{\sqrt{\mu_0 \rho_0}} \equiv \frac{B_z}{\sqrt{\mu_0 \rho_0}}. \quad (2.52)$$

The dispersion relation has three roots defining three MHD wave modes: the Alfvén mode (2.53), slow mode (2.54), and fast mode (2.55):

$$v_p^2 = v_a^2 cos^2(\theta) \quad (2.53)$$

$$v_p^2 = \frac{1}{2}\left[(v_a^2 + c_s^2) - [(v_a^2 - c_s^2)^2 + 4v_a^2 c_s^2 sin^2(\theta)]^{1/2}\right] \quad (2.54)$$

$$v_p^2 = \frac{1}{2}\left[(v_a^2 + c_s^2) + [(v_a^2 - c_s^2)^2 + 4v_a^2 c_s^2 sin^2(\theta)]^{1/2}\right] \quad (2.55)$$

2.4.1 The Alfvén Mode

The Alfvén mode was first postulated by Hannes Alfvén [1942]. It is a purely transverse wave and has no compressional component. This is verified by substituting the Alfvén dispersion relation into equation (2.50) giving the velocity eigenvector

$$\delta v = \left(0, \delta v_y, 0\right), \quad (2.56)$$

which is perpendicular to the wave vector, $\boldsymbol{k}$. Note that because the Alfvén mode is a transverse wave there are no perturbations of the background plasma density or pressure such that P_1=ρ_1=0. Further note that Alfvén group velocity is always parallel to the background magnetic field. Recalling that the magnetic field and wave vector defined by equations (2.48) and (2.49) describe a completely generic magnetic field and wave vector, then the Alfvén dispersion relation can be rewritten as

$$\frac{\omega^2}{k^2} = v_a^2 \frac{(\boldsymbol{k} \cdot \boldsymbol{B})^2}{k^2 B^2} \; or$$
$$\Rightarrow \omega = \pm v_a \frac{(\boldsymbol{k} \cdot \boldsymbol{B})}{B} = \pm v_a k_z, \quad (2.57)$$

and the group velocity is thus given by

$$\boldsymbol{v}_g = \nabla_{\boldsymbol{k}}\omega = \pm v_a \hat{\mathrm{z}}. \tag{2.58}$$

The Alfvén mode is believed to be responsible for establishing the substorm current wedge (SCW) following the initial plasma sheet disturbance during substorm expansion phase onset [*Olson*, 1999]. The initial disturbance at substorm onset may potentially generate Alfvén waves which travel along the background magnetic field carrying a current into the ionosphere. At the ionosphere these Alfvén waves can be reflected, propagating back along the magnetic field where they can be reflected again at either the central plasma sheet or the conjugate ionosphere. The reflection of these Alfvén waves can occur multiple times, each subsequent reflection adding more current to the ionospheric current systems, eventually leading to the full formation of the SCW and intensification of the westward electrojet in the ionosphere. The bouncing Alfvén waves establishing the SCW are believed to be the large amplitude Pi2 ULF waves observed by ground-based magnetometers during the substorm expansion phase onset [*Olson*, 1999]. These Alfvénic disturbances and pulsations associated with the substorm expansion phase onset are discussed in detail in Chapter 5 and Chapter 6.

2.4.2 The Fast and Slow Modes

The fast and slow modes are magnetosonic waves, that is, their dispersion relations are dependent on both the Alfvén speed and the speed of sound in the plasma. Both fast and slow modes can be polarised such that they have a transverse component as well as a compressional component. The fast and slow mode dispersion relations are in general more complicated than the Alfvén mode dispersion. In this section we will consider two limiting cases: $\boldsymbol{k}$ parallel to $\boldsymbol{B}$ and $\boldsymbol{k}$ perpendicular to $\boldsymbol{B}$. In the first case, $\boldsymbol{k}$ =(0,0, k_z) and equations (2.50) and (2.51) simplify to

$$\begin{bmatrix} v_p^2 - v_a^2 & 0 & 0 \\ 0 & v_p^2 - v_a^2 & 0 \\ 0 & 0 & v_p^2 - c_s^2 \end{bmatrix} \begin{bmatrix} \delta v_x \\ \delta v_y \\ \delta v_z \end{bmatrix} = 0, \tag{2.59}$$

$$\det(\boldsymbol{A}) = \left(v_p^2 - v_a^2\right)\left(v_p^2 - c_s^2\right) = 0, \tag{2.60}$$

with roots

$$v_p^2 = v_a^2, \tag{2.61}$$

$$v_p^2 = c_s^2. \tag{2.62}$$

As the name suggests the fast mode has a phase speed greater than the slow mode. Thus the root of the dispersion relation corresponding to the fast and slow mode is dependent on the Alfvén speed and sound speed in the plasma. If $v_a > c_s$ ($v_a < c_s$), then (2.61) corresponds to the fast mode (slow mode) and (2.62) corresponds to the slow mode (fast mode).

The velocity eigenvector corresponding to (2.61) is given by,

$$\delta v = \left(\delta v_x, \delta v_y, 0\right). \tag{2.63}$$

Similar to the Alfvén mode this is a transverse electromagnetic wave. The velocity eigenvector of the root defined by (2.62) is given by,

$$\delta v = (0,0,\delta v_z). \tag{2.64}$$

This eigenvector corresponds to a compressional or longitudinal wave which is similar to a sound wave.

In the second case, $\boldsymbol{k}$=(k_x,0,0) (2.50) and (2.51) simplify to

$$\begin{bmatrix} v_p^2 - v_a^2 - c_s^2 & 0 & 0 \\ 0 & 0 & 0 \\ 0 & 0 & v_p^2 \end{bmatrix} \begin{bmatrix} \delta v_x \\ \delta v_y \\ \delta v_z \end{bmatrix} = 0, \tag{2.65}$$

$$\det(\boldsymbol{A}) = \left(v_p^2 - v_a^2 - c_s^2\right)\left(v_p^2\right) = 0, \tag{2.66}$$

which has only one non-trivial root, corresponding to the fast mode,

$$v_p^2 = v_a^2 + c_s^2. \tag{2.67}$$

The corresponding velocity eigenvector is given by

$$\delta v = (\delta v_x, 0,0). \tag{2.68}$$

This mode has both longitudinal, the velocity perturbation is parallel to the wave vector, and transverse components, the velocity perturbations is perpendicular to the magnetic field. Also note that magnetic field perturbations, the $\delta\boldsymbol{B}$ arising from subbing (2.68) into (2.46), are non-zero and thus this mode is characteristic of both a sound and an electromagnetic wave. Between the limiting cases both the fast and slow modes have transverse and longitudinal components and have characteristics of both sound and electromagnetic waves.

The fast mode is in general believed to be the plasmasheet disturbance generating the Alfvénic disturbance observed during substorm expansion phase onset [*Olson*, 1999]. In both the current disruption (CD) and near-Earth neutral line (NENL) substorm models a compressional or fast mode disturbance is launched following either reconnection in the near tail [*Baker et al.*, 1996], or current disruption in the plasma sheet [*Lui*, 1996]. The fast mode subsequently propagates isotropically throughout the magnetotail and may couple to the background magnetic field, driving Alfvén waves which can be observed as either Pi1 or Pi2 ULF waves during the substorm expansion phase onset. The coupling between the fast and Alfvén modes is discussed in detail in the following section and as well in Chapter 6. Similar to the fast mode the slow mode may also drive Alfvén waves; however, the slow mode is not discussed in detail in this thesis.

2.4.3 Mode Coupling and Field Line Resonances

In a uniform plasma each of the three MHD modes are decoupled. However, in a non-uniform plasma the three modes may become coupled. The most efficient coupling between MHD modes in the magnetosphere occurs in the form of field line resonances (FLRs). In this section we will consider the coupling of the fast and the Alfvén modes in the form of FLRs in a box model magnetosphere [e.g., *Southwood*, 1974] and in the cold plasma limit. In the cold plasma limit, the thermal pressure forces can be neglected in comparison to the ($\boldsymbol{j}\times\boldsymbol{B}$) force. In this limit the slow mode no longer exists, the fast mode propagates isotropically at the Alfvén speed and coupling occurs between the fast and Alfvén modes.

Consider the magnetic field topology shown in Figure 2.3. This is referred to as the box model magnetosphere [e.g., *Southwood*, 1974]. In this model the magnetic field is aligned with the z direction and varies along x (the distance away from the Earth) but is constant with z. The system is bounded above by the ionosphere in the northern hemisphere and below by the southern hemisphere ionosphere. In this model, the ionosphere will be considered to be a perfectly reflecting boundary. The vertical height of the box, l, represents the length of a magnetic field line. Note that in a realistic model of the magnetosphere both the magnetic field and density vary, decreasing with distance away from the Earth. In the simplified box model magnetosphere we will assume that both the magnetic field and density vary with x and are constant in both

the y and z directions. Thus the Alfvén speed, equation (2.52), is only a function of the distance away from the Earth, x.

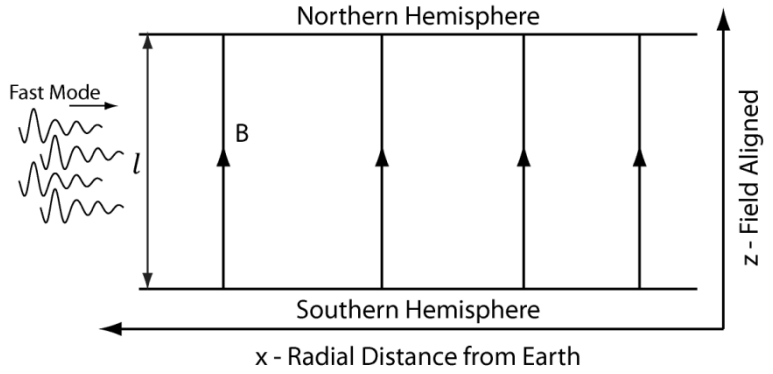

Figure 2.3: Schematic of the box model magnetosphere. Black arrows represent the Earth's magnetic field and the waves represent an incoming fast mode. The Earth is to the right in this schematic.

In the system described above, if we consider that reflection from the ionosphere creates a standing Alfvén wave parallel to the background field, then the wave number k_z is quantized and given by

$$k_z = \frac{n\pi}{l}, \tag{2.69}$$

where n is an integer. In this case the Alfvén dispersion relation becomes

$$\omega_a^2(x) = v_a^2(x)\left(\frac{n\pi}{l}\right)^2. \tag{2.70}$$

This defines the resonant Alfvén frequency of the magnetic field line at the position x. These Alfvénic resonances can be driven by any fast mode wave which has an angular frequency ω_f equal to the Alfvén frequency ω_a. These resonances are referred to as magnetic field line resonances (FLRs).

In a cold plasma the fast mode dispersion relation can be approximated by

$$k_x^2 = \frac{\omega_f^2}{v_a^2(x)} - k_y^2 - k_z^2, \tag{2.71}$$

[*Mann et al.*, 1999]. Note that because the Alfvén speed is a function of x the fast mode can have both spatially oscillatory solutions (2.72) and spatially evanescent solutions (2.73):

$$k_x^2 > 0, \tag{2.72}$$

$$k_x^2 < 0. \tag{2.73}$$

The transition between oscillatory solutions and evanescent solutions occurs at the turning point at a radial distance $x_{T,}$ where

$$\frac{\omega_f^2}{v_a^2(x_T)} = k_y^2 + k_z^2. \tag{2.74}$$

Typically the Alfvén speed in the magnetosphere decreases with increasing distance away from the Earth, thus at distances $x>x_T$ the fast mode is oscillatory and at distances $x<x_T$ the fast mode is evanescent [e.g., *Wright and Mann*, 2006]. If we consider a scenario in which a fast mode emanates from a source in the distant magnetosphere and propagates inward toward the Earth, it can couple to and directly drive an FLR, at the location where $\omega_f=\omega_a(x_R)$. In the box model this occurs in the spatially evanescent region of the fast mode solution.

Typically, the Alfvén wave amplitude peaks at the point x_R where the Alfvén mode resonates at the same frequency as the driving fast mode and decays on either side of the resonant point x_R. The Alfvén wave amplitude profile was first characterised observationally by Samson et al. [1971]. Using a latitudinal array of ground-based magnetometers Samson et al. [1971] showed the amplitude of ULF waves observed on the ground peaked at a certain latitude (a measure of distance away from the Earth in the magnetosphere) and reversed polarisation across the amplitude peak. The authors concluded that the observed pattern was likely the coupling of magnetospheric energy with resonances of the Earth's magnetic field. Southwood [1974] mathematically characterised the resonant response of driven Alfvén waves in the magnetosphere [see also, *Chen and Hasegawa*, 1974] and showed that the theoretical amplitude and polarisation profiles were consistent with the observations of Samson et al. [1971]. The polarisation and amplitude profile predicted by Southwood [1974] is depicted by Figure 2.4. Note that in Figure 2.4 the resonance occurs in the region $x<x_T$ where the fast mode is spatially evanescent.

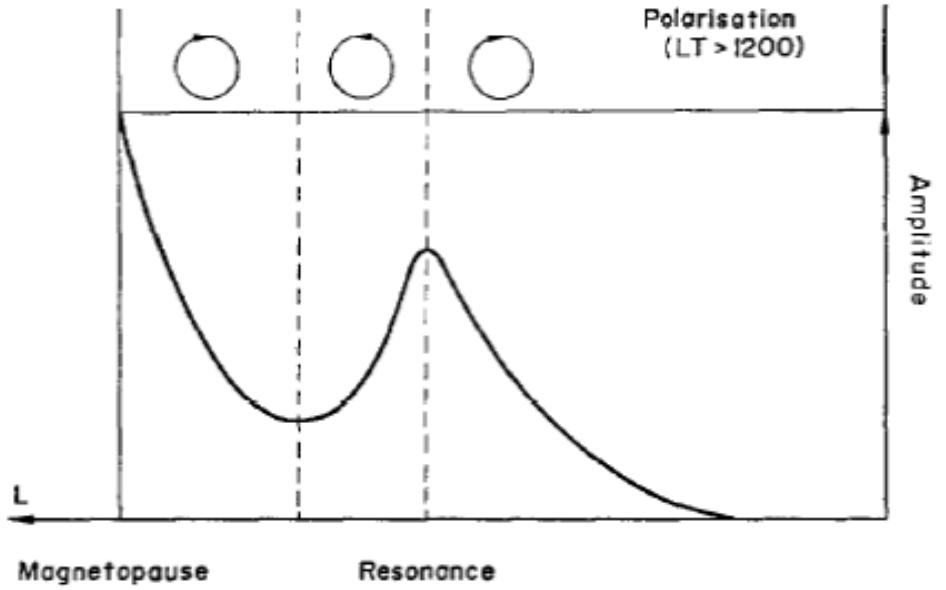

Figure 2.4: A schematic depicting the amplitude profile of a driven Alfvén wave. The top panel displays the observed polarisation of the Alfvén mode. Note the amplitude peaks at the resonant location were the frequency of the driver matches the resonant frequency of the Alfvén wave and across this resonance the Alfvén wave polarisation reverses. Adapted from Southwood [1974].

Coupling between fast and Alfvén waves can also occur in the stretched magnetotail. In this region the magnetic field can become extremely elongated such that a waveguide can form between anti-parallel magnetic fields, and this is referred to as the tail waveguide [*Wright and Mann*, 2006]. The tail waveguide is bounded in the z-direction by the lobe magnetic field which is characterised by open magnetic field lines and low density plasma. The center of the waveguide is the central plasma sheet (CPS), a region of warm and dense plasma where magnetic field lines are closed. The transition region between the lobe field and the CPS is the plasma sheet boundary layer (PSBL). In the PSBL the magnetic field is extremely stretched but remains closed and the plasma density decreases as a function of the distance away from the CPS. As a consequence the local Alfvén speed in the tail waveguide increases in the z-direction as a function of the distance away from the CPS. A schematic of the tail waveguide is shown in Figure 2.5 [*Wright and Mann*, 2006]. Note that the coupling in the tail waveguide is in general more complicated than that in the box model magnetosphere previously discussed.

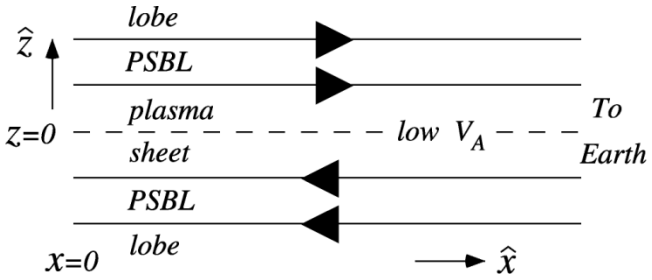

Figure 2.5: A schematic of the tail waveguide. Black arrows represent the direction of the Earth's magnetic field. Figure from Wright and Mann [2006].

In the tail waveguide a fast mode propagating down the waveguide at a parallel group velocity v_{gx} can couple to Alfvén waves at the point z_R where the local Alfvén speed $v_{\mathrm{a}}(\mathrm{z})$ is equal to the parallel component of the fast mode phase speed $v_{p\,\mathrm{x}}$, equation (2.75) [*Wright et al.*, 1999]. This coupling can produce an Alfvén wave which propagates down the tail waveguide at the local Alfvén speed [e.g., *Wright and Mann*, 2006].

$$v_a(z_R) = v_{px}. \tag{2.75}$$

Similar to the box model magnetosphere, if we consider an Alfvén wave propagating parallel to the background magnetic field then the Alfvénic wave number is directed along the magnetic field, in this case the x-direction. At the resonant location z_R the parallel or x-component of the fast mode wave number is equal to Alfvénic wave number ($k_{ax} \equiv k_{fx} \equiv k_x$) and the frequency of the Alfvén wave is given by [*Wright and Mann*, 2006],

$$\omega_a(z_R) = v_a(z_R)k_x. \tag{2.76}$$

Moreover the solution to the fast mode dispersion relation has both spatially evanescent and spatially oscillatory solutions, depending on the values of k_{x}, k_{y}, and k_{z}, see for example (2.71). In the tail waveguide the transition between spatially oscillatory and spatially evanescent solutions in the fast mode dispersion relation occurs at the point z_T, which at times can be inside of the resonant location z_R for a given fast mode wave number $k=(k_{\mathrm{x}},k_{\mathrm{y}},k_{\mathrm{z}})$. Figure 2.6 is a schematic illustrating three different fast mode ray paths for three different fast mode wave numbers in the upper half of the tail waveguide [*Allan and Wright*, 1998]. Rays 1, 2 and 3 in Figure 2.6 are fast modes with different parallel wave numbers. In this example, Ray 3 couples to an Alfvén mode at the resonant location z_R. Note that in general the excited Alfvén wave propagates down the

tail waveguide faster than the fast mode wave since the Alfvén speed is typically greater than v_{gx} for the fast mode [*Wright and Mann*, 2006]. The initial source of wave energy illustrated in Figure 2.6 could potentially be the onset of a magnetic substorm exciting fast mode waves which propagate down the tail waveguide and which themselves excite Alfvén waves which propagate along the background magnetic field toward the Earth [*Wright and Mann*, 2006]. The tail waveguide is discussed in Chapter 6, and the coupling of the fast and Alfvén modes is also discussed in Chapter 6 Specifically in relation to the comparisons between the waveform observed in ground-based Pi2 pulsations and a high-velocity earthward plasma flow in the CPS.

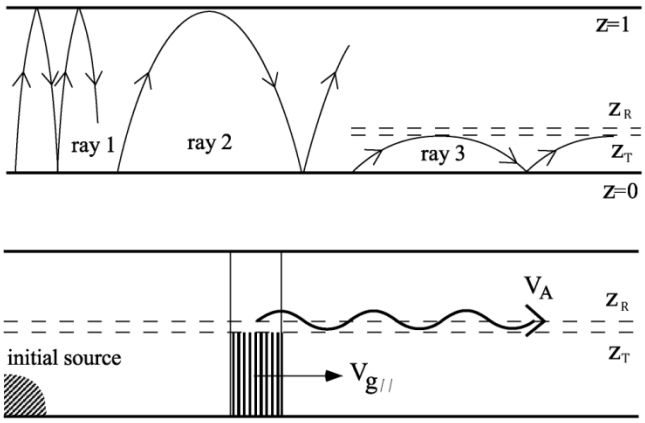

Figure 2.6: An illustration of the ray paths for three fast mode waves with different wave numbers. The point z_R characterises the location where the fast and Alfvén modes can couple and z_T is the turning point for the fast mode whose ray path is characterised by ray 3. The boundary z=0 is the CPS and z=1 is toward the lobe. Figure from Allan and Wright [1998].

Chapter 3 Instrumentation and Analysis

3.1 Introduction

This Chapter introduces the instrumentation, both ground-based and in-situ, used to monitor the Earth's magnetic field and the plasma environments pervading the magnetosphere. The techniques used to analyse the data sets provided by these instruments are also introduced.

3.2 Ground-based Magnetometers

When studying the Earth's magnetic field, ground-based magnetometers provide invaluable insight into the physical processes and phenomena occurring within the magnetosphere since they can monitor from multiple locations magnetic disturbances arising in the magnetosphere. Fluxgate magnetometers measure the D.C. component of the Earth's magnetic field and provide the ability to identify ULF waves and FLRs in the magnetosphere, the onset of magnetic substorms, and even the location of the SCW in the ionosphere. Fluxgate magnetometers were first developed in the 1930's and are in essence composed of two identical driving (or primary) cores that are coiled in wire and surrounded by a secondary (or sensor) core which is also coiled in wire. A schematic of a fluxgate magnetometer is shown in Figure 3.1 (a).

The operation of fluxgate magnetometers is based on magnetic induction and a principle known as magnetic saturation. When a large enough current is driven through the coils of the primary cores the magnetisation in the cores saturates. By applying an A.C. current of frequency f across the primary coils, such that the coils saturate during the current cycle (Figure 3.1 (b) left, i and ii), then the resulting magnetic field and magnetic flux within the cores alternates with the driving current between maximum and minimum values at the frequency f. Utilising two primary cores, aligned anti-parallel, generates two magnetic fields in which the magnetic flux from either core is 180° out of phase (Figure 3.1 (b) left, i and ii) such that the net magnetic field and magnetic flux within the primary cores is always zero (Figure 3.1 (b) left, iii).

When an external field is introduced to the fluxgate system the component of the magnetic field parallel to the external field is offset such that the magnetisation of one

of the primary cores saturates quicker than that of the other. As a result the net magnetic flux within the secondary core is no longer zero and oscillates at a frequency of 2f (Figure 3.1 (b) right, iii). The time varying magnetic flux in turn induces a voltage in the secondary core which also oscillates at 2f (Figure 3.1 (b) right, iv). The second harmonic (2f) component of the induced voltage and phase of the induced voltage is proportional to the magnitude and direction of the external field parallel to the primary cores. With three sets of mutually perpendicular fluxgate cores a fluxgate magnetometer is capable of measuring the full three-vector external magnetic field. Figure 3.1 (b) depicts the response of a fluxgate magnetometer with and without an external field present (right and left respectively).

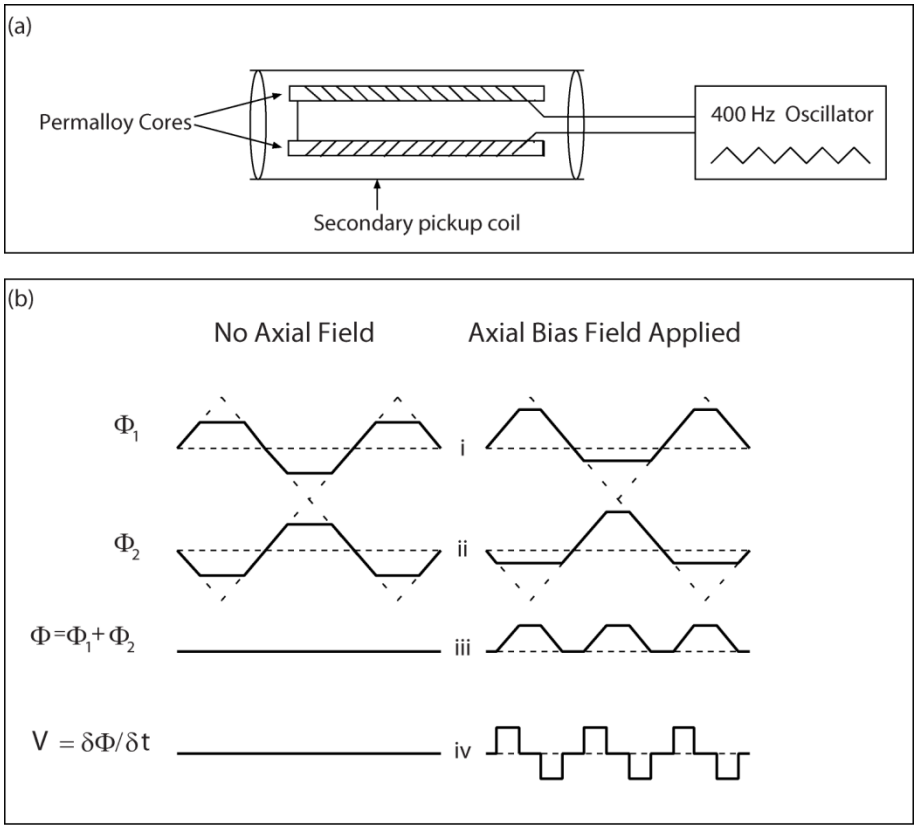

Figure 3.1: (a) A schematic of a fluxgate magnetometer. (b)The response of a fluxgate with no external magnetic field (left) and in the presence of an external magnetic field (right). Panels (i) and (ii) illustrate the magnetic flux generated by the magnetisation of primary coil 1 and 2 respectively. (iii) Shows the net magnetic flux in the fluxgate system and (iv) the induced voltage generated by a time varying flux in the secondary core. Image courtesy of David Milling.

Typically fluxgate magnetometers provide measurements of the Earth's magnetic field in units of nano-Tesla (nT) with a cadence of 0.5-1 s (depending on the instrument specifications) in one of two coordinate systems: geographic or geomagnetic. In the geographic coordinate system the axes are aligned with the directions of the geographic poles, with x pointing North, y East and z vertically downward. In the geomagnetic coordinate system the axes are aligned relative to the Earth's magnetic field; the H-direction is aligned with, and points toward, geomagnetic north, the D-direction to geomagnetic East and z defines the vertical direction (pointing downwards, same as in geographic coordinates). Note, because the z-direction is the same in both geomagnetic and geographic coordinates the x-y and H-D axes define the same two-dimensional plane and the axes' are related by a rotation about the z axis such that

$$H = xcos(\varphi) + ysin(\varphi), \tag{3.1}$$

$$D = ycos(\varphi) - xsin(\varphi), \tag{3.2}$$

where φ is the magnetic declination, the angle between geomagnetic north (true north) and geographic north.

Figure 3.2 shows the location of fluxgate magnetometers deployed throughout North America from six separate magnetometer arrays. The red triangles are magnetometers which are apart of the Canadian Array for Realtime Investigation of Magnetic Activity [*Mann et al.*, 2008] (CARSIMA, formerly operated as CANOPUS, the Canadian Auroral Network for the OPEN Program Unified Study magnetometer array [*Rostoker et al.*, 1995], prior to 1st April 2005) which is operated by the Space Physics group at the University of Alberta. The blue and white squares are fluxgates from the THEMIS GBO array (Time History of Events and Macroscale Interactions during Substorms Ground-Based Observatory) [*Russell et al.*, 2008]. The THEMIS GBO magnetometer array is operated through the University of California Los Angeles by the Institute of Geophysics and Planetary Physics (IGPP). The orange circles are magnetometers from the Canadian Magnetic Observatory System (CANMOS) operated by Natural Resources Canada (NRCAN). The purple diamonds are fluxgates operated by the University of Alaska, as part of the Geophysical Institute Magnetometer Array (GIMA), and the yellow diamond

is an IGPP magnetometer operated through the University of California. Combined, the six arrays provide unprecedented coverage of the magnetic signatures seen on the ground and driven by disturbances in the Earth's magnetosphere. This coverage is provided by over sixty fluxgates spanning ~50 degrees in latitude and a ~100 in longitude. Table 3.1-Table 3.6, found at the end of this Chapter, summarise the geographic and geomagnetic locations of all the magnetometers shown in Figure 3.2.

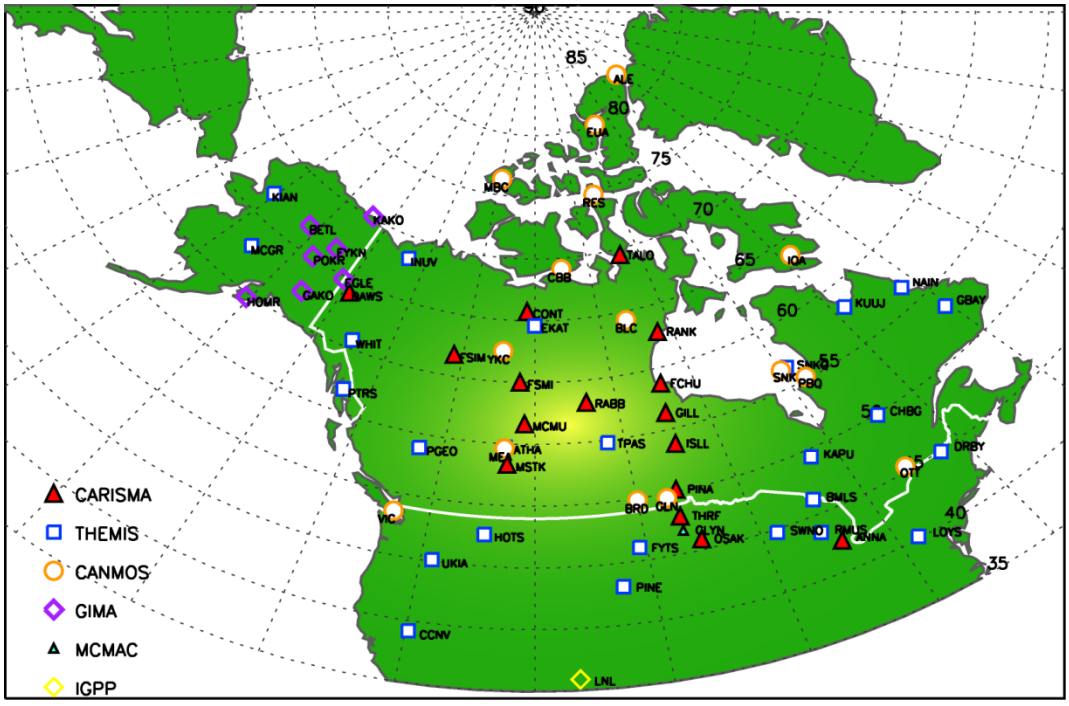

Figure 3.2: Location of fluxgate magnetometers providing observations of the Earth's magnetic field and utilised throughout this thesis.

3.3 The Imager for Magnetopause-to-Aurora Global Explorations (IMAGE) Satellite

In-situ observations of the aurora from satellites, while often limited in spatial and temporal resolution when compared to ground-based observations, provide the most global characterisation of the auroral oval without the pitfalls of ground-based instrumentation such as cloudy skies and even the build up of snow. The Imager for Magnetopause-to-Aurora Global Exploration (IMAGE) spacecraft is a global imaging satellite deployed in order to characterise the response of the magnetosphere to the solar wind by imaging the auroral oval in both the southern and northern hemispheres.

IMAGE is host to seven different instruments, though the only one of relevance in this thesis is the Far Ultraviolet Imager (FUV).

The FUV instrument boasts two auroral imagers, the Wideband Imaging Camera (WIC) and the Spectrographic Imager (SI) [*Mende et al.*, 2000]. WIC is a broadband camera measuring auroral emissions between approximately 140-190 nm. The WIC imager has a resolution of 256x256 pixels, and at apogee the size of a pixel corresponds to roughly $(50\ km)^2$. SI is narrow band imager characterising auroral emissions at and near 135.6 nm. The imager has a 128x128 pixel resolution, each pixel corresponding approximately to $(100\ km)^2$ when the spacecraft is at apogee [*Frey et al.*, 2004]. Both WIC and SI image the aurora oval for ~5-10s with a nominal two minute cadence, the spin period of the IMAGE spacecraft.

IMAGE was launched on 25 March 2000 and officially died on 18 December 2005 when communications between the satellite and ground-based operations were lost. Though new data from IMAGE-FUV instrument is no longer available during its operation the IMAGE spacecraft provided the unique opportunity to characterise the global expansion of the aurora during the substorm expansion phase. In just under six years of operation the IMAGE-FUV instrument observed over 4000 substorms. These substorms were identified by Frey [*Frey et al.*, 2004] and have been compiled into an online substorm database providing the UT time and geographic and geomagnetic location of the global-scale auroral intensification. The substorm database is used to initially identify substorms in Chapter 4 and provides the basis for the statistical study in Chapter 7.

3.4 Geotail Satellite

The Geotail spacecraft is a joint venture between the Institute of Space and Astronautical Science (ISAS) in Japan, the Japanese Aerospace Exploration Agency (JAXA), and the National Aeronautics and Space Administration (NASA). Geotail was designed and built by ISAS, and was launched on 24 July 1992. The primary objective of the Geotail satellite is to further our understanding of the Sun-Earth connection by providing a comprehensive suite of instruments to study the plasma and magnetic and electric fields of the magnetosphere at distances between ~20-200 R_E in the magnetotail. While there are several instruments onboard Geotail with which to

characterise the magnetic and electric fields as well as plasma dynamics in the magnetosphere, three are of most relevance here: the Comprehensive Plasma Instrument (CPI) [*Frank et al.*, 1994], the Low Energy Plasma instrument (LEP) [*Mukai et al.*, 1994] and the Magnetic Field instrument (MGF) [*Kokubun et al.*, 1994].

The CPI instrument is a three-dimensional plasma analyzer which determines the three-dimensional velocity distribution, number density as well as the temperature of the electron and ions with energies in the range of 1 eV-50 keV [*Frank et al.*, 1994]. The CPI instrument has a 64 s cadence, and although this resolution is often inadequate for studying ULF waves, the electron moments, number densities and plasma temperature are unique to CPI and provide an excellent data set with which to characterise bulk aspects of the magnetospheric plasma. LEP similar to CPI is a three-dimensional particle detector. However LEP measures the three-dimensional distribution and moments of ions in the energy range 7 eV-42 keV with a cadence of 12 s [*Mukai et al.*, 1994]. The high temporal resolution of the LEP particle instruments makes it ideal for studying shorter period ULF waves, such as the impulsive ULF waves observed during the substorm expansion phase onset (see 1.5.3). The MGF instrument is a fluxgate magnetometer which measures the vector magnetic field observed at the location of the spacecraft with a 3 s cadence, providing excellent temporal and spatial resolution of the magnetic field when characterising short period fluctuations of the magnetic field [*Kokubun et al.*, 1994]. The instruments described above and their data sets from the Geotail satellite are extensively used in Chapter 6 to study the relationship between ground-based observations of Pi2 ULF waves and bulk plasma flows in the magnetotail.

3.5 Time Series Analysis

In order to properly study the time evolution of various magnetospheric phenomena observed by both ground-based and in-situ instruments we must be able to identify similarities between waves and wavepackets, isolate and identify specific signals, as well as characterise the amplitude or frequency spectrum of a waveform. This section introduces some time series analysis techniques that will aid in characterising and understanding the evolution of a time series, with specific application to studying magnetic substorms and ULF waves.

During substorms ULF waves are often superimposed on large amplitude and slowly varying background fields. Moreover, multiple ULF wavepackets can be observed with differing frequencies, amplitudes and phase characteristics. While both the background field variations and the ULF waves observed within a single time series can both be important, it is often advantageous to be able to separate the background variations from the various waveforms observed. A simple method for isolating waveforms is to apply a bandpass filter to the data set. A bandpass filter, and filters in general, highlight specific frequencies in a series by convolving the series with an impulse response function or kernel, ultimately zeroing or removing unwanted frequencies from the signal. A filter can be as simple as removing a running mean from a signal or can be specifically designed to highlight or remove specific waveforms from a time series. Though filters are a relatively standard data processing technique they are invaluable when studying ULF waves and magnetic substorms, and specifically for identifying and separating Pi1 and Pi2 pulsations observed during the substorm expansion phase.

Identifying the dominant frequency component of a wavepacket and characterising the frequency spectrum of a time series is also vital when characterising ULF waves and waves in general. The Fast Fourier Transform (FFT) is a method to transform a signal from the time domain to the frequency domain, providing an estimate of the spectrum of frequencies contained within a given time series. The forward and inverse FFT of a discretely sampled signal x_n with N points is given by equations (3.3) and (3.4), respectively.

$$F_{\mathrm{k}} = \frac{1}{N}\sum_{n=0}^{N-1} x_n \exp\left[\frac{-2\pi i \mathrm{k} n}{N}\right], \tag{3.3}$$

$$x_n = \sum_{\mathrm{k}=0}^{N-1} F_{\mathrm{k}} \exp\left[\frac{2\pi i \mathrm{k} n}{N}\right], \tag{3.4}$$

where k is the discrete wave number, an integer ranging from [0: N-1] defining both positive ($\mathrm{k} \leq N/2$) and negative frequencies ($\mathrm{k} > N/2$). If we assume F_{k} is symmetric then we only need to consider the range of wave numbers between [0: $N/2$] defining the positive frequency range. The relationship between frequency and wave number is then given by

$$f_{\mathrm{k}} = \frac{\mathrm{k}}{N\Delta t}, \tag{3.5}$$

where Δt is the sampling cadence of the signal x_n. Note, in any FFT the sampled frequencies are discrete and limited by the Nyquist frequency, the largest frequency which can be accurately measured in a discrete time series with a cadence of Δt, defined when k=$N/2$ such that

$$f_{Nyquist} = \frac{1}{2\Delta t}. \tag{3.6}$$

In general the function F_{k} is complex. However the power of a signal is a real valued function and is a measure of the amplitude of the signal at any frequency. The discrete power is defined by

$$\begin{aligned} \mathcal{P}_{\mathrm{k}} &= 2|F_{\mathrm{k}}|^2 for\ \mathrm{k}\epsilon\left[1{:}\,{}^{N}/_{2} - 1\right], \\ \mathcal{P}_{\mathrm{k}} &= |F_{\mathrm{k}}|^2 for\ \mathrm{k} = 0\ and\ {}^{N}/_{2}. \end{aligned} \tag{3.7}$$

The factor of two, for power in the range of [1:N/2-1], accounts for power in both the positive and negative frequencies. Power spectral density (PSD) is similar to power in that it quantifies the frequency content of a real valued signal. However, unlike the discrete power, PSD satisfies Parseval's theorem – the sum of a function is proportional to the sum of its transform. The PSD of a signal can be defined in three different ways, first column, each of which satisfy Parseval's theorem, second column, of equations (3.8), (3.9) and (3.10) [*Press et al.*, 1992],

Power Spectral Density	Parseval's Theorem	Name	
$PSD_{\mathrm{k}} = \mathcal{P}_{\mathrm{k}}$	$\sum_{\mathrm{k}=0}^{\mathrm{N}/2}(PSD_{\mathrm{k}}) = \frac{1}{\mathrm{N}}\sum_{\mathrm{m}=0}^{\mathrm{N}-1}\lvert x_n\rvert^2$	Mean Squared Amplitude	(3.8)
$PSD_{\mathrm{k}} = \mathrm{N}\mathcal{P}_{\mathrm{k}}$	$\sum_{\mathrm{k}=0}^{\mathrm{N}/2}(PSD_{\mathrm{k}}) = \sum_{n=0}^{\mathrm{N}-1}\lvert x_n\rvert^2$	Sum Squared Amplitude	(3.9)
$PSD_{\mathrm{k}} = \frac{1}{\Delta f}\mathcal{P}_{\mathrm{k}}$	$\sum_{\mathrm{k}=0}^{\mathrm{N}/2}(PSD_{\mathrm{k}}) = \frac{1}{\mathrm{N}\Delta f}\sum_{n=0}^{\mathrm{N}-1}\lvert x_n\rvert^2$	Time-Integral Squared Amplitude	(3.10)

Note that though the definitions of power and PSD are very different the broad characteristics of each are the same, for instance the location of local maxima and

minima. This often leads to equation (3.7) and the definitions of PSD in equations (3.8)-(3.10) being used interchangeably. In this thesis PSD will be specifically defined by equation (3.10), unless otherwise stated.

Typically the FFT of a discretely sampled signal produces a reasonable estimate of the power or frequency spectrum. However, for any given power bin, power can leak into a neighbouring bin, thus reducing the absolute resolution of the power spectra. This is referred to as "leakage". Estimates of the power spectrum can be improved by windowing the data set; that is, multiplying the time series by a windowing function. Further, averaging over adjacent power bins can minimise or reduce the leakage over a given frequency bin. Note that when windowing a data set the absolute power in a given spectral peak can be reduced and a correction factor must be applied to the power spectrum such that

$$\begin{aligned} \mathcal{P}_{\mathrm{k}} &= \frac{2|F_{\mathrm{k}}|^2}{W} \; for\; \mathrm{k} \neq 0 \; or \; {}^{N}/_{2}, \\ \mathcal{P}_{\mathrm{k}} &= \frac{|F_{\mathrm{k}}|^2}{W} \; for\; \mathrm{k} = 0 \; or \; {}^{N}/_{2}. \end{aligned} \tag{3.11}$$

where W is a correction factor dependent on the windowing function used. There are several different types of windows which can be used to improve the power spectral estimates. This thesis utilises the Hanning window [*Press et al.*, 1992] and a corresponding correction factor of 0.3745.

Not only is the FFT able to characterise the power and frequency spectrum of a signal, it is also able to provide an estimate of how similar the frequency content of two signals is. This is referred to as the coherence spectrum. Consider two time series x_n and y_n with Fourier transforms $F_{\mathrm{k},x}$ and $F_{\mathrm{k},y}$, then the coherence between x_n and y_n at each discrete frequency is defined by

$$C_{\mathrm{k},xy} = \frac{\left|F^*_{\mathrm{k},x} F_{\mathrm{k},y}\right|}{\left[\left(F^*_{\mathrm{k},x} F_{\mathrm{k},x}\right)\left(F^*_{\mathrm{k},y} F_{\mathrm{k},y}\right)\right]^{1/2}}, \tag{3.12}$$

where the superscript * denotes the complex conjugate. The coherence spectrum in the frequency domain is similar to a correlation coefficient in the time domain. However, coherence ranges from [0:1] and provides an estimate of how similar the amplitude and waveforms of two signals are at a given frequency f_{k}. Note that unlike the correlation

coefficient the coherence does not take into account phase, thus phase shifted signals can have a low correlation but a high coherence. This is often important when studying propagating or non-stationary waves.

Finally the Hilbert transform provides a means with which to define the instantaneous phase of a narrowband signal. The Hilbert transform shifts the phase of a signal by 90 degrees, and this is readily accomplished by multiplying the first half of the FFT of a signal ($k \leq N/2$) by i, the second half ($k > N/2$) by $-i$, and performing the inverse FFT, producing a new signal $H_n(x_n)$. The resulting Hilbert transformed signal $H_n(x_n)$ and the original signal x_n can then be used to calculate the instantaneous phase of a signal

$$\phi_n = \arctan\left[\frac{H_n(x_n)}{x_n}\right]. \quad (3.13)$$

The Hilbert transform is ideal for differentiating between individual wavepackets, whose phase varies roughly linearly with time and where separate wavepackets are often separated by a phase skip as well as for examining broadband or low amplitude noise whose phase profile has no coherent structure. The instantaneous phase can also be very useful for identifying the onset or beginning of wavepackets and ULF signals.

3.6 Magnetometer Locations

The following section summarises the geographical and geomagnetic location (in degrees) and L-shell (in R_E) value of the magnetometers from each of the magnetometer arrays shown in Figure 3.2. The L-shell is the distance from the centre of the Earth to the projection of the magnetometer location in the magnetic equatorial plane, mapped along an assumed dipole magnetic field in units of Earth radii. Note that the L-shell value is proportional to the latitude of a magnetometers station. For high-latitude stations accurate measure of the L-shell cannot be obtained. A value of NA is placed in the column for magnetometer stations where the L-shell cannot be defined.

3.6.1 CANMOS

Full details of the CANMOS magnetometer array can be found at the CANMOS website located at http://gsc.nrcan.gc.ca/geomag/obs/index_e.php.

Table 3.1: Geographic and geomagnetic location of the CANMOS magnetometers

Station	Geographic		Geomagnetic		
	Latitude	Longitude	Latitude	Longitude	L-shell
ALE	82.5	297.6	87.2	88.6	NA
EUA	80.0	274.1	87.9	338.2	NA
MBC	76.3	240.6	80.9	277.6	NA
RES	74.7	265.1	82.8	322.9	NA
CBB	69.1	255.0	76.8	311.4	NA
BLC	64.3	264.0	73.3	329.1	12.3
IQA	63.8	291.5	72.1	14.5	10.8
YKC	62.5	245.5	69.2	302.3	8.1
SNK	56.5	280.8	66.2	357.0	6.3
PBQ	55.3	282.4	65.0	359.4	5.7
MEA	54.6	246.7	61.8	307.2	4.5
BRD	49.9	260.0	59.3	326.1	3.9
GLN	49.7	262.9	59.4	330.3	3.9
VIC	48.5	236.6	53.7	297.2	2.9
OTT	45.4	284.4	50.5	298.1	2.5

3.6.2 CARISMA

Detailed information about the CARISMA magnetometers can be found at http://www.carisma.ca and in Mann et al. [2008].

Table 3.2: Geographic and geomagnetic location of the CARIMSA magnetometers

Station	Geographic		Geomagnetic		
	Latitude	**Longitude**		**Latitude**	**Longitude**
TALO	69.5	266.5	78.3	331.0	NA
CONT	65.8	248.8	72.9	304.9	11.7
DAWS	64.1	220.9	66.0	273.9	6.1
RANK	62.8	267.9	72.2	336.0	10.9
FSIM	61.8	238.8	67.3	294.3	6.8
FSMI	60.0	248.1	67.3	307.0	6.8
FCHU	58.8	265.9	68.4	333.5	7.5
RABB	58.2	256.3	66.8	319.1	6.6
MCMU	56.7	248.8	64.2	309.2	5.4
GILL	56.4	265.4	66.1	333.1	6.2
ISLL	53.8	265.3	63.6	333.3	5.1
MSTK	53.4	247.0	60.7	307.9	4.2
PINA	50.2	264.0	60.0	331.8	4.1
THRF	48.0	263.6	57.8	331.4	3.6
OSAK	45.9	264.9	55.9	333.5	3.2

Station	Geographic		Geomagnetic		
	Latitude	Longitude		Latitude	Longitude
ANNA	42.4	276.1	52.9	349.5	2.8

3.6.3 GIMA

For additional information on the GIMA magnetometers see

http://magnet.gi.alaska.edu/.

Table 3.3: Geographic and geomagnetic location of the GIMA magnetometers

Station	Geographic		Geomagnetic		
	Latitude	Longitude	Latitude	Longitude	L-shell
KAKO	70.1	216.4	71.1	264.7	9.7
BETL	66.9	208.5	66.5	260.9	6.4
FYKN	66.6	214.8	67.3	266.5	6.8
POKR	65.1	212.6	65.4	265.7	5.9
EGLE	64.8	218.8	66.2	271.4	6.3
GAKO	62.4	214.8	63.1	269.3	5.0
HOMR	59.7	209.5	59.3	266.1	3.9

3.6.4 MCMAC

Detailed information about the MCMAC array and the GLYN magnetometer can be found at http://spc.igpp.ucla.edu/mcmac/index.html

Table 3.4: Geographic and geomagnetic location of the MCMAC magnetometer

Station	Geographic		Geomagnetic		
	Latitude	Longitude	Latitude	Longitude	L-shell
GLYN	46.9	263.6	56.7	331.6	3.4

3.6.5 IGPP

Full details on the IGPP LNL magnetometer can be found at

http://sprg.ssl.berkeley.edu/UCLANLMAG/

Table 3.5: Geographic and geomagnetic location of the IGPP magnetometer

Station	Geographic		Geomagnetic		
	Latitude	Longitude	Latitude	Longitude	L-shell
LNL	35.9	253.3	44.2	319.3	2.0

3.6.6 THEMIS

For more information on the THEMIS magnetometer array and magnetometers see http://www-ssc.igpp.ucla.edu/uclamag/ and Russell et al. [2008]

Table 3.6: Geographic and geomagnetic location of the THEMIS magnetometers

Station	Geographic		Geomagnetic		
	Latitude	Longitude	Latitude	Longitude	L-shell
INUV	68.3	226.7	71.2	276.2	9.8
KIAN	67.0	199.6	65.2	253.8	5.8
EKAT	64.6	250.0	71.9	307.3	10.6
MCGR	63.0	204.4	61.8	260.1	4.6
WHIT	60.7	224.9	63.4	279.8	5.1
KUUJ	58.2	291.5	66.8	13.1	6.5
PTRS	56.8	226.8	59.9	283.7	4.0
SNKQ	56.5	280.8	66.2	357.0	6.3
NAIN	56.5	298.2	64.0	21.9	5.3
TPAS	54.8	258.1	63.8	322.6	5.2
ATHA	54.7	246.7	61.9	307.2	4.6
PGEO	53.9	237.4	59.2	296.3	3.9
GBAY	53.3	299.6	60.6	23.0	4.2
CHBG	49.9	285.6	59.5	3.6	3.9
KAPU	49.4	277.6	59.6	351.9	4.0
HOTS	47.6	245.3	54.6	307.5	3.0
BMLS	46.2	275.7	56.6	349.0	3.3
FYTS	46.1	259.4	55.5	325.8	3.2
UKIA	45.1	241.0	51.2	303.1	2.6
DRBY	45.0	287.9	54.4	6.4	3.0
SWNO	44.8	271.4	55.2	342.8	3.1
RMUS	43.6	274.8	54.0	347.7	3.0
PINE	43.1	257.4	52.2	323.5	2.7
LOYS	40.2	281.6	50.5	357.2	2.5
CCNV	39.2	240.2	45.0	303.7	2.0

Chapter 4 Identifying the Onset of ULF Waves

4.1 Introduction

Typically individual ULF wavepackets have a coherent structure such that their phase varies approximately linearly with time and the wavepacket has a well-defined amplitude profile such that the waveform initially rises out of low amplitude and phase incoherent background noise, increases in amplitude reaching a maximum value and subsequently decays back toward background noise levels. In general it is relatively easy to identify ULF wavepackets; however, defining the time onset of a ULF wavepacket (i.e., the initial point in time when the wave is observed) is inherently more difficult as the initial amplitude of the wave can be comparable to background or instrument noise levels or fluctuations driven by pre-existing magnetospheric and ionospheric current systems. In this Chapter three methods will be discussed and tested in order to develop a reliable and robust technique with which to characterise the onset of ULF waves, in particular the onset of impulsive ULF waves during magnetospheric substorms.

Impulsive Pi1 and Pi2 ULF waves are typically observed during the initial seconds of the substorm expansion phase. This Chapter addresses whether these impulsive ULF waves can be used as a reliable phenomenon with which to characterise the temporal onset of a magnetic substorm. The vast number of magnetometers deployed throughout North America (see Figure 3.2) provide an unprecedented spatial coverage of the auroral zone and hence the ability to indirectly probe the entire night-side magnetosphere during substorm onset. The ability to identify the onset of ULF waves, coupled with the immense spatial coverage of magnetometers provides a unique opportunity to locate and time the initial ULF disturbance following substorm expansion phase onset.

In the following sections three techniques for objectively identifying substorm onset will be examined. Each method will be tested during an isolated ULF wave event observed by the THEMIS-A spacecraft and during a magnetic substorm observed by the RABB magnetometer on the ground in order to determine the most reliable and robust method for timing and locating substorm onset. In the subsequent Chapter, the method chosen best will be further developed and validated by comparing the characteristics of

ULF onset to observed optical signatures of substorm onset and to the historical optical definition of substorm onset [*Akasofu*, 1964].

4.2 Techniques for Identifying ULF onset

4.2.1 Phase Skips

ULF waves in both the ionosphere and the magnetosphere are often observed as groups of wavepackets with a well-defined phase and roughly constant frequency, separated by phase skips which can be characterised as sudden and discrete changes in the phase of the wave [e.g., *Chi and Russell*, 1998]. Phase skips in ULF waves have been shown to be the result of impulsive disturbances in the magnetosphere or explosive sources of wave energy [e.g., *Mier-Jedrzejowicz and Hughes*, 1980] as well as due to wave beating or phase mixing between waves of similar frequencies [e.g.,*Waters*, 2000]. Since substorms are both impulsive in nature and an explosive source of energy in the magnetosphere, phase skips should be a promising approach for identifying the onset of ULF waves during the substorm expansion phase. Utilising phase and phase skips, the onset of a ULF wave will be defined by the initial phase skip in the signal, calculated as the temporal rate of change of the phase profile of the wave (see equation (3.13)), followed by a linear phase relation characteristic of a sinusoidal wave. Note that these phase skips are typically indicative of wavepacket structure in an isolated signal with a discrete frequency or period. Thus in order to accurately identify the phase skip and the onset of the ULF wave, the signal must be narrow-band filtered to remove any adjacent frequency or background signals.

4.2.2 ARIMA Modeling and Phase

The second method for identifying the onset of ULF waves utilises a consideration of phase and an estimate of the amplitude of the background fluctuations. For a pseudo-stationary time series, an autoregressive integrated moving average (ARIMA) can be used to model or forecast a time series. The ARIMA model is purely statistical and models future data points based on past data points [*Press et al.*, 1992]. The modeled time series can in turn be used to estimate the amplitude of the background noise fluctuations (or residuals), the difference between the actual and modeled time series at any point in time. A statistical definition of the onset of ULF wave phenomena can then

be defined by the amplitude of the standard deviation of the residuals (σ_w) and the phase of the ULF wave. Specifically, the onset of ULF wave phenomena will be defined by the initial wave period with a peak-to-peak amplitude greater than $4\sigma_w$ and an approximately linear phase profile. These two constraints ensure that the observed oscillation is characteristic of a sinusoid and provides a 98% confidence level that the amplitude of the observed oscillations are not the intrinsic noise fluctuations of the observed time series.

4.2.3 The Discrete Wavelet Transform

The third method examined for determining the onset of ULF waves utilises a discrete wavelet transform (DWT), with a Meyer wavelet basis [*Meyer*, 1989], which decomposes a signal into wavelet coefficients localised in both frequency (*j*) and time (*k*). The wavelet coefficients characterise both the amplitude of the wave and the coherency of the signal and specified wavelet used in the DWT as such wavelets provide an excellent analytical tool for analysing the localised characteristics of a non-stationary time series in both the frequency and time domains. Moreover it has been shown that wavelets are excellent for studying ULF waves observed during the expansion phase of substorms [e.g., *Nose et al.*, 1998]. The onset of ULF waves can be defined in both the time and frequency domains by identifying the first wavelet band whose amplitude continuously rises above a predefined threshold. This threshold can be defined specifically for each wavelet band, and thus all frequencies within a signal can be studied and an onset time determined from the entire ULF spectrum. The thresholds utilised here are defined as the mean of the wavelet coefficients plus two standard deviations of the coefficients calculated from a "quiet" period of the time series during which there is limited ULF wave activity. This gives approximately a 98% confidence level that the wavelet band characterising the onset of ULF waves is a statistically significant signal, not the result of random noise fluctuations inherent to the time series. In testing, we have found that this threshold works well for the ULF waves observed at the expansion phase onset.

4.3 In-situ Case Study: Isolated ULF Wave Event on 6th March 2007

On the 6th March 2007 the THEMIS-A probe, located in the night-side magnetosphere, observed a large-amplitude and monochromatic oscillation of the Earth's magnetic field, indicative of a continuous pulsation referred to as a Pc ULF wave. The ULF wave was

observed in all three components of the magnetic field, the parallel component (parallel to the Earth's ambient field), the azimuthal component (directed east) and the radial component (which completes the right handed coordinate system). This event will be used to develop and illustrate the three methodologies outlined in 4.3 and provide an initial test for each of the methods. Thus for simplicity only one of the magnetic field components, the radial or earthward component, will be discussed in detail with respect to the three methods outlined in the previous section.

4.3.1 Phase Skips

Figure 4.1(a) shows the radial (directed toward the Earth) magnetic field component observed by the THEMIS-A fluxgate magnetometer (FGM) [*Auster et al.*, 2008] between 17000-1800 UT. Panel (b) of Figure 4.1 is instantaneous phase of the signal calculated using the Hilbert transform and equation (3.13). Evident in Figure 4.1 is a monochromatic ULF wave with a dominant frequency of approximately 14 mHz which exhibits a coherent and linear trend in phase. Through visual inspection, the wave is first identified between approximately 1720-1725 UT, during this interval the amplitude of the wave begins to increase and phase profile of the signal becomes increasingly linear characteristic of a monochromatic signal.

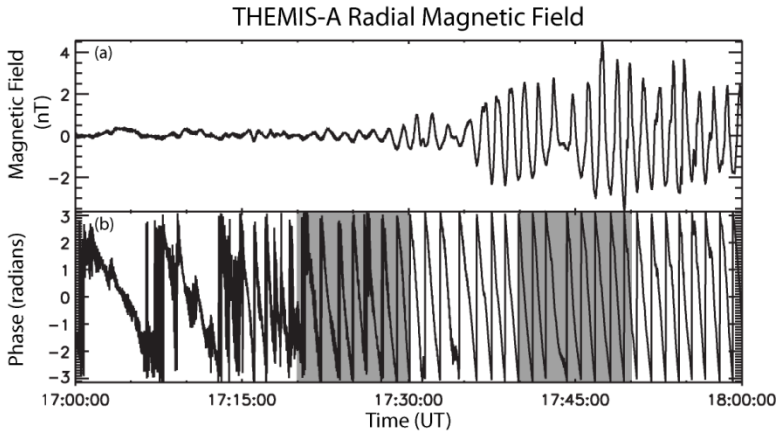

Figure 4.1: (a) The radial magnetic field, nT, from the THEMIS-A FGM during an isolated ULF event on 6th March 2007. (b) The phase profile, in radians, of the ULF wave in (a)

Note that the instantaneous phase of a signal is highly dependent on the amplitude of the signal. During intervals when the amplitude of the signal is large the phase profile is often very linear and phase skips are observed between individual wavepackets. This is clearly observed in the highlighted section of Figure 4.1 between 1740-1750 UT which shows a linear progression of phase and an identifiable phase skip at ~1744-1745. However, when the amplitude of a wave is smaller and background noise fluctuations have a notable affect on the wave amplitude the phase profile while still linear exhibits several phase skips. Thus if a ULF wave gradually rises out the background noise identifying the initial phase skip characterising the onset of ULF wave is difficult. This is depicted in the highlighted section of Figure 4.1 between 1720-1730 UT. Visually the wave appears to start sometime between 1720-1725 UT, however identifying a phase skip associated with the onset of the wave from the raw data is difficult.

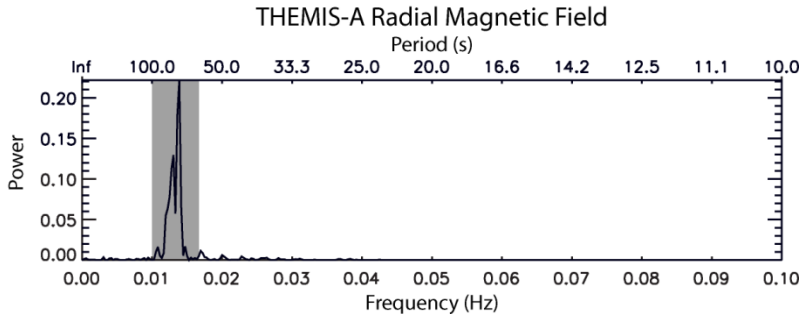

Figure 4.2: The power spectrum from the THEMIS-A radial magnetic field illustrated in Figure 4.1 panel (a).

In order to effectively identify a phase skip associated with the onset of ULF phenomena the time series must be narrow-band filtered. The width of the narrow-band filter required to isolate the ULF signal can be defined using the power spectrum of the signal which characterises the dominant frequency components within the time series. Figure 4.2 illustrates the power spectra of the series plotted in panel (a) of Figure 4.1. A well defined peak centered on 13.9 mHz (72 s) and spanning roughly 10-16.7 mHz (60-100 s, the highlighted section of Figure 4.2) is clearly observed in the power spectra characterising the dominant frequency of the ULF wave and the narrow-band filter which will be used to reduce the background fluctuations at onset. Note that narrow-band filters can be characterised by the full-width-half-maximum of the spectral peak

which characterises a significantly narrower spectral domain then the narrow-band filter of 60-100 s defined above. However there is a trade-off between the filter size and being able to identify phase skips such that as the filter becomes narrower, identifying the phase skips in general becomes more difficult as there is a risk of filtering out the phase skips. Thus we use a filter which is typically larger than the full-width-half-maximum of the spectral peak to reduce the possibility of filtering the phase skip out of the signal.

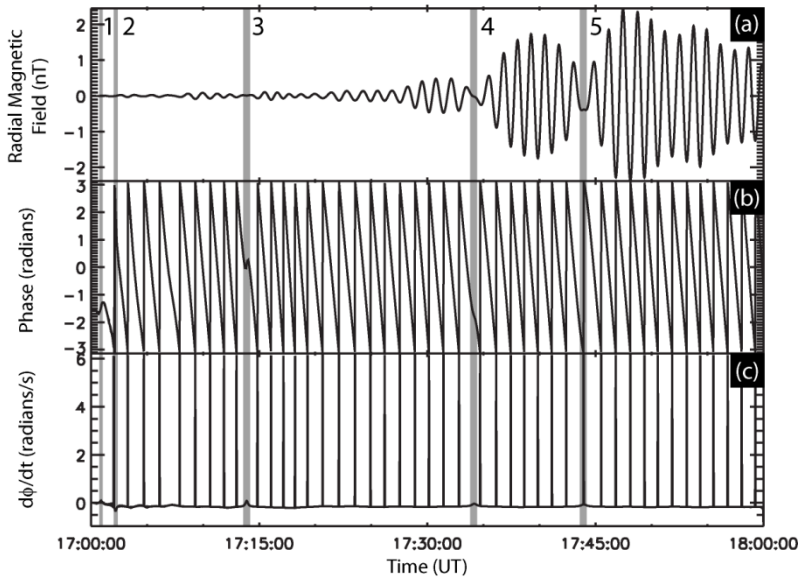

Figure 4.3: (a) The bandpass filtered (60-100 s) THEMIS-A radial magnetic field (nT). (b) The phase profile (radians) of the waveform observed by THEMIS-A, shown in panel (a). (c) The rate of change of the phase profile (radians/s).

Figure 4.3, panel (a), is the 60-100 s bandpass filtered time series from the THEMIS-A spacecraft. The bottom two panels, (b) and (c) respectively, show the phase and rate of change of phase with time ($d\phi/dt$) which characterises the phase skips in the signal. In the bandpass signal there are three phase skips ($|d\phi/dt|>0$) readily identified in panels (b) and (c) of Figure 4.3. The fourth and fifth phase skips, labelled 4 and 5 in Figure 4.3, are clearly associated with the end of one wavepacket and the beginning of another, and thus do not characterise the initial wavepacket or onset of the signal. The initial three phase skips, labelled 1, 2 and 3, occur between 1700:50-1700:56UT, 1702:06 and 1707:17 UT and 1713:40-1714:05 UT respectively (highlighted). Phase skips 1 and 2are

both associated with low amplitude activity on the order of a then of a nano-Tesla. Additionally, phase skips 1 and 2 do not appear to be followed by continuous ULF wave activity (c.f. Figure 4.1 panel (a) and Figure 4.3(a)) thus it is likely that phase skip 3 characterises onset as there are no clearly defined wavepackets before the phase skip and the phase skip is followed by high-amplitude and continuous ULF wave activity. Note however that similar to phase skips 1 and 2 the amplitude of the fluctuations surrounding phase skip 3 are small, on the order of a tenth of a nT, and the phase skip occurs ~7 minutes prior to the initial point in time when the phase first begins to exhibit a linear trend in the signal (first highlighted section of Figure 4.1) and when one would visually identify the onset of the wave at ~1720-1725 UT. This may be a result of the filter used to isolate the ULF signal. If the filter is to narrow then the filter may remove the initial skip associated with the ULF onset. Despite the fact that the filter was defined over the entire width of the spectral peak shown in Figure 4.2 the filter may still be too narrow and removing the initial phase skip associated with the onset of the ULF, though it is difficult to determine how dependent the phase skip structure is on the size or range of narrow-band filter used.

As described above, the amplitude of a signal is important when characterising a wave and examining the phase and phase skips within. Indeed without quantifying the amplitude of the ULF wave and of the background noise fluctuations it is difficult to adequately determine if the initial phase skip is characteristic of the onset of the ULF wave and not a result of pre-existing fluctuations in the background noise levels or a result of the narrow-band filter used. Moreover, when multiple phase skips are associated with low amplitude oscillations it is difficult to adequately determine which of the initial phase skips is most likely to characterises onset of a ULF wave. The ARIMA method utilises both phase and the amplitude of the noise fluctuations to define onset and the DWT method utilises the wavelet power which characterises amplitude and the coherence of the signal with a specific wavelet. Thus the ARIMA and DWT methods may prove to be more consistent with the visual onset time and moreover may identify a more justifiable ULF onset time as more than just phase profile is utilised to determine the ULF onset.

4.3.2 ARIMA Modeling and Phase

Figure 4.4, panel (a), illustrates the entire ULF wave observed by the THEMIS-A spacecraft (1700-1915 UT). The highlighted section shows the part of the time series used to generate the ARIMA model of the time-series. Panel (b) of Figure 4.4 is an expanded view of the highlighted section of panel (a), the black curve is the observed ULF wave from THEMIS-A. The red curve, in panel (c) of Figure 4.4 is the ARIMA modeled ULF wave determined from the time series shown in panel (b). Note the modeled wave is extraordinarily similar to the wave observed by the THEMIS-A FGM. Panel (d) of Figure 4.4 is a plot of the residuals, the difference between the ARIMA modeled time-series and the actual time-series. The residuals are normally distributed about a mean of approximately zero (-0.000245 nT) with a standard deviation (σ_w) of 0.058 nT; this is typical and often required for the residuals of a ARIMA modeled series.

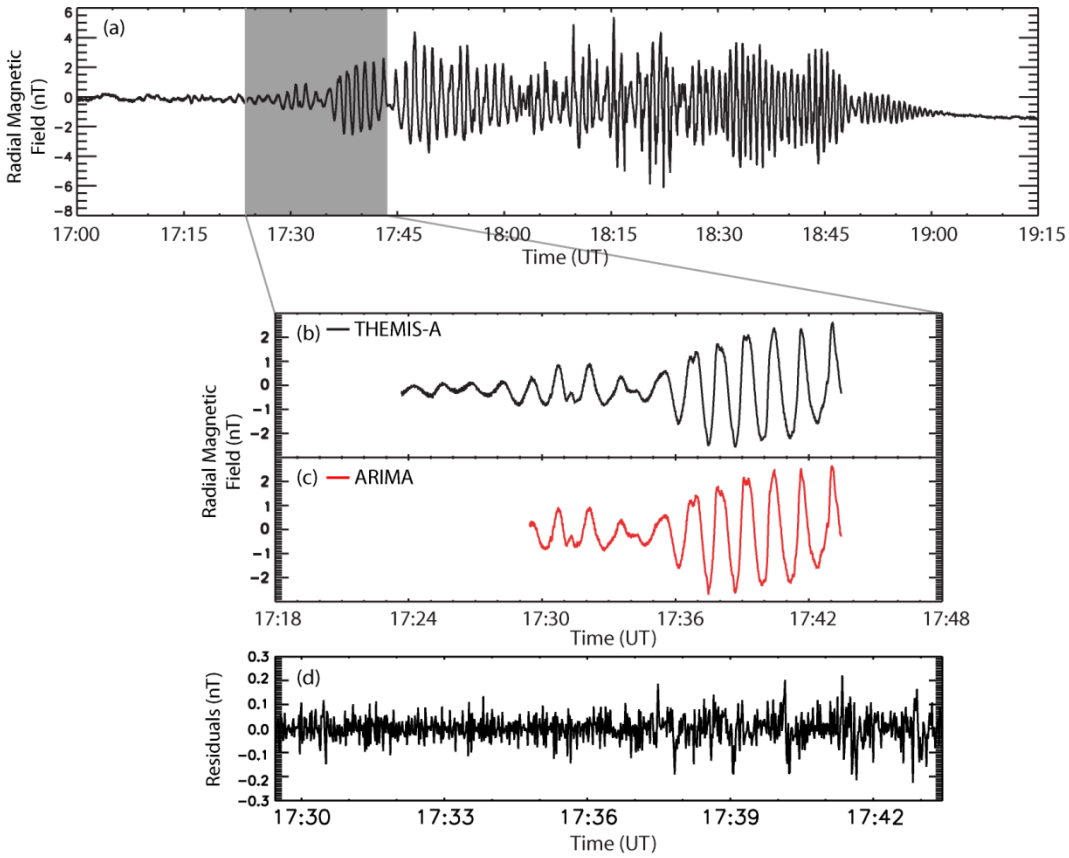

Figure 4.4: THEMIS-A radial magnetic field (nT). (b) Expanded view of the highlighted region in (a), the black trace is the THEMIS-A radial magnetic field. (c) The ARIMA modeled time series of the THEMIS time series shown in (b). (c) The ARIMA modeled residuals.

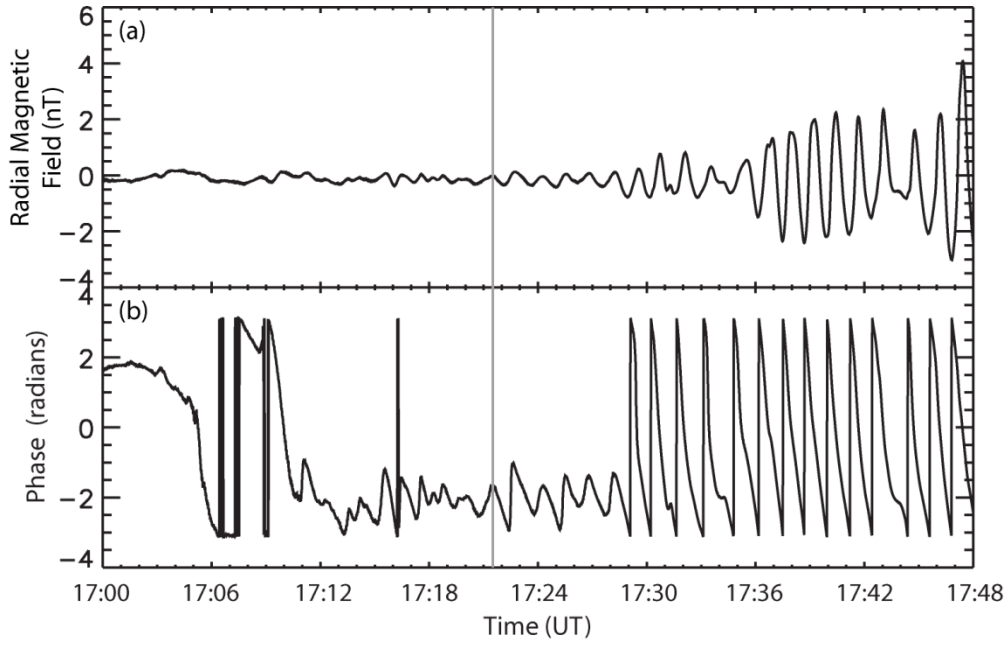

Figure 4.5: Illustrates the ULF onset time defined by the ARIMA modeling and phase technique at 1721:31 UT, defined by the vertical line. (a) The lowpass filtered radial magnetic field, filtered using nine point (9 s) running mean of the signal. (b) The phase of the signal in panel (a).

As described in Section 4.2.2, the ULF onset is defined as the initial point when the wave amplitude is greater than $4\sigma_w$ and has a phase profile consistent with that of a sinusoid. This is depicted by the vertical line in Figure 4.5, at 1721:31 UT. The top panel of Figure 4.5 shows the radial magnetic field and the bottom panel is the phase profile of the radial magnetic field defined by (3.13). The magnetic field has been lowpass filtered using a nine point (9 s) running mean to reduce background fluctuations so that the linear phase is clearly depicted, in contrast to Figure 4.1 (b). The onset defined by the ARIMA method at 1721:31 UT is approximately six minutes after the onset identified by the initial phase skip in the signal (1713:40-1714:05 UT) and consistent with the onset window determined by a visual inspections of the signal (~1720-1725 UT). It is important to note that the lowpass filtered signal shown Figure 4.5 does in fact exhibit a phase skip at the onset time identified by the ARIMA method at in 1721:31 UT. Though $d\phi/dt$ is not plotted the phase skip is readily identifiable in Figure 4.5 panel (b) as the phase changes from positive to negative slope across ARIMA onset time at 1721:31 UT. This clearly shows how dependent the phase skip methodology is on the width of the narrow-band filter used to isolate signal as discussed in the previous section. Indeed the ARIMA method which uses both the phase of the signal and an estimate of the amplitude of the

noise fluctuations in a time series to define the onset of a ULF wave provides a more reliable and justifiable onset then one which uses a single aspect to characterise the signal and the ULF wave onset.

4.3.3 The DWT

Figure 4.6 is the DWT power spectrum of the THEMIS-A radial magnetic field and illustrates the implementation of the DWT method. The power in each wavelet band (defined on the y-axis) is normalised to one and power below the wavelet threshold (see Section 4.2.3) is plotted in black. From Figure 4.6 it is clear that the first ULF band whose power continuously rises above the threshold is the 48-192 s period band, characterising onset at be 1721:12 UT (±32 s).The uncertainty in the onset time is inherent to any discrete wavelet transform since each wavelet band (*j*) has a characteristic temporal width (w_j) defined as,

$$w_j = 2^{\left(\ln(N)/\ln(2)\right)-j+1}, \tag{4.1}$$

where N is the number of points in the time series. Note that the length of a series N must be a power of 2 when utilising the DWT. In any given wavelet band the uncertainty in the wavelet onset time is defined here to be half the temporal width of the wavelet coefficients in that band. In this case the wavelet band defining onset (*j*=6) has a 64 s width (w_j), thus the wavelet onset time is specified as the center of the coefficient to initially rise above the defined threshold with an uncertainty plus or minus 32 s (w_j/2). The DWT onset time is consistent with the onset characterised by the ARIMA model and phase (1721:31 UT). Additionally the ULF wave band identified by the DWT (48-192 s) is consistent with the peak observed in the power spectra (~70 s) shown in Figure 4.2.

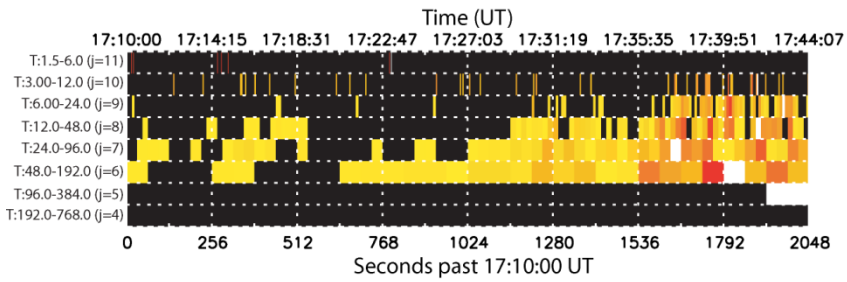

Figure 4.6: The DWT power spectrum from the THEMIS-A radial component magnetic field. The onset is defined by the 48-192 s wavelet band (j=4) at 1721:12 UT (±32 s).

4.4 Ground-based Case Study: Magnetic Substorm on 1st November 2006

The previous section utilised THEMIS-A satellite observations of a continuous ULF wave to examine the ability of three methods to characterise the onset of a wavepacket in a relatively stationary time series. In this section the techniques described in Section 4.2 will be used to identify the onset of ULF waves during a magnetic substorm observed by the RABB magnetometer on the ground (see Figure 3.2 for location) on the 1st November 2006, a period characterised by a more complex time series then that discussed in Section 4.3. Note that the event on 1st November 2006 has been previously studied by Milling et al. [2008] in the context of the DWT. These authors used a method similar to that described here in order to define the onset of ULF waves. However, the threshold defined in Milling et al. [2008] differs from that utilised here and in subsequent Chapters. The threshold utilised in Milling et al. [2008] is dependent on the time series window which characterises the ULF onset, where as wavelet threshold here is defined by a quiet time magnetometer trace which is independent of the time series window used to define the ULF onset.

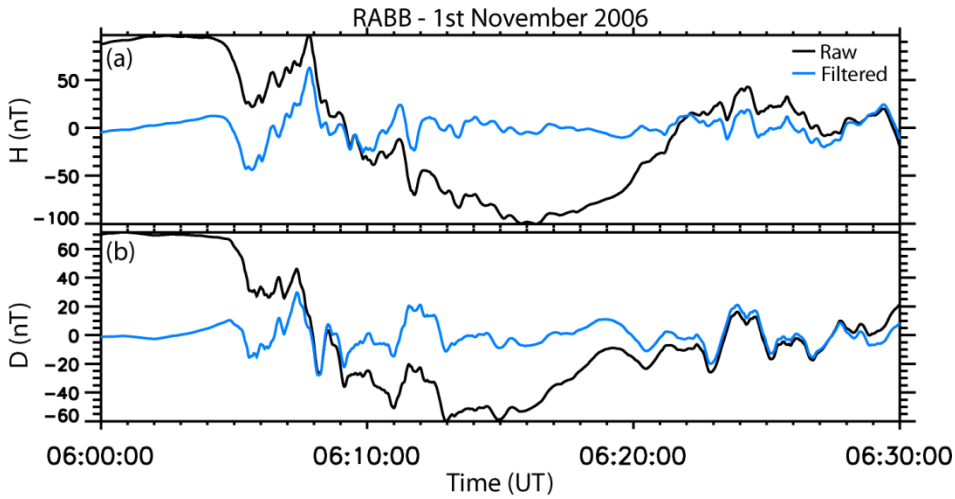

Figure 4.7: (a)The H and (b) the D magnetic field from the RABB magnetometer during a magnetic substorm on 1st November 2006.,The black trace is the raw H and D field and the blue trace is the highpass filtered (0-500s) series.

As mentioned in Chapter 1, substorms are manifested on the ground as large-scale deflections of the Earth's magnetic field and the onset of impulsive ULF waves referred

to as Pi1 and Pi2 waves. In general, Pi2 waves are believed to be Alfvén waves [*Lester et al.*, 1983; *Olson*, 1999]. The wave mode associated with Pi1 pulsations remains less well-understood, though recent work by Lessard et al. [2006] and Rae et al. [2009b] has suggested that Pi1 waves observed in the ionosphere are in fact also Alfvénic in nature. In this section both the H and D magnetic field components will be considered in order to identify the onset of ULF waves during the expansion phase. This inherently makes identifying the onset of ULF waves during a substorm more difficult as both the H- and D-components of the signal must be used.

Figure 4.7 shows plots of the raw H- and D-component magnetic field from the RABB magnetometer, in panels (a) and (b) respectively. The highpass filtered time series is over plotted in blue to remove the SCW bay component of the magnetic field (the background perturbation) and isolate the ULF waves associated with the expansion phase onset. The H- and D-components from both the raw and highpass filtered series have a mean and standard deviation which vary with time, characteristic of a non-stationary time series. Typically, generating an accurate ARIMA model of a signal requires it to be a near-stationary time series, such as the THEMIS-A data discussed in the previous section. Substorms, as illustrated in Figure 4.7 are typically not stationary signals. Thus finding an appropriate ARIMA model for ground-based magnetic substorm perturbations is difficult in practice. Though the ARIMA model is an excellent method to define the onset of ULF waves during a stationary process it will not be considered in the context of substorms as the stability and robustness required for using ARIMA to study ULF waves in multiple field components from several magnetometers during the substorm expansion phase is not typically present.

4.4.1 Phase Skips

In Section 4.3.1, and further in Section 4.3.2, it was shown that analysing phase skips to identify the onset of a ULF wave was difficult since phase skips are characterised by a single aspect of the wave, the phase. Moreover the phase skips within a signal were highly dependent on both the amplitude of the signal, which is not quantified in the phase skip methodology, (c.f. Figure 4.1) and the narrow-band filter used to isolate the waveform from the background fluctuations (c.f. Figure 4.5).However, phase skips are intrinsic to impulsive signals [e.g., *Mier-Jedrzejowicz and Hughes*, 1980] and thus phase

skips may be more suitable for characterising the onset of ULF waves during substorms. In this section a similar phase skip methodology for identifying the onset of ULF waves will be explored as in the previous section. However, because two magnetic field components need to be considered the bandpass filter will be defined by the coherence spectrum of H and D. This ensures that both the H- and D-components observe power in the ULF frequency band and further that a similar waveform is observed in both transverse components of the measured magnetic field. Figure 4.8 shows (a) the H and (b) the D power spectra of the highpass (0-500 s) filtered signal shown in Figure 4.7 (blue line). The bottom panel, (c), of Figure 4.8 shows the coherence between the H and D lowpass filtered time series. Figure 4.8 clearly illustrates that ULF wave power is concentrated at lower frequencies (long periods) however a broad peak in coherence is also observed at higher frequencies between periods ~20-50 s, shown by the highlighted section of Figure 4.8.

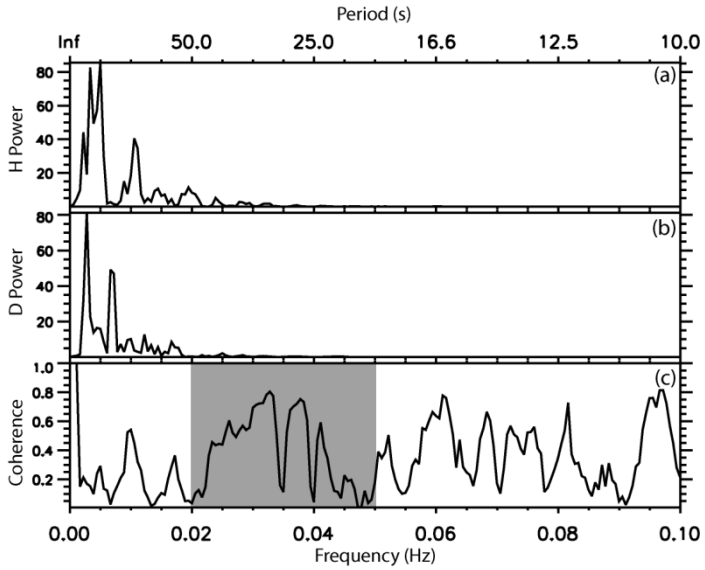

Figure 4.8: (a)H and (b) D power spectrum of highpass (0-500 s) filtered signal shown in Figure 4.7 (blue). (c) The H-D coherence spectrum, panel (c).

Figure 4.9, panel (a), shows the narrow-band filtered H (left) and D (right) magnetic field between 20-50 s periods. The phase, and rate of change of phase, are shown in panels (b) and (c) respectively. The phase skips in each component are identified by the grey highlighted regions and are summarised in Table 4.1. Note that there are three phase

skips in H and four in D. If the ULF wave characterising onset was polarised and hence observed in both the H- and D-component then one might expect an equal number of skips in each component. Since there are multiple phase skips in each component correctly identifying the onset of a ULF wave packet is complicated and potentially subjective. This makes determining which phase skip characterises the onset of the ULF waves somewhat difficult.

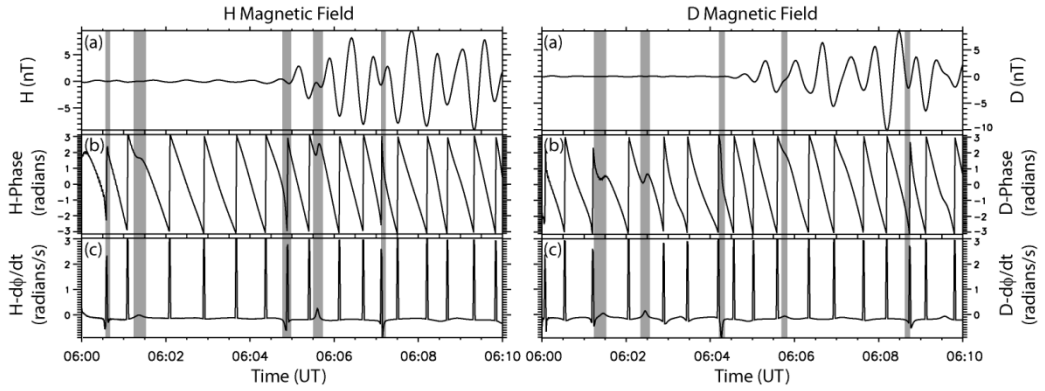

Figure 4.9: H and D (left and right) (a) bandpass filtered (20-50 s) series during the 1st November 2006 substorm. (b) Phase profiles of the bandpassed signal and (c) the temporal rate of change of phase. In both H and D the phase skips are highlighted by the grey boxes.

Table 4.1: H and D phase skips from the 1st November 2006 substorm

Skip	**H**		**D**	
	Start (UT)	**Finish (UT)**	**Start (UT)**	**Finish (UT)**
1	0600:33	0600:38		
2	0601:15	0601:31	0601:15	0601:31
3			0602:21	0602:33
4	0604:47	0604:58	0604:13	0604:20
5	0605:31	0605:43	0605:42	0605:49
6	0607:06	0607:11		
7			0608:43	060849

Similar to Section 4.3.1, the first two phase skips identified in H and D are associated low amplitude fluctuations of the magnetic field. However phase skips 4 (c.f. Table 4.1) in H and D (respectively), are associated with larger amplitude ULF wave activity. Additionally, these phase skips are temporally conjugate, to within a half wave period,

separated by approximately 27 s. Similarly, phase skips 5 in H and D are temporally conjugate. These skips are additionally visually associated with the onset of a second ULF wave packet in both the H and D time series. Phase skip 6, apparent only in the H-component, and phase skip 7, observed in the D-component, are both isolated phase skips and appear to be separating wavepackets similar to phase skip 5. As such phase skips 5, 6, and 7 do not characterise the onset of a ULF wave. Thus it seems the most likely phase skips characterising the initial onset of ULF activity is defined by phase skip 3 in H and D, corresponding to an onset window of 0604:13-0604:58 UT, as these skips are associated with a larger amplitude wave than phase skips 1, 2 and 3, while phase skips 5, 6, and 7 appear to be separating distinct wavepackets. Clearly, when multiple phase skips are observed in both the H- and D-components, correctly identifying onset becomes difficult and somewhat subjective. Further, without quantifying the amplitude of the wave or noise fluctuations it is difficult to determine whether a phase skip is actually associated with ULF wave activity or is a skip inherent to background noise fluctuations, for example the first phase skip identified at 0601:15-0601:31 UT. This was also noted in Section 4.3.1. With multiple skips it seems unlikely that phase skips alone will be a reliable and consistent method with which to identify and characterise the onset of ULF waves during substorm expansion phase onset.

4.4.2 The DWT

In Section 4.3.3, the DWT was shown to provide an excellent method with which to define the onset of a ULF wave. The same approach will be used here in order to identify the onset of ULF waves during the substorm expansion phase onset. However, as above, rather than considering a single component of the magnetic field oscillations the total transverse oscillation in both the H- and D-components will now be taken into account.

With the DWT a two component time series is readily studied by considering the amplitude of the vector sum of both the H- and D-component wavelet coefficients. This can hence provide an estimate of the ULF wave power in the transverse plane rather than in a single field component. The threshold is defined in the same way as in Section 4.3.2, but this time considering both H and D and the amplitude of the vector sum of the coefficients. Figure 4.10 panel (a) is the H-D wavelet power spectra for 1st November 2006 (c.f. Figure 4.6). Power below the wavelet threshold in each wavelet band is set to

zero and plotted in black. Similar to Section 4.3.3, the ULF onset is identified by seeking the first wavelet coefficient to rise and remain above the wavelet power threshold, detailed during a quiet interval. This is seen to correspond to the 12-48 s wavelet band with the ULF onset occurring at 0603:44 UT (±8 s). Panels (b)-(d) of Figure 4.10 show the inverse wavelet transform of the H- and D-components of the magnetic field in the 12-48 s wavelet band and the 12-48 s H-D wavelet power shown in panel (a), respectively. These panels illustrate the amplitude of the H- and D-components and total wavelet power of the ULF waveband identified by the DWT method. The onset window is highlighted in grey and the central time by the vertical red line. Note that the wavelet onset time is closely coincident with the onset time defined by the phase skips in the signal, at 0604:13-0604:58 UT. Further note that wavelet band identifying the ULF onset (12-48 s) is similar to the narrow-band filter used in Section 4.4.1 (20-50 s period). The DWT method for identifying the onset of ULF waves during the substorm expansion phase is not only substantially simpler than identifying the onset using phase skips within the signal but may also be more reliable as only a single onset time is identified where as a total of seven phase skips were observed in the H- and D-component time series in the previous section.

4.5 Discussion and Conclusions

While phase skips have been shown previously to be a good method for characterising the onset of ULF waves and differentiating between different wavepackets during quasi-monochromatic events [*Chi and Russell*, 1998], identifying the onset of ULF phenomena via phase skips can be difficult and subjective as illustrated in Sections 4.3.1 and 4.4.1. In order to characterise the phase profile of a ULF wave, the signal has to be narrow-band filtered to isolate the frequency of interest from the rest of the signal and to reduce the influence of background fluctuations. However, this potentially removes phase skips from the signal, as shown in Section 4.3. Moreover during substorm expansion phase onset multiple ULF wavepackets are often observed with differing frequencies and amplitudes. In order to adequately characterise the onset of the waves observed during a magnetic substorm the entire ULF spectrum must be considered. In addition, when characterising the ULF onset during a magnetic substorm both the H- and D-components were shown to exhibit multiple phase skips. This is likely to be a typical characteristic of

ULF waves observed during substorm expansion phase onset. Objectively defining ULF onset when multiple phase skips are present is difficult as one must determine which skips are most likely associated with the onset of a ULF wave. As discussed in Waters [2000], phase skips are often observed in only a single component of the magnetic field and when observed in both magnetic field components they are often temporally disparate, without a clear pattern relating the temporal delays between skips. While phase skips have in the past been used to characterise the onset of ULF waves, phase skips alone seem to be unlikely to offer a robust method with which to reliably and objectively define the onset of ULF waves during the substorm expansion phase.

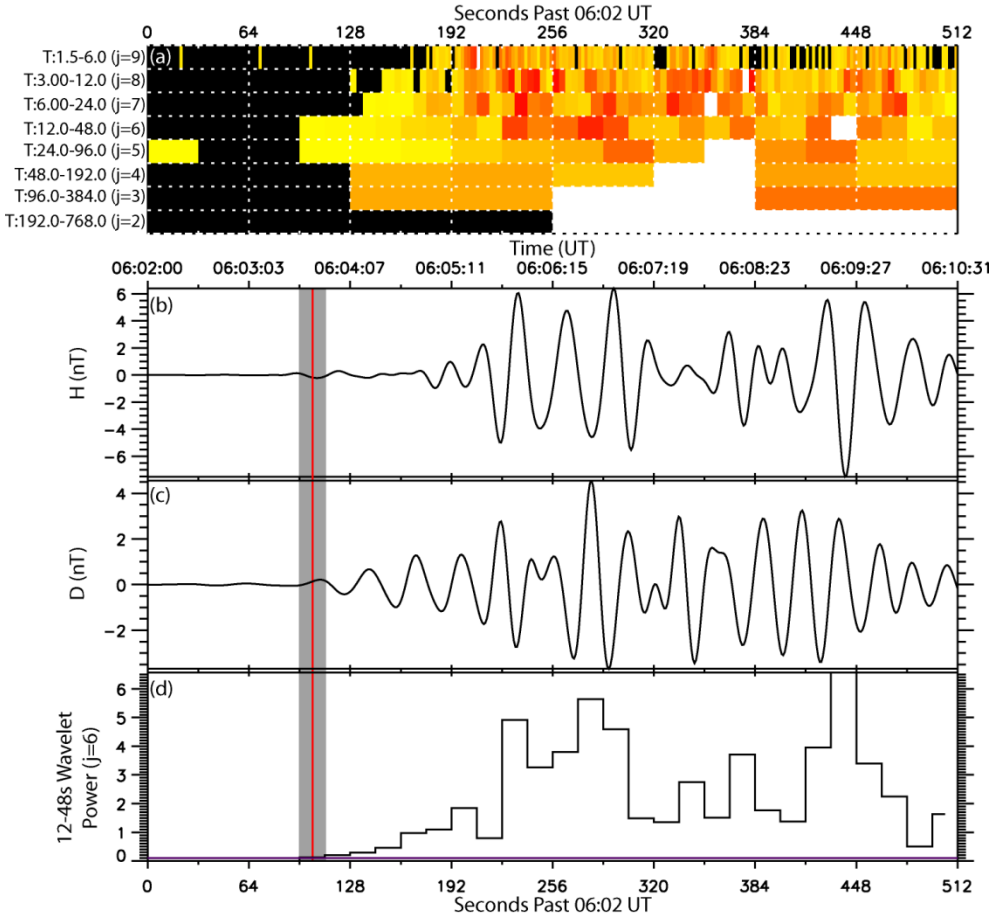

Figure 4.10: The DWT analysis of the 1st November 2006 substorm. Panel (a) shows the wavelet power spectrum from the RABB magnetometer. Panels (b) and (c) are the inverse wavelet transform of the H and D magnetic field components in the 12-48 s wavelet band which defines ULF onset. Panel (d) shows the wavelet power in the 12-48 s wavelet band. The vertical red line depicts the ULF onset at 0603:44 UT and the highlighted region the uncertainty in the ULF onset time (±8 s for the j=6 wavelet band)

For a stationary time series (i.e. the mean and standard deviation are relatively constant), the ARIMA model and phase characteristics provide an excellent means with which to identify onset when considering a relatively monochromatic and stationary waveform. This is clearly demonstrated in Section 4.3.2 and Figure 4.4. Moreover the onset time identified using the ARIMA model and phase for the continuous pulsation in Section 4.3 was consistent with that identified using the DWT methodology. However, when considering a non-stationary series, for instance those observed during magnetic substorms, an ARIMA model is unable to adequately characterise every aspect of the time series, such as the slowly varying perturbation associated with the SCW as well as the larger amplitude Pi2 oscillations associated with the formation of the SCW. In short, while the ARIMA methodology is excellent for characterising a stationary time series, the technique is likely somewhat inadequate in the context of the expansion phase and defining the ULF onset of magnetic substorms.

Unlike ARIMA modeling, wavelets are capable of characterising both stationary and non-stationary time series. Unlike the phase skip methodology a DWT is able to probe the entire ULF spectrum and not simply a narrow-band of ULF power. Moreover the wavelet technique described herein can objectively define an identifiable ULF onset time during substorm expansion phase onset, so long as an appropriate threshold is chosen, in contrast to both the ARIMA and phase skip methodologies. In Section 4.3 the onset time of the continuous pulsation observed by THEMIS-A determined by the DWT method was consistent with ARIMA onset time. Similarly during the 1st November 2006 substorm (Section 4.4) the DWT and phase skip methods defined ULF onset times which were closely conjugate in time. This suggests that the DWT algorithm is a reliable and robust method for characterising the onset of ULF waves during both continuous pulsation events and during substorm expansion phase onset. Recent work by Milling et al. [2008] has shown that the DWT is a powerful and novel tool for timing and locating substorm onset utilising an array of ground-based magnetometers. In the subsequent Chapter, the DWT method described in Section 4.2.3 will be further developed and validated by comparing the ULF onset time and location to those from optical observations of the expansion of the aurora as well as the features of the historical optical definition of the time series of events during expansion phase onset [*Akasofu*, 1964].

Chapter 5 Wavelet-based ULF Wave Diagnosis of Substorm Expansion Phase Onset[1]

Summary

Using a discrete wavelet transform with a Meyer wavelet basis, we present a new quantitative algorithm for determining the onset time of Pi1 and Pi2 Ultra Low Frequency (ULF) waves in the nightside ionosphere with ~20-40 s resolution at substorm expansion phase onset. We validate the algorithm by comparing both the ULF wave onset time and location to the optical onset determined by the IMAGE-FUV instrument. In each of the five substorm onsets analysed the ULF onset is observed prior to the global optical onset observed by IMAGE at a station closely conjugate to the optical onset. The observed ULF onset times expand both latitudinally and longitudinally away from an epicentre of ULF wave power in the ionosphere. We further discuss the utility of the algorithm for diagnosing pseudo-breakups, and the relationship of the ULF onset epicentre to the meridians of elements of the substorm current wedge. The importance of the technique for establishing the causal sequence of events at substorm onset, especially in support of the multi-satellite THEMIS mission, is also described.

5.1 Introduction

Since the initial detailed characterisation of the growth, expansion and recovery phases of substorms [*Akasofu*, 1964; *McPherron*, 1970], significant work has been dedicated to determining the mechanism (or mechanisms) responsible for the onset and subsequent evolution of substorms in the magnetosphere. Two models are currently favoured to explain the observed phenomena associated with the expansion onset phase of a geomagnetic substorm: the Near Earth Neutral Line (NENL) [*Baker et al.*, 1996; *Russell and McPherron*, 1973] and Current Disruption (CD) [e.g., *Lui*, 1996] models. In the NENL model, magnetic reconnection in the tail is responsible for the initiation of the expansion phase, while in the CD model, a plasma instability in the near-Earth plasmasheet initiates the substorm expansion phase.

[1] Based on Murphy, K. R. et al. (2009), Wavelet-based ULF wave diagnosis of substorm expansion phase onset, *J. Geophys. Res.*, 114, A00C16, doi:10.1029/2008JA013548.

In the NENL model, reconnection in the magnetotail at distances ~20-25 Re [e.g., *Baumjohann et al.*, 1989] drives Earthward flows in the form of bursty bulk flows (BBFs) [e.g., *Angelopoulos et al.*, 1992]. These BBFs brake as they approach dipolar field lines closer to the Earth, disrupting the cross-tail current and diverting it into the ionosphere to form the Substorm Current Wedge (SCW) [e.g., *Shiokawa et al.*, 1997]. In the CD model, plasma instabilities, such as ballooning modes [*Roux et al.*, 1991] [e.g., Roux et al., 1991], lower hybrid turbulence [e.g., *Huba et al.*, 1977; *Lui*, 1996], or cross-field current instabilities [e.g., *Lui et al.*, 1995] lead to diversion of the cross-tail current into the ionosphere forming the SCW. In this model, rarefaction waves propagate outwards and trigger reconnection at the NENL later in the expansion phase following the onset at the inner edge of the plasmasheet [e.g., *Angelopoulos*, 2008]. To date, the lack of sufficiently large scale and sufficiently high spatial and temporal resolution conjugate in-situ and ground-based magnetic and auroral observations during the expansion phase of substorms has hindered efforts to resolve, both spatially and temporally, the sequence of events to unequivocally determine whether substorms onset occurs “inside-to-out” (e.g., CD) or “outside-to-in” (e.g., NENL).

Vital to characterising the sequence of events observed during the evolution of the substorm is an accurate determination of the spatial and temporal onset of the substorm expansion phase. Traditionally the structure and dynamics of auroral arcs preceding the formation of the substorm current wedge (SCW) have been used to determine the onset of the substorm expansion phase. Akasofu [1964] characterised the onset of the expansion phase as the brightening of a quiescent arc, “usually the most equatorward arc”, followed by the rapid poleward expansion of the auroral arc. During periods of clear skies, ground-based optical instruments provide a characterisation of the energetic particle precipitation during the expansion phase onset of substorms. However, we will show in this Chapter that we can achieve a better understanding of the evolution of substorms by including ground-based observations of magnetic fluctuations, especially since disturbances with no optical counterpart (i.e. missing images or obscured by thick clouds) can then also be characterised.

Substorms manifest themselves in ground-based magnetometers as large amplitude perturbations of the background field [*Kisabeth and Rostoker*, 1977] as the magnetotail

dipolarizes and the SCW wedge forms in the magnetosphere. Prior to the full formation of the SCW, impulsive Ultra Low Frequency (ULF) waves denoted Pi1s and Pi2s with periods of 1-40s and 40-150s, respectively, are observed [*Jacobs et al.*, 1964]. Pi2s observed at substorm onset are believed to be generated by the initial disturbance of the magnetospheric plasma sheet during the expansion phase onset, and the propagation to the ionosphere and subsequent perturbations establish the field-aligned current (FAC) system in the SCW [*Olson*, 1999]. Though evidence suggests that these waves are intimately connected with the onset of the substorm expansion phase, the onset of Pi2 wavepackets can generally be timed with a resolution of approximately the wave period (~1-2 minutes). Pi2 waves are also commonly observed across many hours of local time, and hence their meso-scale occurrence cannot be used to identify any localised ionospheric region associated with substorm initiation. Note however that the polarisation of Pi2s can be used to identify the meridians of the elements of the SCW [e.g., *Lester et al.*, 1983]. Pi1s on the other hand have significantly shorter periods allowing for more accurate timing of substorm expansion phase onset.

Initial studies of Pi1s observed at substorm onset concentrated on broadband ULF waves with periods of 1-10s, referred to as Pi1B waves [e.g., *Bösinger et al.*, 1981; *Lessard et al.*, 2006]. Posch et al. [2007] found that the onset of Pi1Bs are coincident in both time and space to the optical onset determined by the IMAGE-FUV. These authors concluded that a very dense array of searchcoil magnetometers may provide improved information and resolution of the ionospheric onset location. Milling et al. [*Milling et al.*, 2008] have recently shown using discrete wavelet transform (DWT) techniques that long period Pi1s can be used to define a ULF onset time to within a temporal resolution of ~20s. These authors have shown that long-period Pi1 waves, which are more readily studied with the current deployment of fluxgate magnetometers in the North American auroral zone than their shorter period Pi1B counterparts, also have a localised ionospheric epicentre where the onset disturbance begins, which subsequently expands over continent scales.

In this Chapter further application of the DWT algorithm discussed in Chapter 4 is presented to examine the ionospheric onset of magnetic substorms. The DWT algorithm and results are validated by comparing optical onsets determined by the IMAGE-FUV

instrument, with a 2 minute cadence, on-board the IMAGE satellite, to the Pi1/2 ULF onset time and ionospheric location determined using the DWT algorithm. We present here five events identified in the Frey substorm database [*Frey et al.*, 2004; *Frey and Mende*, 2006] and in each of the substorm events we find a coherent expansion of ULF waves away from an epicentre of ULF power, consistent with the Pi1/2 expansion observed by Milling et al. [2008]. The Pi1/2 ULF DWT algorithm hence represents a powerful new tool for characterising the onset and evolution of substorms especially when combined with in-situ satellite data, for example THEMIS, and contributes to the resolution of the so-called "two-minute problem" [e.g., *Angelopoulos*, 2008; *Petrukovich and Yahnin*, 2006]. The ability to accurately determine timing, and hence the causal sequence of events in relation to the proposed CD and NENL hypotheses for substorm expansion phase onset, is key to ultimately solving the substorm problem.

5.2 AWESOME: Automated Wavelet Estimation of Substorm Onset and Magnetic Events

Wavelets provide a novel tool for studying localised characteristics of a non-stationary series in both the frequency and time domains. Specifically the discrete wavelet transform (DWT) utilises a complete wavelet basis (for example; the Meyer [*Meyer*, 1989] or Daubechies wavelets [*Daubechies*, 1988]) to decompose a signal into wavelet coefficients denoted by $\alpha_{j,k}$, which are localised in time (k) and band limited in frequency or period (j). With the use of the DWT and a specified wavelet basis, the dispersive and impulsive characteristics of wave phenomena are more accurately represented than with the traditional Fourier transform.

The DWT's ability to characterise both the frequency and temporal content of waves makes it ideal for studying Pi1 and Pi2 ULF waves during the onset of magnetic substorms. Nose et al. [1998] showed that the Meyer wavelet can be used for studying long-period and impulsive Pi2 ULF waves associated with substorm onset. These authors successfully developed an automated algorithm, utilising a wavelet power threshold, for now-casting magnetic substorms from real-time mid-latitude ground-based magnetometer data. For reference, Figure 5.1 shows the characteristic Meyer wavelet from the three unitary wavelet coefficients, $\alpha_{6,7}$, $\alpha_{5,7}$ and $\alpha_{4,7}$ (Figure 5.1 a-c, respectively). Table 5.1 shows the period band (j), ULF band, temporal width (k) and the

associated timing uncertainty for a wavelet of specific *j*. The period bands shown in this table have values associated with the impulsive Pi1 and Pi2 ULF wave bands.

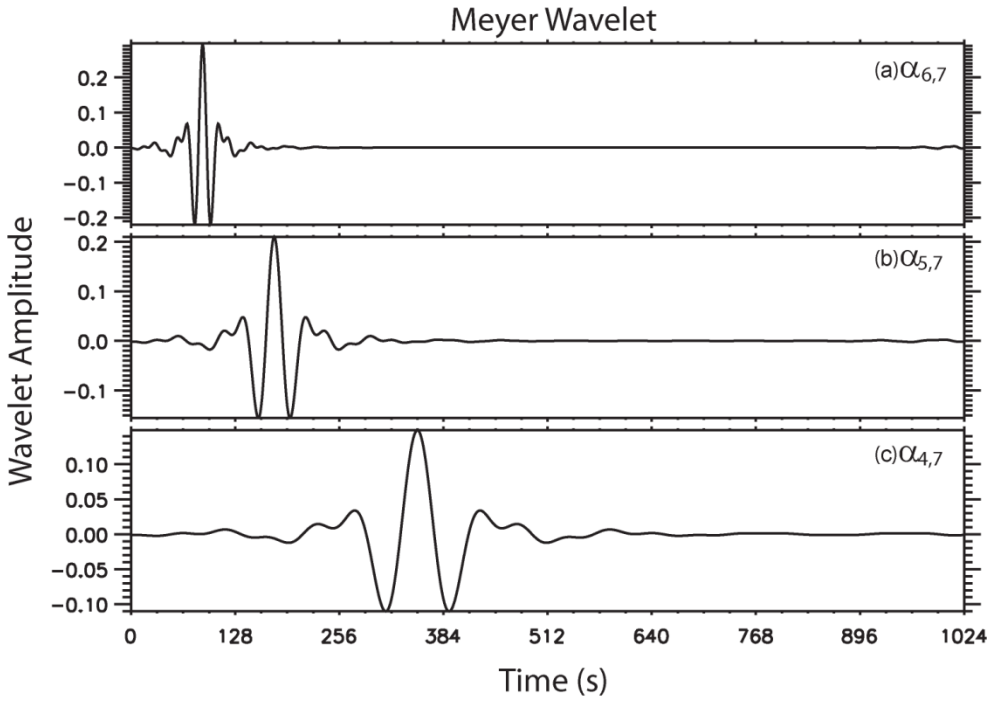

Figure 5.1: Select Meyer wavelets, (*j, k*), representative of the Pi1 and Pi2 ULF waves observed during the expansion phase onset; (a) (6, 7)-Pi1/2, (b) (5, 7)-Pi1/2, (c) (4, 7)-Pi2.

The Automated Wavelet Estimation of Substorm Onset and Magnetic Events (AWESOME) technique presented here utilises the Meyer wavelet to determine the onset time and characteristics of ULF waves as a function of *j* observed by ground-based magnetometers. The AWESOME algorithm is applied to magnetometer data provided by the CARISMA [*Mann et al.*, 2008], THEMIS [*Russell et al.*, 2008], CANMOS, GIMA and MCMAC magnetometer arrays (see Figure 3.2) to determine the initiation time of ULF waves in the Pi1 and Pi2 bands in the North American sector following substorm expansion phase onset. Using the AWESOME algorithm and the extensive spatial coverage provided by these five magnetometer arrays provides a means to determine the spatial dependence of the onset time of Pi1 and Pi2 ULF waves at the onset of a magnetospheric substorm on a continental scale. The resulting expansion of these ULF wave signals in the ionosphere also indicates the capabilities of the AWESOME

technique to identify an ionospheric epicentre of ULF wave activity using DWT methods [c.f., *Milling et al.*, 2008].

It is sometimes difficult to estimate the onset of substorm-related ULF wave activity since the time-series are noisy and contain fluctuations due to pre-existing ionospheric currents. The AWESOME algorithm implements an interactive adaptive threshold to determine the time at which the signal at each magnetometer station in each *j* band develops power above the pre-existing noise. For each magnetometer station a period of low-amplitude ULF wave power before the substorm is selected. In all of the events we select the quietest interval preceding the substorm during the UT day, usually an interval greater than five hours, and calculate a noise threshold for each band based upon the properties of the waves during this time. While this is the case for each of the events presented herein, a quiet time preceding substorm onset cannot always be identified. In such cases other times, either earlier or later, could be selected to define magnetic quiet at each stations and hence the appropriate thresholds. The calculation of a statistical noise threshold based upon prior "quiet-time" magnetometer data at each station allows the AWESOME algorithm to more objectively and quantitatively determine the onset time of substorm related ULF waves. The Meyer DWT power spectrum is calculated using the geomagnetic north-south and east-west magnetic field components (H and D, respectively), and the transverse wavelet power coefficients $\alpha_{j,k}$ are determined from the square root of the sum of squares of $\alpha^H_{j,k}$ and $\alpha^D_{j,k}$, i.e. equation (5.1).

$$\alpha = \sqrt{(\alpha^D)^2 + (\alpha^H)^2}. \tag{5.1}$$

The threshold power value for each wavelet frequency band, *j*, is defined as the mean plus two standard deviations of the quiet time wavelet power coefficients in that band. In the DWT applied here we use a window of 512 s of data with 1 s cadence. Since the DWT Meyer wavelet, like all mother wavelets, has length inversely proportional to *j*, we obtain more power estimates for large *j* within the 512 s window. For example for the *j* = 4, the wavelet is 64 s in length, generating a set of eight wavelet power coefficients to define the mean and standard deviation (σ_α) of the *j* = 4 wavelet band during the 512 s window; for *j* = 9, the wavelets are 2 s long, hence there are 256 estimates of wavelet power in the 512 s window with which to define the mean and standard deviation of the

power for the *j* = 9 wavelet band. This 2 σ_α threshold provides a ~95% confidence level that wavelet power coefficients above these thresholds represent a statistically significant signal and are not background noise. Note that in theory different threshold definitions can be used, this can be important for analysing multiple or compound substorm intervals (i.e., non-isolated activations which evolve as a series of pre-cursors or pseudo-breakups followed by a main onset, often with subsequent intensifications) where power fluctuations do not return to pre-substorm levels between multiple onsets. However, for isolated substorms we have determined that in practice, by characterising the quiet time amplitude distribution of wavelet coefficients and comparing the relative strengths of ULF power during quiet time intervals, isolated substorms and compound substorm events, two standard deviations represent a good threshold. The time of onset of substorm-related ULF activity is defined by using the first *j* band to exhibit a continuous time-series of transverse wavelet coefficients whose power exceeds the threshold value. The onset time is then defined to be at the center of the first wavelet coefficient which exceeds the threshold, the uncertainty being defined as plus or minus half the temporal width of each coefficient for the specific onset band (c.f., Table 5.1).

Table 5.1: The Meyer wavelet

j	Period (s)		Temporal	Error	ULF
	Lower	Upper	Width (s)	Estimate (s)	Band
9	1.5	6	2	±1	Pi1
8	3	12	4	±2	Pi1
7	6	24	8	±4	Pi1
6	12	48	16	±8	Pi1/2
5	24	96	32	±16	Pi1/2
4	48	192	64	±32	Pi2

5.3 Observations

The Frey substorm database contains the onset times and locations for substorm onsets identified by the FUV imager, at a cadence of 2 minutes, onboard the IMAGE satellite between May 2000 and December 2005 [*Frey et al.*, 2004; *Frey and Mende*, 2006]. These onset times were identified as the frame showing the first evidence of auroral

intensification, the onset location being described as the brightest pixel in the frame. High-resolution, 1 second cadence, GPS-timed CARISMA magnetometer data was available for the entire upgraded CARISMA array from 1st of April 2005. In order to establish the relationship between the timing and spatial location of AWESOME onsets with those in the Frey database, we chose to examine onsets between 1st April 2005 and the end of December 2005. The event list was narrowed by selecting substorm onsets which occurred between ~0530 magnetic local time (MLT) and ~0930 MLT, corresponding to intervals where magnetometers from the available arrays were closest to local midnight. From the identified events, four isolated substorms were chosen at random for detailed comparison to the Frey IMAGE-FUV onset location and time. Note that due to the IMAGE orbit, all of the Frey substorms occurred where IMAGE was viewing the southern hemisphere and were mapped using the Tsyganenko field model to the northern hemisphere. Østgaard et al. [2004; 2006] have shown that an asymmetry exists between substorm onset locations observed in the northern and southern hemispheres which may be described as a function of the IMF clock angle. For the events studied herein we find the IMF clock angle lies between ~30- ~200 degrees, corresponding to a separation of less than ~1.5 MLT hours between the northern and southern hemispheric onset locations according to the Østgaard et al. [2004; 2006] statistics . The north-south hemispheric-asymmetry for each of the events studied here is roughly equal to the longitudinal separation of the magnetometers utilised in this study, thus validating the approach of using conjugate mapping of southern hemisphere auroral features to the northern hemisphere adopted here.

5.3.1 Case 1: 3rd June 2005

Figure 5.2 shows the H- and D-components of the magnetic field on the 3rd June 2005 between 0515 -0645 UT for selected CARISMA, THEMIS and CANMOS magnetometers. A substorm is observed at ~0545 UT, visible through the formation of a negative H bay at GILL and coincident large amplitude Pi2 oscillations. The Frey database indicates that the onset of the substorm in the southern hemisphere occurred in the IMAGE-FUV data at 0544:23 UT (vertical blue line). The red vertical line in Figure 5.2 represents the initial onset of Pi1/2 activity which occurred first in the *j*=5 band (24-96 s) as determined by the AWESOME technique at the GILL magnetometer station at 0540:48 UT (± 16 s), the epicentre of ULF wave activity.

The results from the AWESOME algorithm from GILL are shown in Figure 5.3. The top two panels show the H- and D-components of the magnetic field during the substorm interval. The bottom panels (c-h) represent the wavelet coefficients, $\alpha_{j,k}$, for *j*'s from 9-4, the horizontal grey line represents the value of the 2σ threshold for each *j*. The substorm onset time as defined by the AWESOME technique in this case is determined from the *j* = 5, *k* = 10 wavelet coefficient; this being the first band with power that continuously exceeds the threshold. When performing the timing analysis, all wavelet bands at each station are studied. In this event the ULF wave power in the *j* = 5 band is the first to rise continuously above the threshold at each station, although the time when this occurs differs from station to station. For subsequent events in this Chapter it is sometimes the *j* = 6 wavelet band which shows this behaviour. We do not identify *a priori* band to study for any particular event, rather all wavelet bands are analysed to identify the correct timing information.

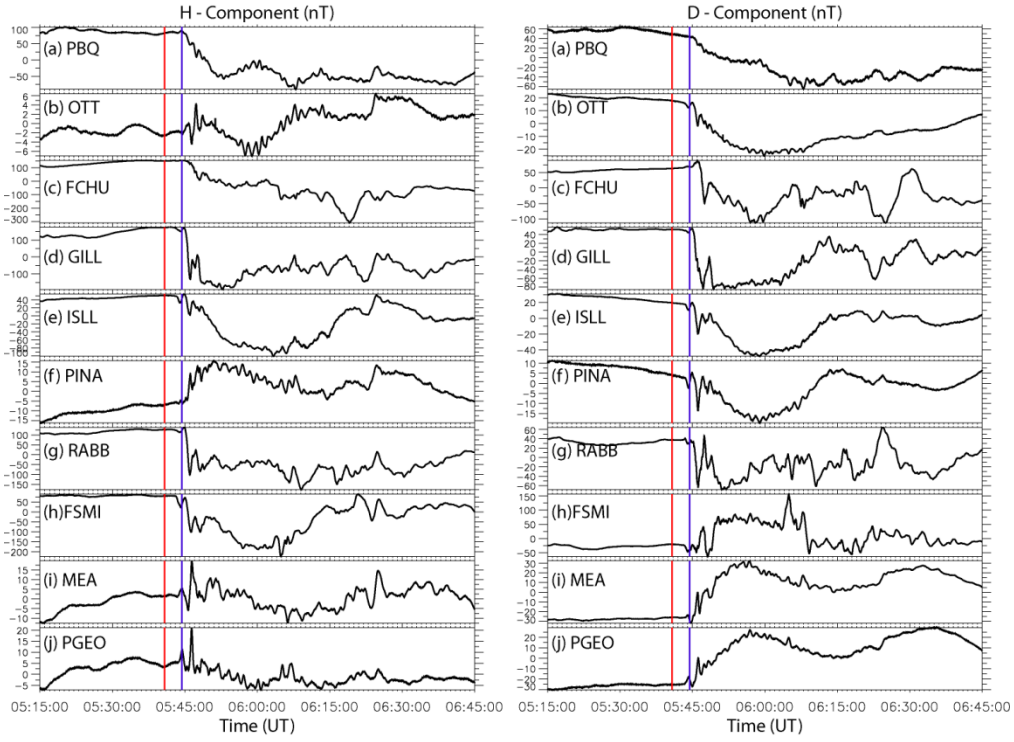

Figure 5.2: Selected H- and D-component magnetograms from 6th June 2005. The red line at 0540:48 UT depicts the ULF onset determined via AWESOME. The blue line at 0544:23 UT indicates the time of Frey optical onset inferred from the IMAGE-FUV instrument.

Onset as determined by $\alpha_{5,10}$ is depicted by the vertical dashed line in each panel at 0540:48 UT (± 16 s). Figure 5.4 shows the onset of ULF activity in the *j*=5 band (top two panels), and the color coded DWT spectra (bottom two panels) for GILL, the initial station, and RABB, the subsequent station to observe the onset of ULF waves. Note that we have subtracted the noise threshold from the DWT power spectra shown in Figure 5.4 (c) and (d) and have normalised each wavelet band, such that power which is below the noise threshold is black and any color blocks show statistically significant power levels. Panel (a) is an inverse wavelet transform of the *j*=5 band shown in panel (b). Evident in the top two panels is the presence of continuous ULF power above threshold in the *j*=5 band at GILL prior to the observation of wavelet power at RABB (64 seconds later). Similarly, the bottom two panels show a clear onset of continuous ULF wave power in the *j* = 5 wavelet band first at GILL, at 304±16 s after the start of the plot at 0535:44 UT, followed by RABB at 368±16 s after 0535:44 UT.

Figure 5.5 is a minimum curvature fit of the onset times in the *j*=5 (24-96 s) band, for all available magnetometer stations. The maximum error in the fitted contour times and the actual onset times is at most on the order of seconds at each station, such that the contours are an excellent representation of the onset times at each station location. Each contour is 32 s apart, the temporal width of each $\alpha_{5,k}$. Figure 5.5 shows a coherent expansion of Pi1/2 wave onset times in the *j*=5 band away from an epicentre at GILL, GILL being the first station where ULF power rises continuously above the threshold. This behaviour is similar to the localisation and expansion of Pi1 wave power onset times observed by Milling et al. [2008]. The conjugate northern hemisphere onset location, mapped as the negative latitude of the southern hemisphere onset location from the Frey database, is also shown on Figure 5.5 as a red cross (labelled as Frey) to the east of GILL. The blue cross (labelled T96) is the Tsyganenko 96 (T96) [*Tsyganenko*, 1995] magnetic field trace of the southern hemisphere Frey IMAGE-FUV onset location into the northern hemisphere. Both locations are very close to GILL, consistent with the AWESOME determined ULF onset location. It is important to note that although the onset location determined by AWESOME is limited by the spatial coverage and separation of the available magnetometer stations, the close proximity of the Frey

optical and AWESOME ULF onset locations validates the effectiveness of the AWESOME algorithm.

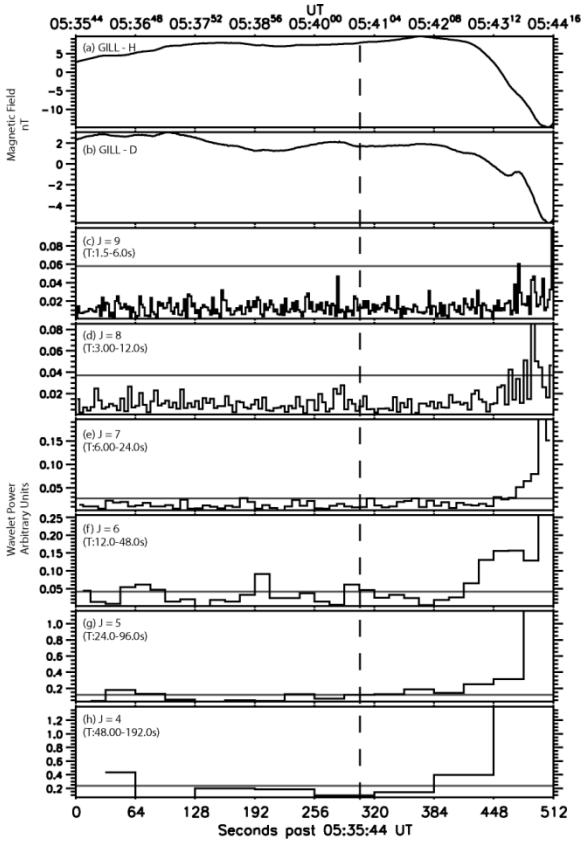

Figure 5.3: Depicts the implementation of the AWESOME algorithm at the GILL magnetometer. Panels (a)-(b) are the H- and D-components of the magnetic field. Panels (c)-(h) show the ULF wave power in the wavelet coefficients *j* = 9-4, respectively. The horizontal grey line in panels (c)-(h) represents the threshold for each *j* band. The dashed line depicts the onset at 05:40:48 UT represented by the *j*=5, *k*=10 wavelet coefficient in panel (g)

The position of the auroral electrojet and the upward and downward FACs can be estimated by comparing the magnetic bay perturbations in the H-, D- and Z-components to a SCW model consisting of dipolar FACs connecting through an ionospheric closure current [e.g., *Cramoysan et al.*, 1995]. These authors have determined the amplitude and the sign of the initial magnetic perturbations as a function of latitude and longitude with respect to a model SCW [see also, *Smith et al.*, 2002]. By fitting the substorm bay observed on this day it is estimated that the central meridian of the SCW lies between MCMU and PINA; however due to limited coverage, an accurate determination of the

east-west extent and latitude of the electrojet was difficult. We do note that the AWESOME determined onset location is east of the central SCW meridian, in the direction towards the downward FAC element.

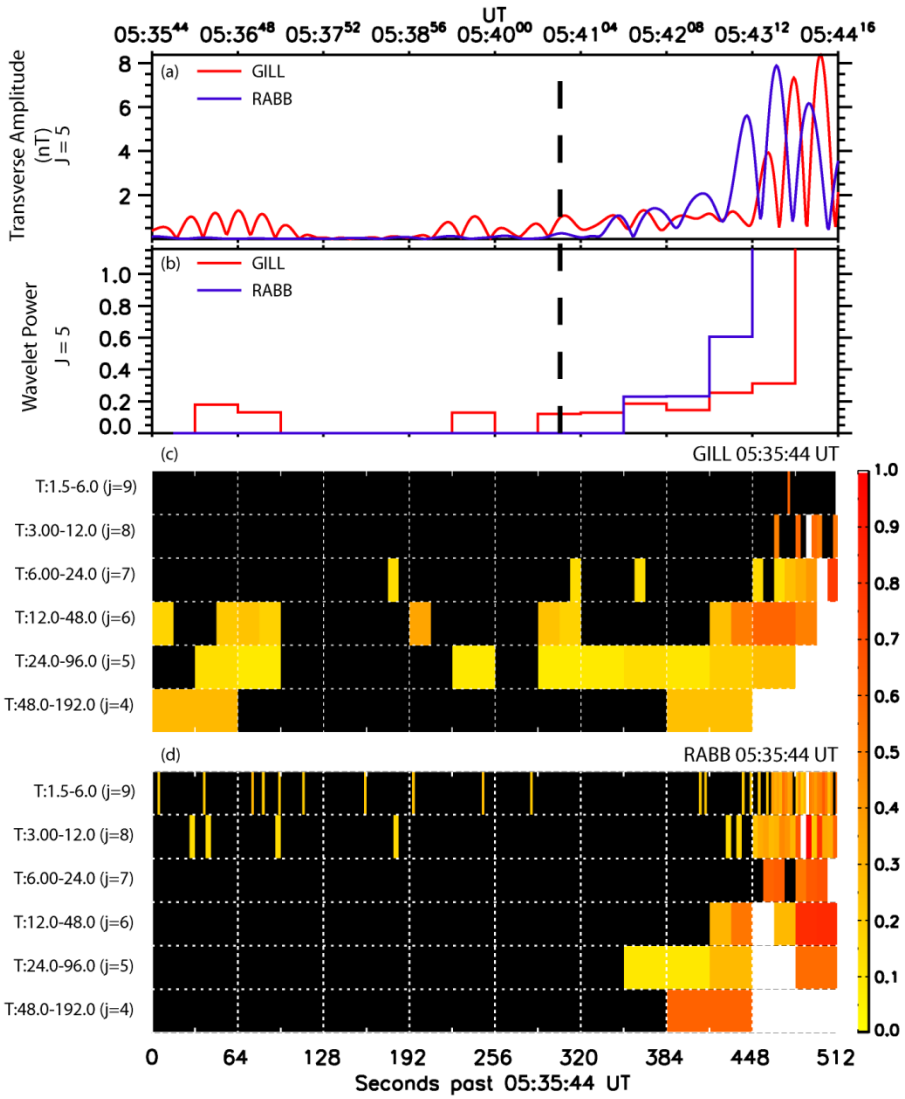

Figure 5.4: Panels (a) and (b) show the onset of ULF waves in the *j*=5 band for the GILL (red) and RABB (blue) magnetometers. Panel (a) shows the inverse transform of the transverse ULF amplitude determined from the *j*=5 wavelet coefficients shown in (b). The dashed line depicts the ULF onset at the GILL magnetometer station at 05:40:48 UT, 64 s before the onset at RABB. Panels (c) and (d) show the normalised Pi1 and Pi2 wavelet power spectra for *j*'s 9-4 at GILL and RABB, respectively. The x-axis denotes time, and y-axis period. Black represents wavelet coefficients below the determined threshold for each *j*, yellow-orange-red-white are coefficients rising above the threshold in increasing amplitude.

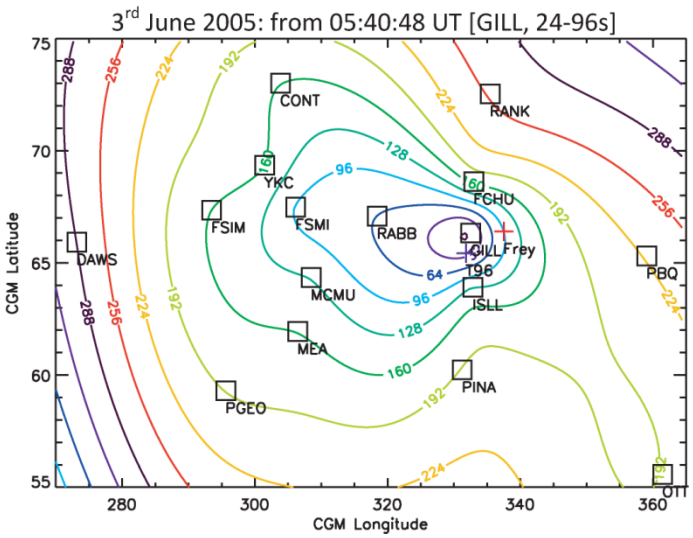

Figure 5.5: Contour plot of *j*=5 onset times determined by AWESOME on the 6th June 2005. ULF onset is observed first at the GILL and expands coherently in both latitude and longitude. The red cross denotes the conjugate northern hemisphere onset location in the Frey substorm database. The blue cross is the Tsyganenko field trace of the southern hemisphere onset location to the northern hemisphere.

5.3.2 Cases 2 and 3: 17th and 20th July 2005

Two substorms on the 17th and 20th July 2005 are analysed in this section providing further validation for the AWESOME technique. Figure 5.6 and Figure 5.7 show the H-component of the magnetic field from selected stations for 17th and 20th July 2005, respectively. Two magnetic substorms were identified in the Frey substorm database on the 17th July 2005: one at 0714:15 UT (first blue line in Figure 5.6) and the second at 0848:11 UT (second blue line in Figure 5.6). A third isolated magnetic event on the 17th July 2005 can be seen in the highlighted section of Figure 5.6 between 0800-0830 UT, and will be addressed in more detail in the next sub-section. The first red line depicts the onset time at FSMI which occurred first in the *j*=6 frequency band as determined by the wavelet algorithm at 0706:28 UT (± 8 s). Note however that the IMAGE determination of substorm onset during this event is relatively uncertain, ~9 minutes, as IMAGE was experiencing tracking difficulties between ~0705 and ~0714 the onset region shifted out of the field of view of IMAGE and the onset time may in actuality be more consistent with the ULF determined onset time. The second red line depicts the ULF onset in the *j*=5 wavelet band for the final event, which occurs first in this band at GAKO, at 0835:48 UT (± 16 s). The Frey substorm data base identifies a single substorm on the

20th July 2005 at 0530:53 UT, identified by the blue line of Figure 5.7, the red line showing the DWT ULF onset which occurred first in *j*=5 at 0524:24 UT (±16 s) at MCMU.

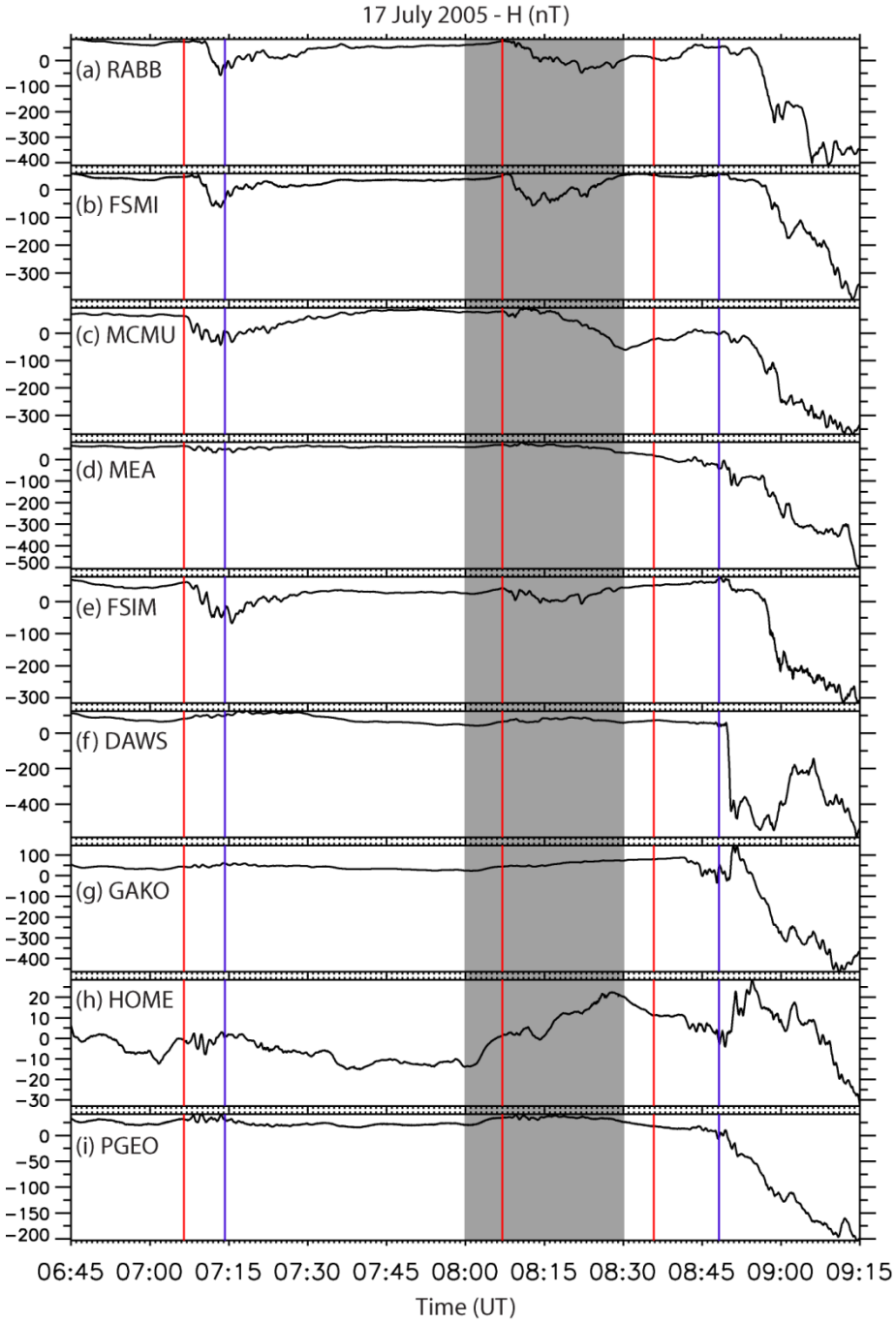

Figure 5.6: The H-component magnetic field from select magnetometers on the 17th July 2005. The red lines, 07:06:28 UT and 08:35:48 UT, represent the ULF onset. Blue lines, 07:14:15 UT and 08:48:11 UT, depict the optical onset times. The highlighted region is a localised pseudo-breakup discussed in further in Section 5.3.3 and Figure 5.9.

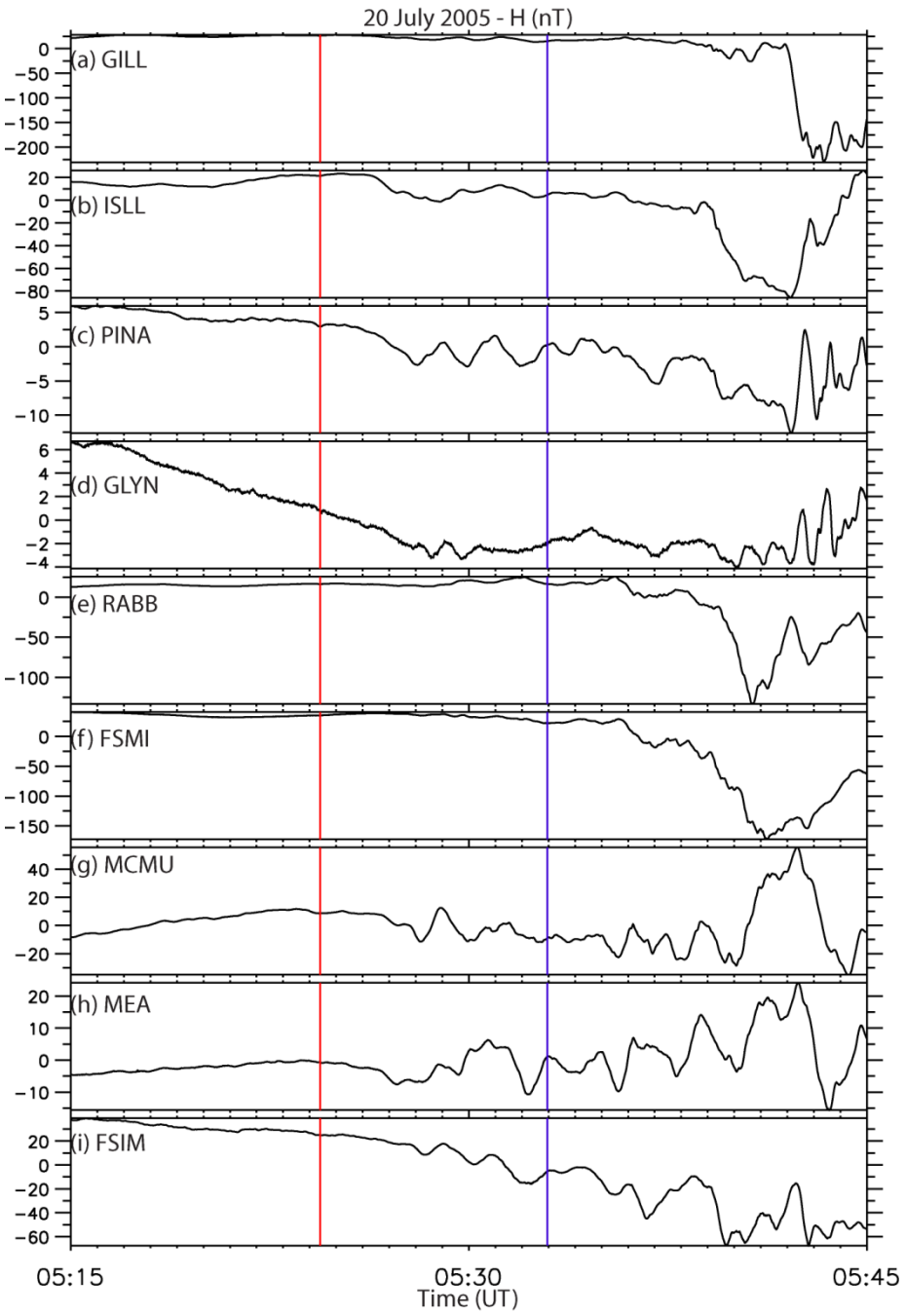

Figure 5.7: Select H-component magnetic time-series on the 20th July 2005. Red line is the ULF onset at 05:24:24 UT, and the blue line, the optical onset at 05:32:57 UT.

Figure 5.8 shows a minimum curvature contour plot of the delay in the onset of ULF wave activity (same format as Figure 5.5) for these three events on the 17th and 20th July 2005. Figure 5.8 (a) shows the expansion of the *j*=6 onset for the first substorm and panel (b) the expansion of the *j*=5 onset of the second substorm on the 17th July 2005.

Figure 5.8 (c) shows the expansion of ULF wave (*j*=5) onset times during the substorm observed on the 20th July 2005. In each panel, the location of substorm onset mapped to the northern hemisphere is labelled by the red and blue crosses. The red cross is the conjugate northern hemisphere onset location as determined by Frey et al. [2004] (negative latitude of the southern hemisphere onset location) and the blue cross is the T96 magnetic trace of the Frey onset location in the southern hemisphere to the northern hemisphere. Apparent during each substorm is a clear propagation of the onset ULF wave activity away from a localised epicentre. This epicentre occurs at FSMI, GAKO, and DAWS in panels (a, b, and c) respectively, in each case lying close to the onset location as determined by Frey et al. [2004] and mapped into the northern hemisphere.

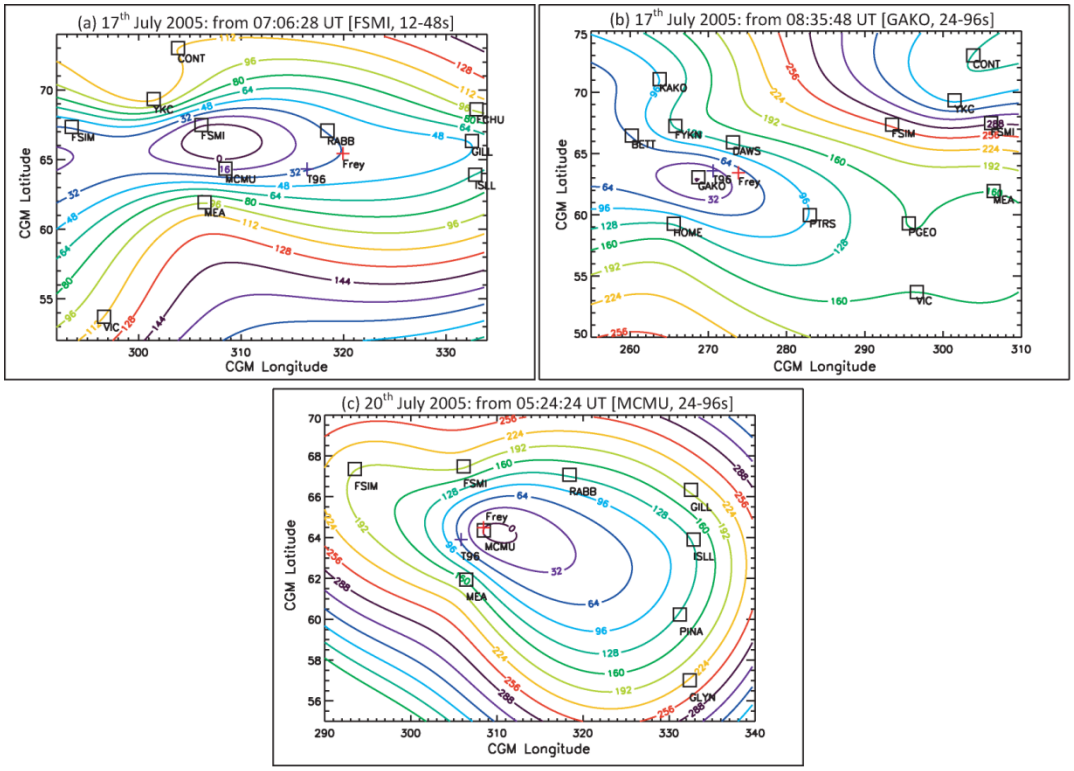

Figure 5.8: Contours of the ULF onset time for: (a) The initial substorm on 17th July 2005 in the *j*=6 wavelet band; (b) The second substorm on the 17th July 2005 in the *j*=5 wavelet band; (c) The 20th July 2005 substorm in the *j*=5 wavelet band. The red crosses in each panel are the conjugate northern hemisphere Frey onset locations. Blue crosses are the T96 field trace of the southern hemisphere optical onset location to the northern hemisphere.

The Cramoysan et al. [1995] SCW model analysis of the H-, D- and Z-component bays for these three substorms yields an estimate for the latitude and meridians of the electrojet and upward and downward FACs. The electrojet for the first substorm observed on the 17th July 2005 (0706:28 UT) was centered approximately between MCMU and RABB in longitude, and between MEA and FSMI in latitude. The downward FAC system lies east of the "Churchill" line of magnetometers (FCHU-GILL-ISLL-PINA) and the upward FAC approximately in the VIC meridian. For the second substorm on the 17th July 2005 (0835:48 UT) the central meridian of the auroral electrojet was east of DAWS, and between GAKO and HOME in latitude. Due to limited coverage to the east and west for this substorm accurate determination of the meridians of the FAC elements was not possible. On the 20th July 2005 the magnetic bays are small and combined with limited mid-latitude coverage, we were unable to accurately determine the location of the electrojet and corresponding meridians of the FAC.

5.3.3 Case 4: Isolated substorm between 0800-0830 UT 17th July 2005

The bays associated with the second event observed on the 17th July 2005 (shaded region in Figure 5.6) are small and localised. The highlighted section between 08:00 and 08:30 UT in Figure 5.6 is shown in detail in Figure 5.9. Evident in Figure 5.9 (a) and (b), is the formation of a small amplitude negative bay in the H-component at RABB and FSMI at ~08:10 UT. The remaining stations show limited deflection of the H-component magnetic field; however Pi2s are readily observed which suggests the formation of a localised substorm or perhaps a pseudo-breakup [e.g., *Baker et al.*, 1996 and references therein; *Voronkov et al.*, 2003].

Though the extent of this magnetic event is limited, the onset and subsequent expansion of ULF waves can still be characterised. Figure 5.10 shows a contour plot of the onset and expansion of ULF waves in the *j*=5 (24-96s) wavelet band (same format as Figure 5.5). The ULF wave onset is observed simultaneously at the FSIM, FYKN and DAWS magnetometers at 08:07:00 UT (±16s, black line Figure 5.9) suggesting that the onset of ULF power lies between these three stations. Similar to the previous four events, the ULF wave onset expands coherently across the available magnetometer stations.

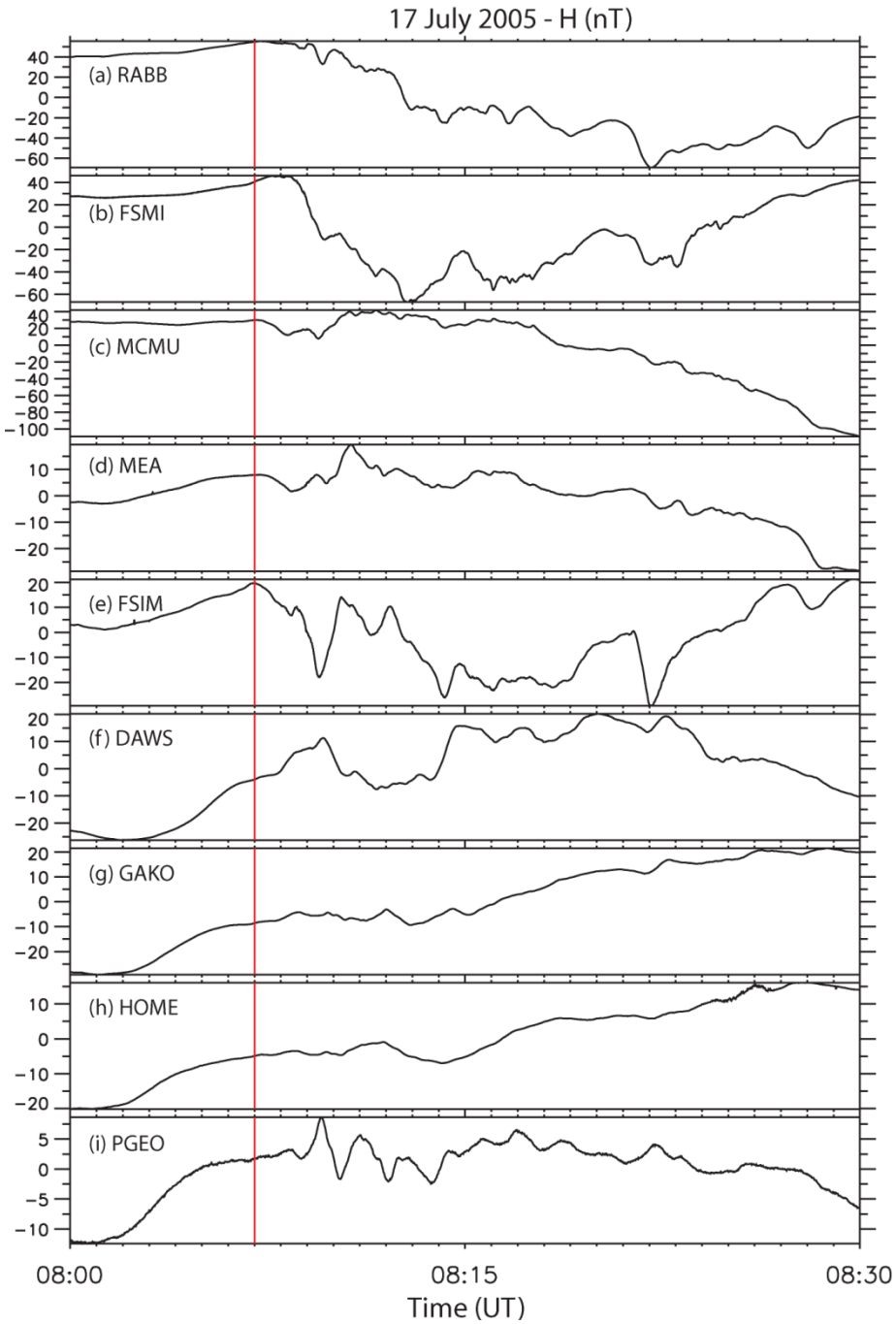

Figure 5.9: An expanded view of the highlighted portion of Figure 5.6. The black line depicts the ULF onset of a pseudo-breakup event at 08:07:00 UT; no optical onset for this event is identified in the Frey substorm database.

A localised auroral brightening is seen by the IMAGE-FUV instrument at approximately 0808 UT on 17th July 2005 (data not shown), coincident in time (to within instrumental resolution) with the onset of ULF waves at the FSIM, FYKN and DAWS magnetometer

stations. Unfortunately during this interval, the IMAGE satellite experienced tracking difficulties which caused the auroral oval to shift in and out of the field-of-view of the FUV instrument. As such, the limited spatial and temporal expansion of the auroral oval observed by IMAGE-FUV fails to meet the criteria set forth by Frey et al. [2004] to be included in the substorm database; however the auroral brightening seen in the FUV data suggests that the intensification may be indicative of a pseudo-breakup or other intensification which is not followed by auroral breakup (i.e., the poleward expansion and breakup of the main arc into multiple arcs). This localised event suggests that the AWESOME technique may also be utilised to determine the onset of ULF phenomena and their resulting spatial and temporal expansion during pseudo-breakup events [see for example, *Rae et al.*, 2009a; 2009b].

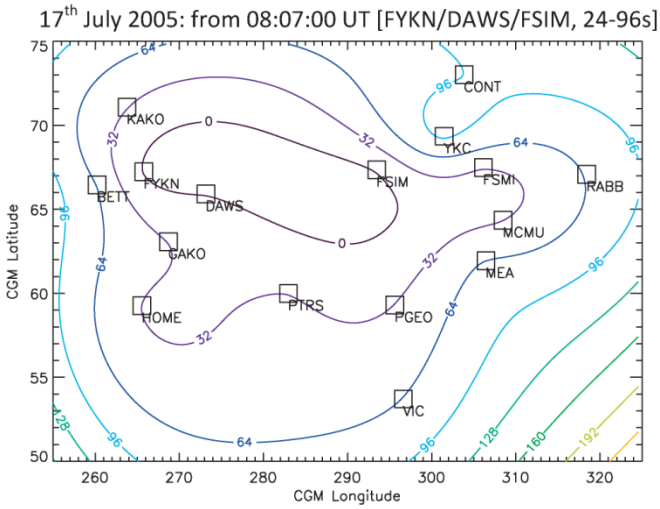

Figure 5.10: A contour plot of the ULF onset times for the pseudo-breakup observed between 08:00 – 08:30 UT on the 17th July 2005. The first ULF onset occurred in the *j*=5 wavelet band.

5.3.4 Compound Substorm expansion event on the 18th November 2005

While the wavelet algorithm is able to successfully characterise the ionospheric arrival times of Pi1 ULF waves during isolated substorms onsets, it is clearly more difficult to determine the onset timing and propagation during events in which multiple onsets, localised pseudo-breakups, or ULF precursors associated with discrete arc brightenings are observed prior to the full expansion phase onset. One such compound event was observed on the 18th November 2005. Figure 5.11 shows the AWESOME determined timings of the first ULF power to exceed threshold, which occurs in this instance in the

j=5 band. The initial disturbance is observed first at the FCHU and GILL magnetometers at 0605:24 UT (±16 s) followed by RABB and YKC 64s later. Apparent in Figure 5.11 are two regions from which the *j*=5 waves expand; one centered on the FCHU-GILL magnetometers and the second centered about the YKC magnetometer. The Frey database indicates that substorm onset occurred at 0609:29 UT, in the southern hemisphere at the CGM latitude and longitude of –65.93°, 301.66° respectively. Figure 5.11 shows the inverse magnetic location as a red cross at +65.93°. The T96 trace to the northern hemisphere is located at CGM latitude and longitude of 65.71° and 303.86°, shown in Figure 5.11 as a blue cross. The conjugate Frey and T96 northern hemisphere onset locations both lie between the MCMU, FSMI and FSIM magnetometers. As described above the wavelet algorithm indicates the ionospheric onset occurred first in the *j* = 5 (Pi1/2) wavelet band at the FCHU and GILL magnetometers. However the second YKC epicentre of the Pi1/2 activity is approximately coincident with the two mapped Frey onset locations. Such an expansion pattern suggests the Pi1/2s observed at FCHU and GILL might be a localised magnetic phenomenon which occurs prior to the full onset of the substorm.

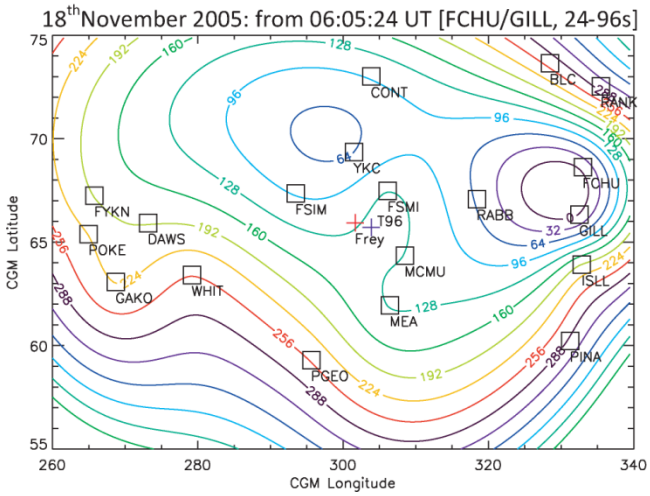

Figure 5.11: Contour plot of ULF onset times in the *j*=5 wavelet band on 18th November 2005, during a compound magnetic substorm. Conjugate optical onsets are indicated by the red (Frey) and blue (T96 field trace) crosses.

Rae et al. [2009a; 2009b] have shown that prior to the full expansion of the aurora during substorm break-ups, spatially localised auroral brightening can be observed

coincident with Pi1 and Pi2 wavepackets. From analysis of these other events, we suggest that on the 18th November 2005, similar localised auroral signatures near the GILL and FCHU magnetometers are responsible for the initial ULF activity observed prior to the full onset of the substorm which begins 64 s later and has an epicentre to the west of these stations. Indeed the GILL meridian scanning photometer in the NORSTAR array of the Canadian Space Agency Canadian Geo-Space Monitoring program (data not shown) shows evidence of local auroral brightening at approximately 0605 UT several minutes prior to the substorm breakup.

Indeed, it is possible to interpret the disturbance observed at FCHU and GILL as a precursor and identify a second intensification of Pi1/2 activity after the initial rise of Pi1/2 ULF activity above pre-substorm background noise. This produces a more coherent pattern of temporal expansion of Pi1/2 signals away from a single epicentre close to YKC, near the Frey onset location. Figure 5.12 shows results which arise when the time of the second burst of Pi1/2 activity is considered at FCHU and GILL. Note there is now a clearer expansion of substorm onset related Pi1/2 activity, centered on a single epicentre.

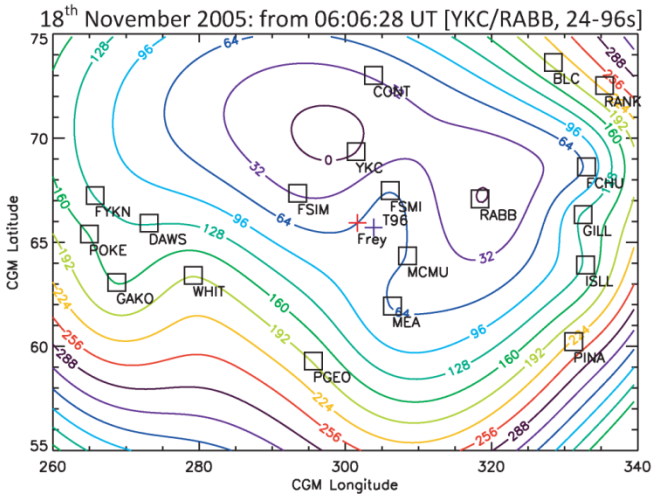

Figure 5.12: Contour plot of the ULF intensifications in the *j*=5 wavelet band on the 18th November 2005, during a compound magnetic substorm. Conjugate optical onsets are indicated by the red (Frey) and blue (T96) crosses.

Figure 5.13 (a) shows the H-component magnetic field observed at the YKC (grey) and FCHU (black) magnetometers. The dashed grey lines depict the initial onset of ULF

power at FCHU and the second intensification of ULF power, the black dashed line indicates the onset ULF power at YKC and the dotted line depicts the onset time identified in the Frey substorm database. Panels (b) and (c) of Figure 5.13 show the inverse wavelet transform of the *j*=5 band the *j*=5 wavelet power, respectively. Apparent in (c) are two packets of wave power observed at FCHU (grey), indicated by the grey dashed lines, and a continuous rise in power at YKC (black), identified as the onset of the substorm (dashed black line) . The initial packet observed by FCHU is associated with the localised auroral brightening apparent in the GILL MSP and the second packet is the onset of the substorm identified by IMAGE in the Frey database. While the wavelet algorithm is an excellent tool for determining substorm onset and the resulting expansion of ULF waves, this example illustrates that care must still be taken when identifying Pi1s and Pi2s and associating them with substorm onset. Arc brightenings and auroral dynamics can also often be associated with Pi1/2 activity which will also be detected by the AWESOME DWT algorithm.

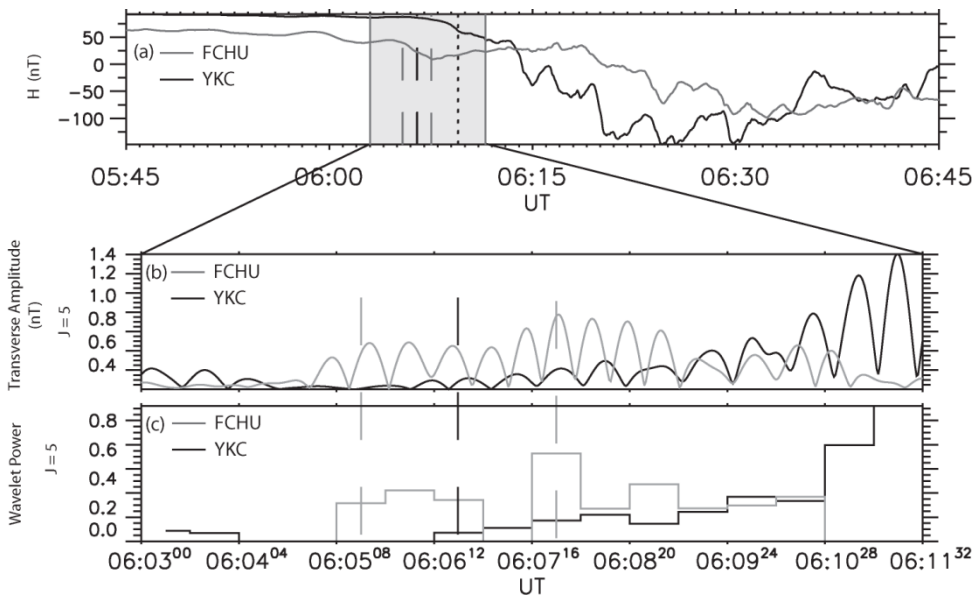

Figure 5.13: Panel (a) shows the H-component magnetic field observed by the YKC (black) and FHCU (grey) during the compound substorm on 18th November 2005. The first grey dashed line indicates the onset of ULF wave power at FCHU associated with a localised brightening of the aurora, the second grey dashed lined depicts intensification of Pi/2 power, the black dashed line indicated the onset of ULF power observed by YKC and the onset of the magnetic substorm identified in the Frey substorm database. Panel (b) shows the inverse wavelet transform of the *j*=5 wavelet band for the YKC (black) and FCHU (grey) magnetometers. Panel (b) is the *j*=5 wavelet power at YKC (black) and FCHU (grey). The dashed lines in Panels (a) and (b) are the same as those in Panel (a).

The position and extent of the SCW can also be estimated by the initial H, D and Z bays seen following the onset of this substorm. The approximate centre of the SCW lies at a longitude between FSMI and RABB and at a similar latitude to both stations. The upward FAC meridian lies between FSIM and DAWS and the meridian of the downward FAC system lies to the west of the "Churchill" line between RABB and GILL. In this case the optical and Pi1/2 ULF onset locations lies between the upward and downward FAC element.

5.4 Discussion

Each of the five substorms from the Frey database, as well as the localised pseudo-breakup observed at ~08:00 UT on the 17th July 2005, studied here show a universal picture of a coherent expansion of the onset of Pi1/2 ULF waves away from a localised onset epicentre in the ionosphere. Angelopoulos et al. [2008] showed that the westward travelling surge (WTS) expands azimuthally in the ionosphere at a rate of ~15° in longitude per minute. The typical longitudinal expansion rate of the onset of Pi1/2 ULF waves in the events studied here is ~30 seconds per 10° of magnetic longitude. The observed Pi1/2 ULF wave onset expansion rate reported here is hence faster than that of the WTS. This is in agreement with the observations of Samson and Harrold [1995] who concluded that the excitation mechanism of ULF waves at expansion phase onset is different than that responsible for the auroral break up and subsequent propagation of the WTS.

Using a fit to the substorm magnetic bays [*Cramoysan et al.*, 1995], the location of the SCW in four of the six events was compared to the AWESOME-determined Pi1 onset location. In these four events the center of the latitude of the electrojet in the SCW was found to be co-located with the latitude of both the (conjugate) optical Frey IMAGE-FUV and AWESOME Pi1 ULF wave onset locations. Of these four events, two were located in a region of the North American sector in which there was sufficiently dense mid-latitude and auroral magnetometer coverage surrounding the onset location to estimate the meridians of the FAC elements in the SCW. Milling et al. [2008] have suggested that the location of the epicentre of Pi1 ULF wave onset is co-located with the region in which the downward FAC element subsequently develops. On the 17th July 2005 the onset location was found to lie between the upward and downward FAC elements. On the 18th

November 2005 both the Pi1/2 ULF and Frey optical onsets were close to the upward FAC element of the SCW, though as described in Section 5.3.4 the observed substorm was compound in nature. This evidence suggests that a localised auroral brightening occurred close to the FCHU-GILL magnetometers prior to the full onset of the substorm which occurred 64s later to the west and centred close to YKC. For this event, the ULF epicentre and the Frey optical onset appear to be between the locations of the upward and downward FAC meridians. Note however that the spatial resolution available to the SCW technique is limited by the separation of the stations in the array such that spatial errors in determining the meridians of the SCW elements can be as large as the longitudinal station separation. Further note that care must be taken in inferring the meridian and latitude of the SCW system since there is flaring of the zero crossings in the average magnetic bay perturbations [*Cramoysan et al.*, 1995], and thus the longitudinal magnetic bay structure is a function of latitude.

The DWT analysis presented in this Chapter demonstrates a clear relationship between the location of the first ionospheric Pi1/2 activity, and the location of the global scale substorm auroral brightening which can be seen with the global scale FUV imager on the IMAGE satellite validated via comparison to five substorms in the Frey substorm list. Further, independent location of the SCW current system by analysis of the substorm bays shows a close correspondence between the latitude of the electrojet and the Pi1/2 onset, and the meridians of the centre of the SCW or the meridian of the downward FAC element, which subsequently develops. In their recent paper, Milling et al. [2008] also found a spatial correspondence between the location of the ULF onset and the location where the downward FAC element subsequently develops.

One obvious interpretation for the close spatial correspondence between the SCW central meridian/downward FAC element with the Pi1/2 onset epicentre is that the Pi1/2 epicentre reflects the field-aligned ionospheric image of the perturbations created in the magnetosphere by the mechanism triggering expansion phase onset. It is possible that the Pi1/2 (j=5 or 6) waves are a signature of the first seconds of the substorm expansion phase onset process in the ionosphere. Significantly, the rate at which the Pi1/2 onset propagates in latitude and longitude in the ionosphere is much slower than the time taken for shorter period (1-10 s period) Pi1B signals to propagate in the Earth-

ionosphere waveguide [*Lysak*, 1988], ruling out a role for the waveguide in the expansion of the Pi1 onset signal reported here. Similarly, assuming an Alfvén speed of 1400 km/s in the magnetosphere at geosynchronous orbit (B=100nT, n=3/cc) results in an azimuthal propagation speed in the ionosphere of ~10 seconds to travel 1 hour of MLT of longitude. This Alfvénic propagation time is thus much faster than the observed expansion of the Pi1/2 onset times observed by the individual magnetometers in the ionosphere, suggesting that any cross-field propagation of a source region of the onset-related Pi1/2s in the magnetosphere occurs much slower than the local Alfvén speed. It is possible that the Pi1/2 signals identified by the wavelet transform represent the arrival of an Alfvén wave excited by disturbances which may map to a localised region of the magnetotail where the cross-tail current is diverted into the ionosphere to form the SCW. In principle such a signal could be generated in a localised region by CD in the magnetotail, or in the process of flow braking [e.g., *Shiokawa et al.*, 1997; 1998] following reconnection further tail-wards in the NENL model. If however the region of the nightside magnetosphere is extremely elongated then the initial expansion of the Pi1/2 may be a result of the direct propagation of an Alfvén wave along the plasma sheet boundary layer from the reconnection region corresponding to the NENL. Conjugate studies of future events combining in-situ data from the magnetotail with ionospheric onset diagnosis using AWESOME will enable this hypothesis to be tested and perhaps enable the driver of Pi1/2 onset waves to be uniquely determined.

Despite the need for further in-situ studies, our observations are consistent with the following scenario. The first Pi1/2 waves characterise the arrival in the ionosphere of Alfvénic disturbances triggered by the expansion phase onset process in the magnetotail. Subsequently, the power in the Pi1 and Pi2 bands gradually increases for ~2 minutes. During this time the onset arc intensifies, and after ~2-3 minutes auroral breakup follows, characterised by a rapid and large increase in Pi1 and Pi2 power. The initial low power Pi1/2s reported here can therefore be used to time and locate the very first signatures of onset in the ionosphere. Auroral break-up and the build up of the FAC in the SCW are only established later as a result of the propagation and reflection of large amplitude Alfvén waves, historically characterised in the magnetograms as Pi2s. Finally, the westward drift of substorm injected ions in the magnetosphere creates a westward expansion of the spatially distributed upward FAC in the WTS. This expansion

of the WTS most likely occurs as the result of $j_{||} \propto \nabla P \times \nabla V$, where P is the pressure and V is the flux tube volume [e.g., *Vasyliunas*, 1970], driving an upward FAC which expands westwards under the pressure gradient front arising from gradient curvature drift of the injected ions [c.f., *Lyons*, 1995]. The large scale auroral brightening identified in the FUV images characterises the onset of the substorm in the Frey database several minutes after the time that ULF wave power first exceed the quiet time threshold.

A very important question concerns the origin of the Pi1/2 waves seen in the ionosphere, especially the physical implications of the existence of the Pi1/2 wave onset epicentre in the ionosphere. Previous optical studies have observed the occurrence of small-scale auroral undulations immediately prior to expansion phase onset [e.g., *Donovan et al.*, 2006; *Liang et al.*, 2008; *Rae et al.*, 2009a; *Rae et al.*, 2009b]. In order to link the optical and magnetic manifestations of expansion phase onset, Rae et al. [2009a] determined that the epicentre of long period Pi1 ULF wave activity in the ionosphere is coincident in both time and space with these small-scale auroral beads or arc undulations that form on the most equatorward arc prior to auroral breakup. Furthermore, Rae et al. [2009a] determined that the most poleward arcs remained undisturbed during the development of this Pi1/2 signature and during the development of the auroral beads. This suggests that the Pi1/2 onset is an ionospheric signature of a CD mechanism in the near-Earth plasma sheet, the signatures evolving for several minutes prior to the disruption and breakup of more poleward discrete arcs which map to the nightside central plasmasheet. Alternatively, in an extremely stretched tail the initial expansion of Pi1/2 waves in the ionosphere may extend into the distant magnetotail, the onset of ULF wave activity thus being associated with the triggering of reconnection and the substorm expansion phase, consistent with the NENL model. However, in such a scenario the development of auroral undulations at latitudes lower than the pre-existing and quiescent poleward arc must be successfully explained [e.g., *Rae et al.*, 2009a]. More studies including in-situ data are needed to provide conclusive evidence of the location and driver of the initial magnetospheric disturbance.

5.5 Conclusions

In this Chapter we describe the implementation and validation of a discrete wavelet transform algorithm, AWESOME, which enables the determination of the magnetic

onset of Pi1/2 ULF waves in the ionosphere during magnetic substorms. The wavelet algorithm is able to probe the initial seconds of the expansion phase onset with high temporal resolution, ~20 -40 s. Furthermore, using a network of stations, the onset of the Pi1/2 waves can be mapped as a function of latitude and longitude in the ionosphere. This reveals a coherent pattern of the propagation of the onset of Pi1/2 waves above pre-substorm background noise which has a clear ionospheric epicentre.

The location of the ULF wave epicentre has been validated by comparing the ULF onset time and location with five selected substorms identified in the Frey et al. [2004] IMAGE-FUV substorm database. In each case the ULF wave onset is observed prior to optical onset as defined in the Frey substorm database, with the epicentre lying in close spatial proximity to the conjugate northern hemisphere Frey onset location (red crosses Figures 5.5, 5.8a, 5.8b, 5.8c, 5.11 and 5.12) and as well as the T96 field trace of the southern hemisphere onset location into the northern hemisphere (blue crosses Figures 5.5, 5.8a, 5.8b, 5.8c, 5.11 and 5.12). In all of the substorms reported here, the global scale auroral intensification recorded by the IMAGE-FUV instrument and identified as substorm onset occurs ~2 minutes, and in one case as long as 12 minutes (though due to IMAGE tracking problems the uncertainty in the onset time is approximately 9 minutes) after the wavelet-determined Pi1/2 onset time. Even though the FUV camera has ~2 minute cadence, the global intensification of the aurora occurs during these substorms generally occurs several minutes after the first coherent and continuous observation of Pi1/2 ULF wave power above the background noise threshold. The ability to detect the initial and localised ionospheric onset of the substorm expansion phase to within ~20-40 s is essential to understanding the sequence of events during the substorm expansion. The AWESOME technique meets the ionospheric timing requirements of the THEMIS mission[*Angelopoulos*, 2008], showing the value of the AWESOME wavelet algorithm.

It has been suggested [e.g., *Angelopoulos et al.*, 2008; *Baker et al.*, 1996; *Lui*, 1996] that the unambiguous identification of the magnetospheric processes responsible for triggering substorm expansion phase onset has been thwarted in the past due to limited spatial and temporal observations during expansion phase onset. Both in-situ and ground-based observations across an extended region are required at high temporal

cadence and high spatial resolution in order to resolve the causal sequence of events at substorm expansion phase onset and distinguish between competing CD and NENL models. The AWESOME technique described here offers the capability to not only provide a high temporal resolution (~20-40 s) diagnosis of the first ionospheric signatures of substorm expansion phase onset, but also to spatially locate the epicentre which characterises the ionospheric region of the first Pi1/2 activity. Such continent scale magnetic Pi1/2 timing and location, as provided by the AWESOME wavelet technique described here, will be crucial for interpreting in-situ substorm signals, for example from the THEMIS probes, and ultimately for solving the substorm problem.

Chapter 6 The Dependence of Pi2 Waveforms on Periodic Velocity Enhancements within Bursty Bulk Flows[2]

Summary

Pi2s are a category of Ultra Low Frequency (ULF) waves associated with the onset of magnetic substorms. Recent work has suggested that the deceleration of bulk plasma flows in the central plasmasheet, known as bursty bulk flows (BBFs), are able to directly-drive Pi2 oscillations. These previous works have shown that there is a one-to-one correlation between Pi2 magnetic waveforms observed on the ground and periodic peaks in flow velocity within the BBF, known as flow bursts. Utilising a favourable conjunction between the Geotail spacecraft and the Canadian Array for Real-time Investigations of Magnetic Activity (CARISMA) magnetometer array on 31st May 1998, we examine the causality of the link between BBF flow bursts and Pi2 waveforms. Using a series of analytical tests, in both the time and frequency domains, we find that while the Pi2 and BBF waveforms are extraordinarily similar the ground response occurs prior to the flow enhancements in the magnetotail. We conclude that during this specific case study the temporal variations of the flow bursts within the BBF are not directly-driving the observed ground-based Pi2 waveforms, despite the fact that a visual inspection of both time-series might initially suggest that there is a causal relationship. We postulate that rather than there being a direct causal relation the similar waveforms observed in both Pi2s and BBFs may result from temporal variations in a common source for both the BBFs and the Pi2s, such as magnetic reconnection, this source modulating both the Pi2 and BBF at the same frequency.

6.1 Introduction

Ultra Low Frequency (ULF) waves have been associated with the onset and development magnetic of storms and substorms for over 40 years [Jacobs et al. 1964]. Specifically, a band of impulsive ULF waves known as Pi2s, with periods of 40-150 s, have traditionally been used as indicators of substorm onset [e.g., *Nose et al.*, 1998; *Saito*, 1969; *Saito et al.*, 1976]. The physical process or processes driving these impulsive ULF waves during

[2] Based on Murphy K. R. et al. (2009), The dependence of Pi2 waveforms on periodic velocity enhancements within bursty bulk flows, *J. Geophys. Res., submitted*

substorms is still being debated[e.g., *Chi et al.*, 2001; *Kepko and Kivelson*, 1999; *Kepko et al.*, 2001; *Rae et al.*, 2006; *Uozumi et al.*, 2000]. In general it is believed that Pi2s are generated by a disturbance in the near Earth plasmasheet which subsequently leads to the formation of the substorm current wedge (SCW) [*McPherron*, 1979]. The initial plasmasheet disturbance generates a field-aligned current (FAC) system which closes in the ionosphere, established by the reflection of Alfvén waves, seen as Pi2 waveforms superposed on magnetic bays observed on the ground [e.g., *Olson*, 1999 and references therein]. Substorm onset may also drive a compressional disturbance which propagates away from the source in the magnetotail and generates Pi2 phenomena in the ionosphere. These may include contributions to Pi2s in the form of FLRs on the flanks, plasmaspheric cavity modes, as well as a contribution from the initial formation of the SCW [see *Olson*, 1999 and references therein].

The ULF waves responsible for the generation of the SCW FAC system are believed to be the dominant source of Pi2s observed at mid- to high-latitude magnetometer stations. The initial FAC is established by an Alfvén wave which propagates to the ionosphere, and is reflected, perhaps multiple times. The observed ground-based magnetic perturbations are referred to as transient response (TR) Pi2s [*Olson*, 1999]. If the plasmasheet disturbance is large enough, the existing cross-tail current is diverted along field lines into the ionosphere, subsequently the SCW is observed as a widespread night-side current system. Any impedance mismatch between the ionosphere and the current carrying Alfvén wave may then cause a partial reflection to occur, with the wave bouncing along field lines between the ionosphere and plasmasheet leading to the characteristic periodic and decaying structure of the Pi2 [*Olson*, 1999]. However, Kepko et al. [2001] suggested that during periods of quiet geomagnetic activity the nightside ionospheric conductivity may be sufficiently low that any impedance mismatch between the ionosphere and Alfvén wave is negligible and produces little reflected ULF signal. Therefore during quiet periods the TR model could fail to adequately explain the characteristics of the observed Pi2 wavetrains.

The compressional, or fast-mode, wave produced by a substorm-related plasmasheet disturbance can travel almost isotropically and radially inward towards the Earth. This coupling can create a plasmaspheric cavity mode [e.g., *Sutcliffe and Yumoto*, 1991;

Yeoman and Orr, 1989]**,** or through coupling to an Alfvénic mode drive a field line resonance [e.g., *Rae et al.*, 2006]. The fast-mode wave is also believed to be the main source of Pi2s at higher latitudes when the TR mechanism is circumvented and the initial Alfvén wave does not reflect at the ionosphere [*Kepko et al.*, 2001]. Uozumi et al. [2000] and Chi et al. [2001] proposed that the latitudinal amplitude and phase structure of Pi2s can be characterised by the flight path of a compressional disturbance in the equatorial plane of the magnetotail and an Alfvénic disturbance along the background magnetic field lines [c.f., *Tamao*, 1964], and Kepko and Kivelson [1999] suggest that Pi2s are directly-driven by the deceleration of large amplitude earthward plasma flows.

In this Chapter we investigate the Kepko and Kivelson [1999; also see *Kepko et al.*, 2001] model (hereafter termed the Kepko model) in detail during one particular Pi2 event. In the Kepko model it is suggested that high-speed earthward plasma flows may rapidly decelerate in the dipolar region of the Earth's magnetosphere, being responsible for the initial near-Earth plasmasheet disturbance, and the deceleration of temporal variations in the flow velocity being responsible for directly driving the Pi2 waveforms observed on the ground. Plasma flows in the central plasmasheet (CPS) typically have velocities of approximately 30 km/s. However, high-speed flows are often observed with velocities approximately an order of magnitude larger than the typical plasmasheet velocity. These high-speed earthward flows are termed bursty bulk flows (BBFs) [*Angelopoulos et al.*, 1992], and have a typical velocities larger than ~400 km/s, and a duration of ~10 minutes. During these events short-lived, quasi-periodic, large amplitude peaks in plasma velocity can occur within a specific BBF, which are referred to as flow bursts (FBs) [*Angelopoulos et al.*, 1994]. BBFs are often observed as far as ~30 R_E down-tail and are rarely observed closer then ~10 R_E [e.g., *Angelopoulos et al.*, 1992; *Baumjohann et al.*, 1990]. This is believed to be evidence of flow braking in the inner magnetosphere due to an increase in magnetic pressure caused by the increase in the strength of the Earth's magnetic field as flows propagate toward the Earth [e.g., *Haerendel*, 1992; *Shiokawa et al.*, 1997].

Kepko and Kivelson [1999] proposed a mechanism by which BBFs and FBs may be causally related to the generation of Pi2s observed on the ground. By comparison of time-shifted FBs and Pi2 waveforms, Kepko and Kivelson [1999] and Kepko et al. [2001]

suggested that each ground-based Pi2 waveform observed was a direct consequence of each FB within a particular BBF. Specifically these authors suggested that additional FACs were induced inside the SCW region when BBFs are decelerated in the inner magnetosphere. This is termed the inertial current (IC) Pi2, and is hypothesised to be a small amplitude Pi2 waveform superposed onto the existing TR Pi2s and SCW. Further these authors suggested that the deceleration of BBFs could launch a fast-mode wave which perturbs magnetic field lines and directly drives Pi2s on the flanks and at lower latitudes, outside the SCW region.

We investigate the hypothesised relationship between BBFs and Pi2 oscillations in the nightside magnetosphere by selecting a small night-side event during which plasma flows are observed in the magnetotail by the Geotail spacecraft when it is conjugate to the Canadian sector, and a small isolated ionospheric current system and magnetic bays are observed on the ground, which are consistent with a small substorm or pseudo-breakup. We find that while Pi2s and BBFs are both associated with night-side activity, the temporal causality of the directly-driven model proposed by Kepko and Kivelson [1999] and Kepko et al. [2001] is not supported by our study. Indeed the Pi2 waveforms and BBF structure are shown to be remarkably similar; however, the ground signature is shown to occur prior to flow signatures in the CPS. We postulate that both signatures may be driven by the same source, which could allow for ground-based Pi2s to be observed prior to the BBF if magnetospheric conditions are favourable. Such a model can account for both the observation presented herein, as well as those reported by Kepko and Kivelson [1999] and Kepko et al. [2001].

6.2 Case Study: 31st May 1998

6.2.1 In-situ Observations

In order to test the hypothesis that BBFs directly drive Pi2 oscillations we examined a conjunction between the Geotail satellite [*Frank et al.*, 1994; *Kokubun et al.*, 1994; *Mukai et al.*, 1994]and the Canadian Array for Realtime Investigation of Magnetic Activity magnetometer array [*Mann et al.*, 2008] (CARISMA, operate as CANOPUS [*Rostoker et al.*, 1995], prior to 1st April 2005) during a small amplitude and isolated night-side event. On 31st May 1998, a conjunction between the Geotail satellite and

CARISMA magnetometer array occurred between 0400 and 0800 UT. The average solar wind speed and proton number density during this conjunction, observed by WIND at 186 R_E upstream, were 517 km/s and 2.5 n/cc, respectively, while the observed B_z was northward and B_y was predominantly positive. During the conjunction the Geotail satellite was situated in the nightside CPS, and observed a short duration BBF during this conjunction. The top panel of Figure 6.1 shows the northern magnetic footprint (obtained using Tsyganenko 89c external and IGRF internal geomagnetic fields [*Tsyganenko*, 1989], using the relevant Kp value of 1) of Geotail along with the location of the CARISMA ground-based magnetometer array and the lower latitude Los Alamos (LNL) magnetometer. The middle and bottom panels show the location of Geotail in the GSM x-y and x-z planes, respectively.

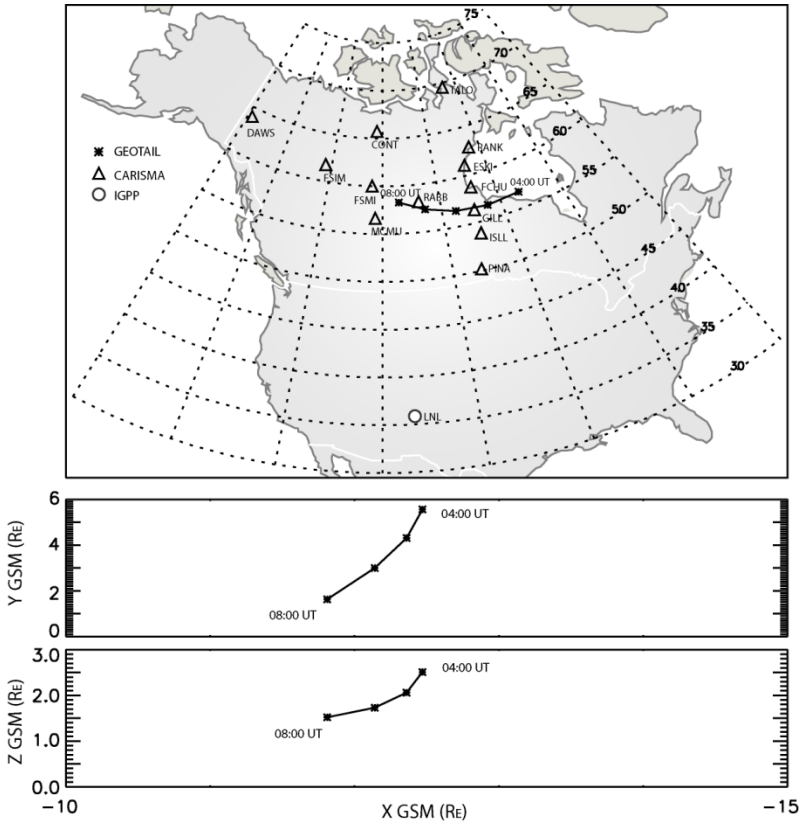

Figure 6.1: (a) Ground northern magnetic field trace of the conjunction between the Geotail spacecraft and CARISMA magnetometer array between 0400 and 0800 UT on the 31st of May 1998. The GSM location of Geotail in the x-y plane and x-z planes are plotted in panels (b) and (c), respectively.

During the conjunction between Geotail and CARISMA, a BBF was observed between 0549-0555 UT which contained four FB peaks. For the duration of the flow, Geotail was positioned at (x_{GSM}, y_{GSM}, z_{GSM}) = (-12.2, 3.3, 1.8) R_E. The large value of the ion-plasma beta, β_i, and the criterion that the ion-plasma beta be greater than 0.5 [*Angelopoulos et al.*, 1992; 1994 and references therein] is generally taken to indicate the spacecraft is situated within the CPS. Figure 6.2 (a) confirms that Geotail is located in a region of hot plasma characteristic of the CPS for the duration of the interval as the derived ion-plasma beta lies well above the 0.5 threshold. The plasma beta was derived from measurements provided by the Comprehensive Plasma Instrument (CPI) [*Frank et al.*, 1994]and the Geotail Magnetic Field Experiment (MGF) [*Kokubun et al.*, 1994]onboard the Geotail spacecraft.

Following the onset of the BBF, Geotail observes a dipolarization of the GSM magnetic field evident in the increase of the ratio of the magnitude of B_z to the magnitude of the vector sum B_x and B_y (Figure 6.2 b), as well as an increase in the z-component of the magnetic field (Figure 6.2 c). The dipolarization, observed at ~0549:30 UT, is characteristic of the relaxation of the magnetotail to a lower energy state during substorms, and is consistent with previous observations of BBFs during substorms [e.g., *Angelopoulos et al.*, 1992]. Note that there are no apparent Pi2s oscillations in the magnetic field observed at Geotail, Figure 6.2 (c), this is likely due to the motion of the plasma flow in the CPS which may generate incoherent or turbulent oscillations of the background magnetic field.

The bottom two panels of Figure 6.2, (d) and (e), show the observed GSM plasma velocity at Geotail from the Low-Energy Particle (LEP) instrument [*Mukai et al.*, 1994] and the derived plasma velocity in field-aligned (FA) coordinates, respectively. In the FA coordinate system the direction perpendicular to the background field and directed toward the earth is denoted by x_{FA}, z_{FA} is aligned along the field and y_{FA} completes the right handed coordinate system [see *Rae et al.*, 2005 for details]. Clearly evident between 0549 UT and 0555 UT is a strong, ~400 km/s, flow in the earthward FA plasma velocity (hereafter referred to as $v_{\perp x}$), corresponding to a strong earthward BBF. During this interval four FB peaks are observed within the $v_{\perp x}$ component of the BBF, with a temporal spacing on the order of one to two minutes and velocity peaks between 400

and 500 km/s. Note, a detailed analysis of the 2-D ion distribution functions from the LEP Editor-B data (not shown) verifies that the plasma flow, BBF and FBs, observed at Geotail was indeed a bulk plasma flow perpendicular to the background field and not a field-aligned plasma beam [e.g., *Raj et al.*, 2002]. This further confirms that Geotail was likely situated in the CPS.

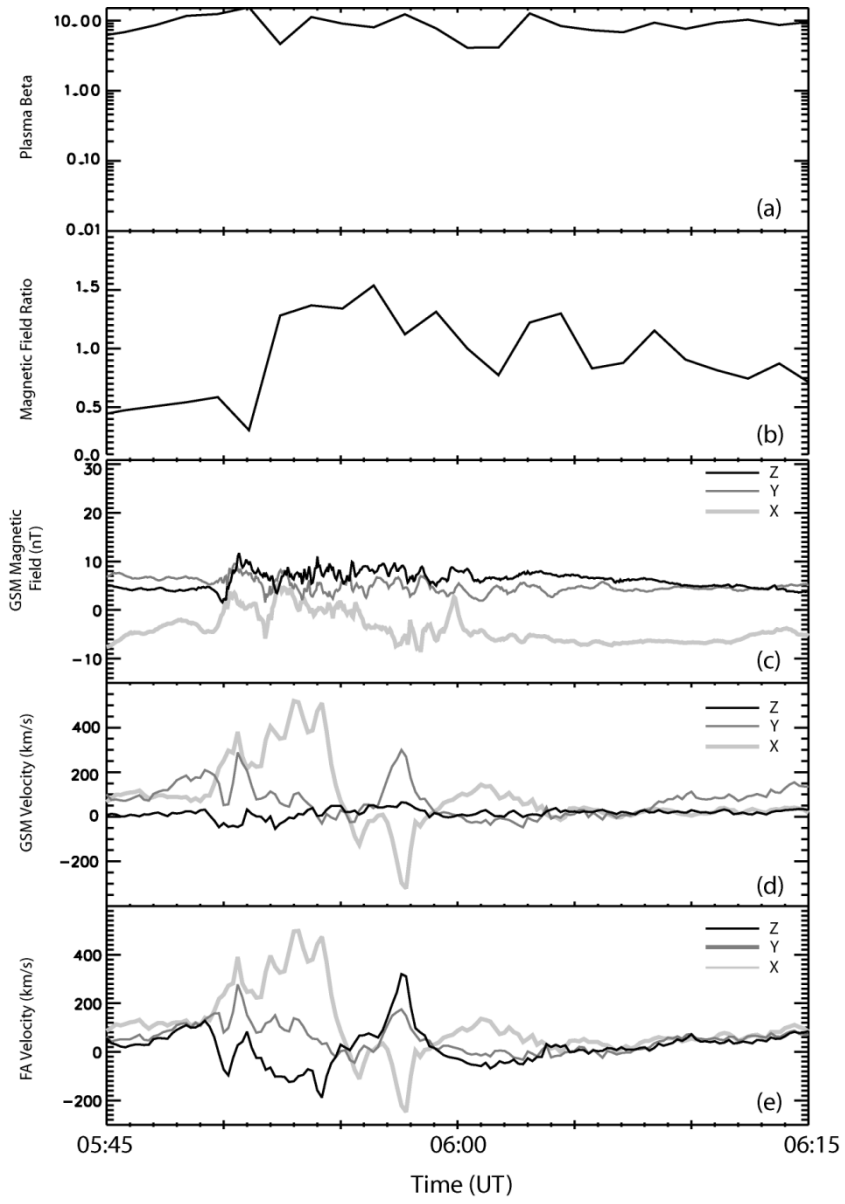

Figure 6.2: In-situ and derived observations from Geotail for the period 0545-0615 UT. (a) Ion-plasma beta observed during the BBF. (b) The magnetic field ratio, the ratio of B_z to vector sum of B_x and B_y. (c) The GSM vector magnetic field. (d) The GSM plasma velocity and (e) plasma velocity in a field-aligned (FA) coordinate system. See text for details.

6.2.2 Ground-based Observations

For the duration of the BBF, Geotail lies slightly to the west of the "Churchill line" of magnetometers (~265 degrees geographic longitude), closely conjugate to the GILL and RABB magnetometers at geographic latitude of 56.38, and 58.22 degrees, respectively (Figure 6.1 (a) and Chapter 3 Table 3.1-Table 3.6). For brevity, Figure 6.3 shows the H-component of the magnetic field at the auroral- and mid-latitude Churchill line magnetometers; FCHU, GILL, ISLL, and PINA; the stations RABB and FSMI; and the low-latitude LNL magnetometer. These stations are those recording the largest bay structure, and in closest conjunction with the Geotail satellite during the BBF interval and hence those most likely to observe the IC and directly driven compressional Pi2s. The bottom panel of Figure 6.3, (h), displays the $v_{\perp x}$ plasma flow measured by the LEP instrument at Geotail. Large amplitude magnetic deflections are observed at L≈6.5 (FCHU, GILL, RABB and FSMI), the largest bay being observed at FCHU (~120 nT). Though FCHU observes the largest H-component magnetic bay structure, the formation of the bay occurs much later than the observed BBF. Conversely, the magnetic bays observed at GILL, RABB and FSMI begin to form at about ~0545 UT, roughly 4 minutes before the BBF is observed at Geotail.

6.2.3 Frequency Content of the Pi2-BBF Waveforms

Figure 6.4 shows the bandpass filtered (40-200 s) H-component for selected CARISMA magnetometers, the LNL magnetometer (panels a-f), and the $v_{\perp x}$ plasma velocity (panel g). The largest amplitude Pi2 is observed at GILL, and Pi2s are evident at all of the remaining five stations, closely coincident with the BBF. In the filtered time-series the BBF shows 6 FBs (Figure 6.4 g); however the last two FBs are due to a flow reversal at the end of the BBF, a result of the data processing, and are hence not FBs which can be associated with Pi2 impulses in the Kepko model, thus we do not discuss these flow bursts in detail. Both GILL and ISLL observe a similar Pi2 wavepacket, while RABB and FSMI observe Pi2 waveforms with a similar number of amplitude peaks as the FBs within the BBF. The low latitude LNL magnetometer observes the smallest amplitude Pi2 (~0.5 nT), though the waveform at this station has a remarkable similarity to the waveform of the observed FBs within the BBF. Further the Pi2s and BBF are observed almost contemporaneously, at ~0549 UT. Note however, that both the observed Pi2s and the BBF follow the formation of the initial current system at ~0545 UT, c.f. Figure 6.3.

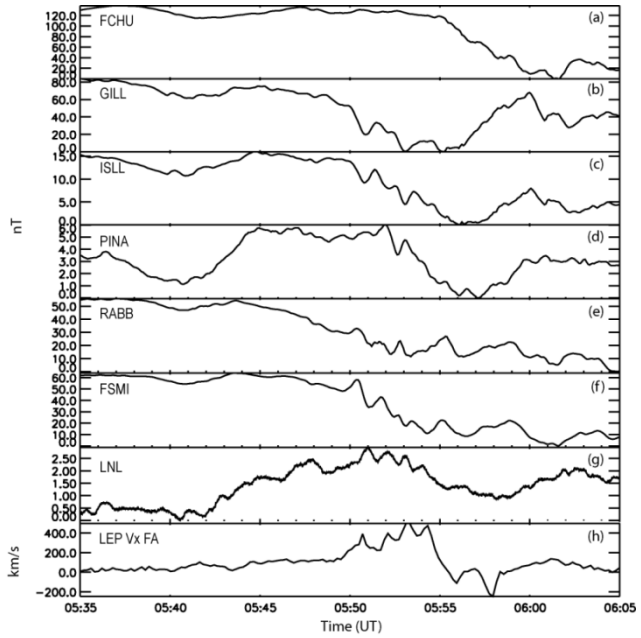

Figure 6.3: A stack plot of the H-component magnetic field for selected CARISMA magnetometers and the Los Alamos (LNL) magnetometer, panels (a-g), and the $v_{\perp x}$ plasma flow observed by Geotail, panel (h), between 0535-0605 UT.

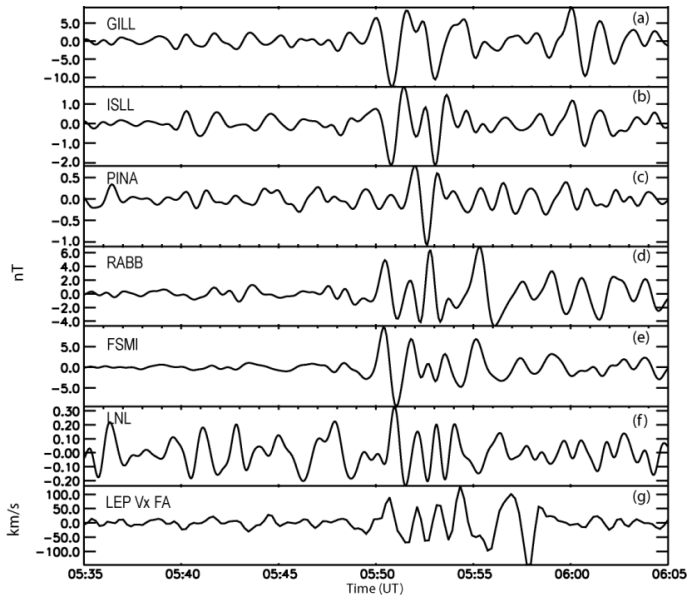

Figure 6.4: The bandpass filtered (40-200 seconds) H-component magnetic field for selected CARISMA magnetometers, panels (a-e), the LNL magnetometer (f), and $v_{\perp x}$ plasma flow, panel (g).

A fundamental aspect of the directly-driven model proposed by Kepko and Kivelson [1999] and Kepko et al. [2001] is the one-to-one correlation between BBF FBs and cycles within Pi2 waveforms. This suggests that both the waveforms and dominant frequency content of the observed BBF and Pi2 should match. Figure 6.5 shows the Fourier power spectra of the H-component of the CARISMA magnetometers (a-e), LNL magnetometer (f) and the $v_{\perp x}$ plasma flow (g) derived from the time-series shown in Figure 6.4. The BBF shows discrete frequency peaks at ~7, ~12, and ~16 mHz, however only the 12 and 16 mHz peaks are associated with the temporal spacing of FBs within the BBF (shaded region of Figure 6.5). The 7 mHz peak is a consequence of the end of the BBF and the flow reversal mentioned previously. Thus we concentrate on the 12 and 16 mHz peaks in the frequency range 11-17 mHz when comparing the power distributions of the BBF and the Pi2 waveforms observed on the ground.

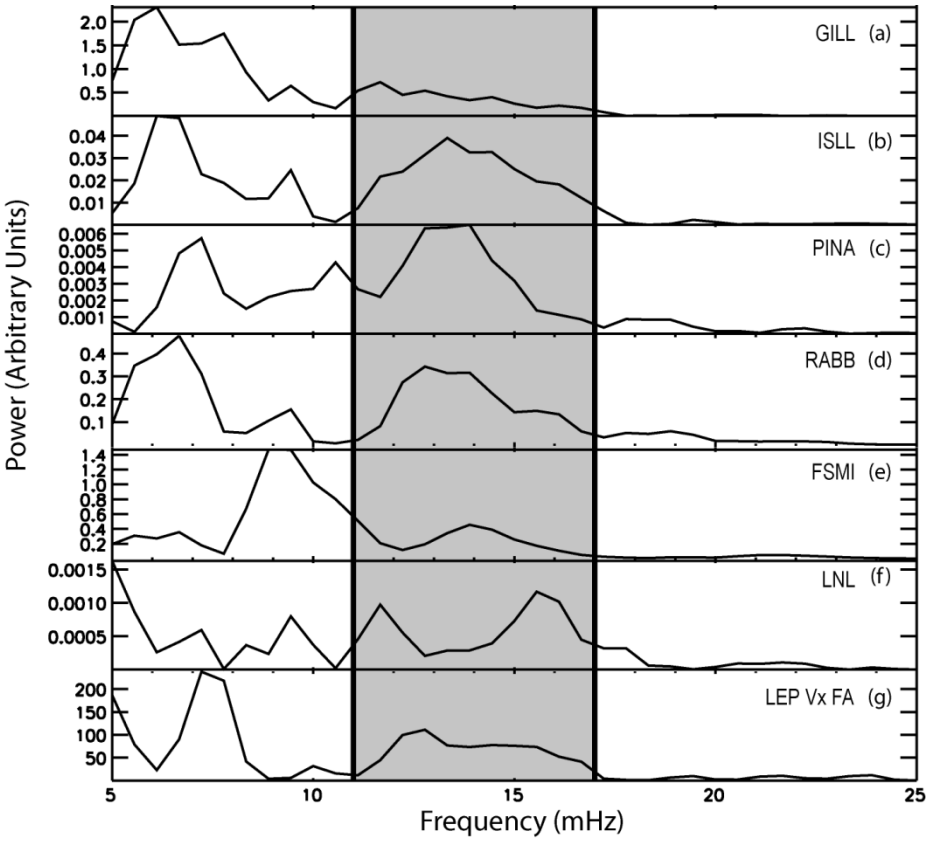

Figure 6.5: The power spectra of the filtered time-series shown in Figure 6.4 (arbitrary units). The grey section highlights the frequencies present in the BBF, between 11-17 mHz.

Figure 6.6 shows the coherence spectrum between each of the magnetometers and the $v_{\perp x}$ plasma velocity (panels (a)-(f)). For reference the bottom panel, (f), shows the power spectra of the BBF (same as the bottom panel of Figure 6.5). The coherence spectrum provides an estimate of the correlation between two time-series by comparing the power spectra of both series. Evident in Figure 6.5 are the similarities between the power spectra of the magnetometers and the BBF, while Figure 6.6 shows that over the duration of the flow peaks in the coherence exist between the Pi2 observed at each magnetometer station and the BBF. It is important to note that coherence is most significant at frequencies where there exists power, thus we consider only the peaks in coherence between 11-17 mHz, spanning the frequency content of FBs within the BBF (shaded region).

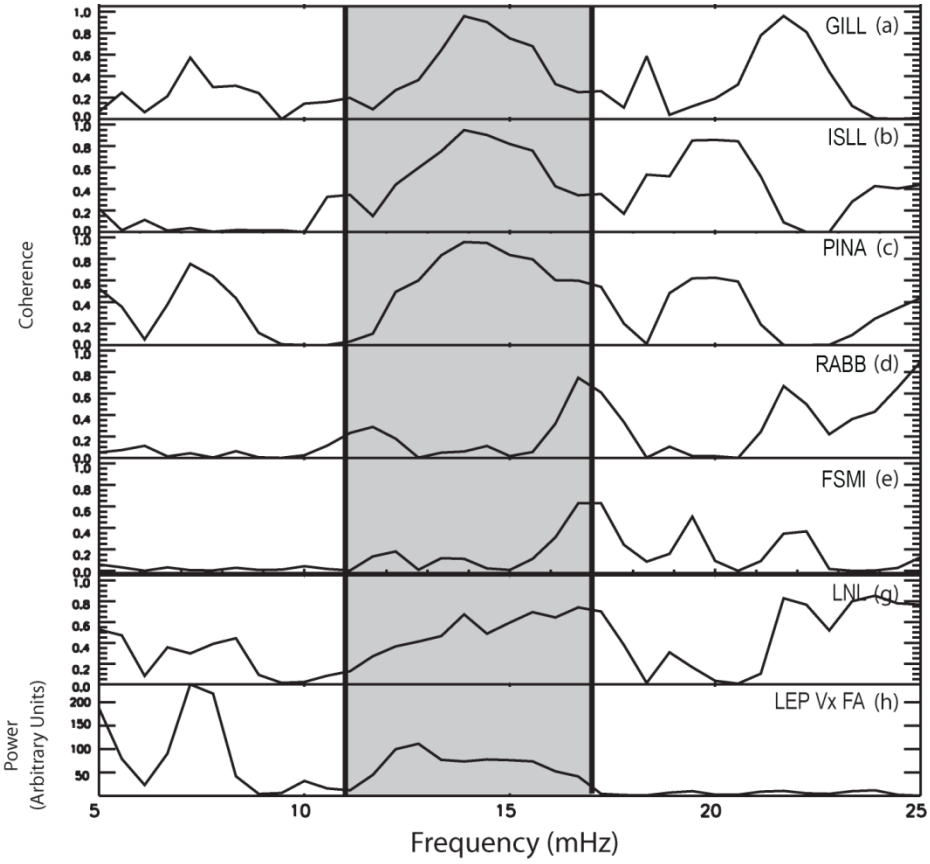

Figure 6.6: Panels (a-f) show the coherence spectra between individual magnetometer stations and the LEP $v_{\perp x}$ plasma velocity observed by the Geotail spacecraft. Panel (f) shows the BBF power spectra (same as Figure 6.5 f), for comparison to the coherence spectra. Similar to Figure 6.5, the grey section highlights the frequency of FBs in the BBF, 11-17 mHz.

6.2.4 Temporal Causality of the Pi2-BBF Waveforms

Although the high coherence between the Pi2s observed at each magnetometer station and the $v_{\perp x}$ plasma flow suggests that the observed wavepackets are similar in frequency content, it does not address the temporal causality between the flow and the ground ULF waves. In the directly-driven model, a BBF propagating in the magnetotail should be observed prior to Pi2 waveforms on the ground. As such a dynamic power spectrum should show the development of power in $v_{\perp x}$ prior to the development of power in the Pi2 frequency band at each magnetometer station. By comparing the normalized dynamic power spectrum from the magnetometer stations to that of $v_{\perp x}$ we can determine whether oscillations in the 11-17 mHz range (the frequency of FBs within the BBF) are observed first on the ground or in the magnetotail.

The dynamic power spectrum for both the magnetometers and the LEP $v_{\perp x}$ plasma flow is determined for an entire day using a 10 minute FFT window, approximately twice the temporal length of the BBF, with a 1 minute step size, approximately the frequency of the FBs. The normalized dynamic power spectrum of the $v_{\perp x}$ plasma is then subtracted from the normalized dynamic power spectrum from each magnetometer. The resulting differenced power is plotted, corresponding to a "dynamic difference power spectrum". If the BBF drives the Pi2 we expect in each difference plot to first observe a minimum in the spectra (blue) corresponding to a time where the BBF power dominates, followed by a maximum (red) where power from the Pi2 waveforms observed by ground-based magnetometers dominates over the BBF. Figure 6.7 shows the "dynamic difference power spectra" for the CARISMA (GILL, ISLL, PINA, RABB and FSMI) and LNL magnetometers between 0530-0615 UT. The opposite of what is expected in the directly-driven model in the frequency range of study (11 – 17 mHz, grey box) is seen in Figure 6.7. That is, power is observed first at the magnetometer stations (GILL, ISLL, PINA, RABB, FSMI and LNL - red), and only later does power from the BBF, $v_{\perp x}$, observed at Geotail dominate (blue). Consequently the data show that the Pi2 power is seen on the ground in advance of being seen in $v_{\perp x}$ at Geotail in the plasmasheet.

Additionally, a lagged correlation between the BBF $v_{\perp x}$ and the observed ground Pi2 waveforms shows not only how similar the two waveforms are, but also shows the lag at which the similarity is the greatest. This further allows for the causality as well as the

hypothesised one-to-one relationship between FBs and Pi2 waveforms in the Kepko model to be tested. Figure 6.8 (a) shows the $v_{\perp x}$ plasma flow observed at the Geotail satellite filtered between 11-17 mHz. The highlighted area corresponds to the section of the BBF which is used to calculate the correlation between the FBs and Pi2 waveforms. The minimum and maximum lags considered in the analysis correspond to 2 minutes (10 time steps either way of t_0, 0549:12 UT), shifting the BBF either 2 minutes backward or forward of t_0, respectively. Figure 6.8, panels (b-g) show the Pi2 observed at each ground station (grey), also filtered between 11-17 mHz. Over-plotted (black) is the BBF $v_{\perp x}$ time-series, with a lag applied which generates the maximum squared correlation. Table 6.1 summarises the results of the lagged correlation. Note that a positive lag corresponds to the BBF occurring before the observation of ground Pi2s, and a negative lag suggests the Pi2 is observed before the BBF. Apparent in Figure 6.8 and Table 6.1 is that all magnetometer stations exhibit a high correlation with the BBF; however, the largest correlation occurs when the BBF is time-shifted backward (negative lag), violating the causality of the Kepko model.

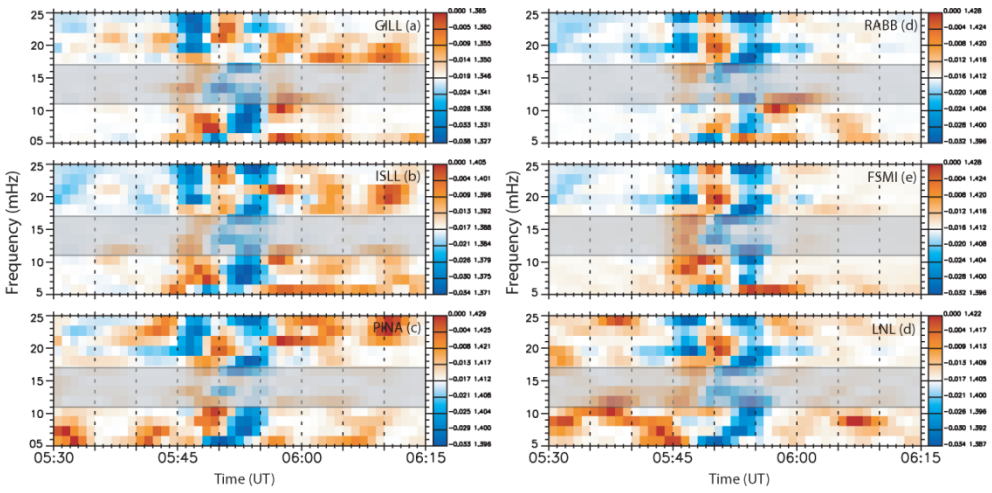

Figure 6.7: The dynamic difference spectra between the normalised power spectra in the H-component magnetic field at LNL, and at selected CARISMA and the LEP $v_{\perp x}$ plasma flow. The color bar depicts the difference between the power observed at a ground-based magnetometer and that observed in $v_{\perp x}$. Red indicates power from the magnetometer dominates, and blue shows that power in the LEP $v_{\perp x}$ plasma flow dominates and white shows similar power is observed in both the H-component magnetic field and $v_{\perp x}$ flow at Geotail. The grey band highlights the frequency band of interest, between 11-17 mHz.

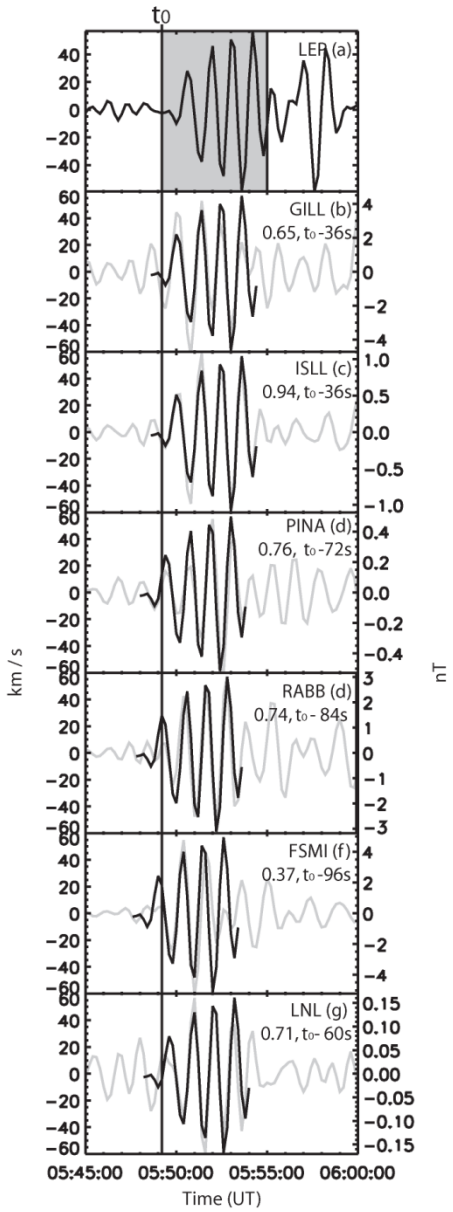

Figure 6.8: The top panel, (a), shows the $v_{\perp x}$ plasma flow bandpass filtered between 55-95s, approximately 11 and 17 mHz. The highlight depicts the section of the BBF which is used to calculate the BBF-Pi2 correlation coefficient; t_0 labels the beginning of the BBF, at 0549:12 UT. Panels (b-g) show the Pi2 observed at each magnetometer station (grey), and over plotted is the BBF (black), this having been time-shifted such that the correlation between the ground magnetic pulsations and FBs is maximized. Displayed in the upper right corner of panels (b-g) is the correlation coefficient squared and the amount the BBF is shifted relative to t_0, c.f., Table 6.1, e.g., 0.65, t_0-36s, in the case of the GILL magnetometer.

Table 6.1: Summarises the results at each magnetometer station for a maximum correlation lag with $v_{\perp x}$ at Geotail.

Magnetometer Station	Maximum Correlation Squared	Corresponding Lag of BBF from t_0 (0549:12 UT)	
		Time Pts	Seconds
GILL	0.65	-3	-36
ISLL	0.94	-3	-36
PINA	0.76	-6	-72
RABB	0.74	-7	-84
FSMI	0.37	-10	-96
LNL	0.71	-5	-60

Finally, the directly-driven model may also be suitably tested utilising a lagged regression analysis in Fourier space, also known as an impulse response function[*Shumway and Stoffer*, 2006], shown in equation (6.1).

$$y_t = \sum_{s=-\frac{-N}{2}}^{\frac{N}{2}-1} \beta_s x_{t-s} + \eta_t \tag{6.1}$$

The impulse response function utilises the Fourier spectrum of two signals, x_t and y_t, to estimate a set of filter coefficients relating the two variables. Specifically, the impulse response method estimates the β_s coefficients in equation (6.1), where y_t and x_t are two discrete signals and η_t is a stationary noise process (e.g., a Gaussian distributed random signal), N is the number of points in each time-series, t is the time and s is the lag between the two signals at time t. The filter coefficients β_s are estimated from the power spectrum of x and the cross-power of x and y. Details on the estimation and calculation of each β_s can be found in Shumway and Stoffer [2006].

There are two important properties of the impulse response function to note: If s is a positive integer, then y_t is a function of a series of past values of x_t. If s is a negative value, then y_t can be written in terms of future x values (or x_t is a function of past values of y_t). By convention y_t is forced to be a function of the past values of x_t by considering only the coefficients of β_s where $s \geq 0$ and which satisfy the condition:

$$|\beta_{s\geq 0}| = \max(|\beta_{s<0}|) \tag{6.2}$$

The second property of the impulse response function is that equation (6.1) may be reversed and x_t may be written as a function of y_t. In general one calculates both sets of β_s ($\beta_{s,\,y(x)}$ and $\beta_{s,x\,(y)}$) and determines the most likely relation between the observed variables. Ideally, one set of β_s will not satisfy equation (6.2) and the proper temporal dependence between x and y may be determined. Alternatively, neither sets of β_s will satisfy (6.2) suggesting the variables are not causally related and are therefore independent, however similar their time-series appear to be. Finally, both sets of β_s can satisfy (6.2) implying that there may be additional variables in the system relating x and y which have not been considered.

The impulse response function is therefore ideal to test the BBF-Pi2 relation as it directly relates the observed BBF to the Pi2 in a functional form. In the directly-driven model, we expect to be able to write each magnetometer station (y_t) as a function of the BBF (x_t). In our analysis we also consider the scenario where the BBF is a function of the Pi2 observed by the magnetometers. Though this is not physically plausible, it allows us to further test the temporal causality of the model. Further, if the BBF $v_{\perp x}$ time-series can be written as a function of the observed Pi2 signal this suggests that another physical process may exist which is driving both the Pi2 and BBF.

Figure 6.9 summarises the results from the impulse response analysis between the H-component magnetic field observed at the FSMI magnetometer and the $v_{\perp x}$ plasma velocity. Both datasets have been bandpass filtered in the frequency range of the BBF (55-95s, ~11-17 mHz); these bandpass signals are shown in the top panel of Figure 6.9. The bottom two panels, (b) and (c), display the β_s coefficients as a function of the lag s. The horizontal lines denote the maximum value of $|\beta_s|$ where s<0, and the vertical lines represent the value of β at each s. The red vertical lines depict those values β_s which satisfy equation (6.2). Figure 6.9 (b) shows the filter coefficients when the $v_{\perp x}$ plasma flow is considered as a possible function of the Pi2 time-series observed at FSMI. Evident in panel (b) is that the coefficients at lags s=0, 1, 2, 3, and 8 rise above the threshold and satisfy equation (6.2). Figure 6.9 (c) shows the filter coefficients when the Pi2 observed at FSMI is considered as a function of the $v_{\perp x}$ plasma flow observed at

Geotail. Evident in Figure 6.9 (c) is that none of the coefficients satisfy equation (6.2). Table 6.2 summarises the results from the impulse response function for the Pi2s observed at the five remaining magnetometer stations. These results indicate that the FB in $v_{\perp x}$ are likely not the cause of the Pi2s observed on the ground (panel (c)). However, the fact the FB $v_{\perp x}$ can be written as a lagged function of the FSMI H-component magnetometer data, panel (b), suggest that the time-series are related, perhaps by a common driver.

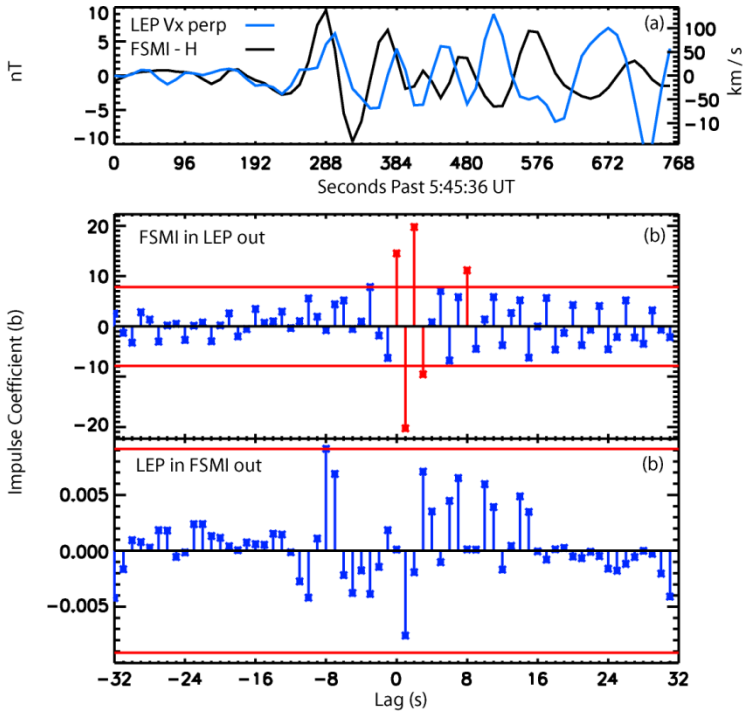

Figure 6.9: Panel (a), shows time-series of the Pi2 observed at FSMI (black) in nT (left axis), and of the BBF (blue) in km/s (right axis). These are the data sets utilised in the impulse response function. Panels (b) and (c) depict the results from the impulse response function, (b) BBF $v_{\perp x}$ as a function of the Pi2 waveform at FSMI and (c) the Pi2 waveform at FSMI as a function the BBF $v_{\perp x}$. The y-axis is the value of the filter coefficient, β_s, as a function of the lag, s, on the x-axis. The horizontal lines represent the threshold defined in equation (6.2) and the red vertical lines represent the β_s coefficients lying above the threshold.

Table 6.2: Summarises the results from impulse response function analysis between each of the individual magnetometer H-component time-series and the observed BBF $v_{\perp x}$.

Magnetometer Station	Number of β_s coefficients satisfying equation (6.2)	
	Pi2 (y_t) as a function of the observed BBF (x_t)	BBF (x_t) as a function of the observed Pi2 (y_t)
GILL	0	2
ISLL	0	2
PINA	5	0
RABB	0	3
FSMI	0	5
LNL	1	2

6.3 Discussion

In this Chapter we present results from a nightside conjunction between the Geotail spacecraft and the CARIMSA magnetometer array on 31st May 1998 during the development of a small and isolated night-side substorm-like event. Utilising observations of the plasma flow in the CPS from the Geotail-LEP instrument, and Pi2 waveforms from the CARISMA magnetometer array and from the LNL magnetometer, we investigate the relationship between quasi-periodic FBs within a BBF and Pi2 waveforms observed on the ground.

In their model Kepko and Kivelson [1999] and Kepko et al. [2001], propose that an earthward propagating BBF could be decelerated in the plasmasheet in the transition region between dipole- and tail-like magnetic field orientations. They proposed that the deceleration of FBs within the BBF could generate a fast-mode wave which directly drives Pi2 oscillations at lower- and mid-latitudes on the dawn and dusk flanks. At higher latitudes, these authors propose that the deceleration of individual FBs could generate a FAC which drives oscillations of the magnetic field at the frequency of the FBs; these oscillations being termed the inertial current (IC) Pi2 [*Kepko et al.*, 2001]. Kepko et al. [2001] have also suggested that during periods of quiet geomagnetic activity the conductivity of the ionosphere could be sufficiently low that there is little reflection of the Alfvén wave responsible for generating Pi2s observed on the ground, and hence that the TR mechanism [*Olson*, 1999] could be circumvented. Indeed the magnetic bays during this event begin to form before the observation of the BBF (Figure 6.3). During

this time, the Pi2s typically associated with the formation of the SCW are not observed. This suggests that either the TR Pi2s are damped or the TR mechanism is completely circumvented due to low conductivity of the ionosphere. Further, the geosynchronous magnetic field observed at GOES-8 (not shown) is approximately dipolar, while the magnetic field at GEOTAIL (at radial distance ~13 R_E) is highly stretched with a magnitude of ~10 nT. From this we infer that the flows observed at Geotail have not yet been decelerated since they are observed outside the likely region of flow braking [*Shiokawa et al.*, 1997]. Thus in this case study, if the Kepko model is correct, the Pi2s should resemble that of an IC Pi2. They should also be directly driven by the FBs and hence the Pi2 waveform on the ground should be observed following the observation of the BBF FBs at Geotail.

The one-to-one correlation predicted by the Kepko directly-driven model also implies that the frequency spectrum of the BBF should match that of the Pi2s. Similarly we should observe a peak in the coherence spectrum over the range of frequencies present in the BBF, providing further evidence that the waveforms present in both the BBF $v_{\perp x}$ and ground Pi2 waveforms are similar. As seen in Figure 5, each magnetometer power spectra and the $v_{\perp x}$ plasma flow power spectra are similar over the frequency range of FBs in the BBF, between 11-17 mHz. These spectra have similar power distributions and peaks in power over the 11-17 mHz. The coherence of the observed Pi2 waveforms at the individual magnetometer stations and the BBF $v_{\perp x}$ also peak in the frequency range of the BBF as shown in Figure 6.6. The coherence at, GILL, ISLL, and PINA have broad peaks at ~14 mHz, coincident with the $v_{\perp x}$ spectral peak at Geotail. RABB and FSMI peak twice within the 11-17 mHz range, at ~12 and ~16.5 mHz. LNL also shows strong coherence between 11-17 mHz. The similarities between the H-component magnetometer power spectra and that of the $v_{\perp x}$ plasma flow at Geotail, as well as the peaks in the coherence spectra, clearly shows that the Pi2 waveforms resemble the FB structure within the BBF.

The impulse response function, “dynamic difference power spectra” and lagged correlation provide a more rigorous test to scrutinise both the one-to-one correlation as well as the temporal causality of the BBF-Pi2 relation. The BBF appears to be observed at Geotail outside the region of deceleration, thus the BBF and FBs should be observed

before the ground Pi2s. Figure 6.7 shows the temporal development of power in the Pi2 frequency range, in the ground Pi2s and $v_{\perp x}$, and Figure 6.8 shows the best lagged correlation between the observed Pi2s and the BBF $v_{\perp x}$ (summarised in Table 6.1). Table 6.2 summarises the results from of the impulse response analysis between the BBF and Pi2s. All of these results are consistent with a scenario where, in the BBF frequency range, the spectral power develops first on the ground and subsequently in the waveform of $v_{\perp x}$ in the flow. The correlation is maximised at each magnetometer when the BBF is shifted backward in time, and the impulse response function shows that at all stations, except PINA and LNL, that the BBF $v_{\perp x}$ waveform can be described in terms of ground Pi2s. The converse is not true, casting doubt on the hypothesis that the waveform of the FB $v_{\perp x}$ directly drives the Pi2 waveform seen on the ground.

In the Kepko model we expect the waveform of the FBs within the BBF to consistently occur before the conjugate Pi2 pulsations, and further the Pi2 wavetrain should be dependent on the $v_{\perp x}$ structure within the BBF. This is clearly not the case, since at four of the six stations (GILL, ISLL, RABB, and FSMI) power is observed first at the ground stations and subsequently by Geotail in $v_{\perp x}$. Similarly, at each of these stations the BBF and Pi2 are correlated best when the BBF $v_{\perp x}$ time-series is shifted backward in time, and finally, the impulse response function estimates the BBF $v_{\perp x}$ waveform to be dependent on the observed H-component Pi2 waveform observed on the ground. This clearly demonstrates that the temporal causality of the Kepko model is inconsistent with the observations on this day.

While four of the magnetometers clearly violate the causality of the Kepko model, PINA and LNL show apparent contradictory results between the impulse response analysis and the results from dynamic difference spectra and lagged correlation. Both PINA and LNL show some evidence that their Pi2s can be written as a function of the BBF $v_{\perp x}$ FB structure. Indeed, the Pi2 at LNL can be described as both the dependent (y_t) and independent (x_t) variable described by equation (6.1), suggesting that the BBF and Pi2 may indeed be related via additional variables not considered in the impulse response analysis. However, the dynamic difference power spectra at both PINA and LNL show the development of Pi2 power prior to the observation of BBF power in the 11-17 mHz band. Similarly, the Pi2 at both LNL and PINA is best correlated with the $v_{\perp x}$ plasma flow

when $v_{\perp x}$ is shifted 60 s and 72 s backward in time, respectively, violating the causality of a FB $v_{\perp x}$ driver. This is further discussed below, where we propose a model which can explain the similarities between the FB structure within a BBF and ground Pi2s and which is consistent not only with our observations, but also with those of Kepko and Kivelson [1999] and Kepko et al. [2001] as well.

It is clear that the frequency, occurrence and structure of the BBF FBs and the Pi2 waveforms observed on the ground are very similar, suggesting that while BBFs may not directly drive Pi2s the two phenomena may still be intimately connected. We propose that either bursty/non-steady reconnection in the tail or the coupling of a compressional disturbance with the plasma flows accelerated by reconnection provide a mechanism by which to modulate both the Pi2 waveforms observed on the ground and FB structure within a BBF at the same frequency. In the latter scenario a compressional disturbance could be launched following reconnection at the near-Earth neutral line (NENL). This compressional disturbance propagates almost isotropically away from the NENL potentially coupling to both the magnetotail waveguide [*Allan and Wright*, 1998] and the CPS. As the fast-mode (compressional disturbance) continues to propagate along the magnetotail waveguide it couples to the background magnetic field as an Alfvén wave which propagates down the field and which could be observed as a Pi2 by ground-based instrumentation [see for instance, *Chi et al.*, 2001; *Tamao*, 1964; *Uozumi et al.*, 2000]. Furthermore the coupling of the fast-mode and the CPS could potentially generate the FB structure observed in the BBFs accelerated during reconnection.

Alternatively, bursty reconnection, potentially driven by an irregular inflow of ions into the NENL reconnection region, could produce both a propagating compressional disturbance as well as a bulk plasma flow burst. Each subsequent 'burst' of reconnection could in turn generate an additional compressional disturbance and plasma flow. This could result in a periodic structure being observed in both the bulk plasma flow, i.e. FBs, and in a series of travelling compressional disturbances. As the compressional disturbance, propagate toward the Earth, they could it in turn couple to the background magnetic field creating the Alfvénic Pi2s observed by ground-based magnetometers [c.f. the Tamao travel time concept, *Tamao*, 1964].

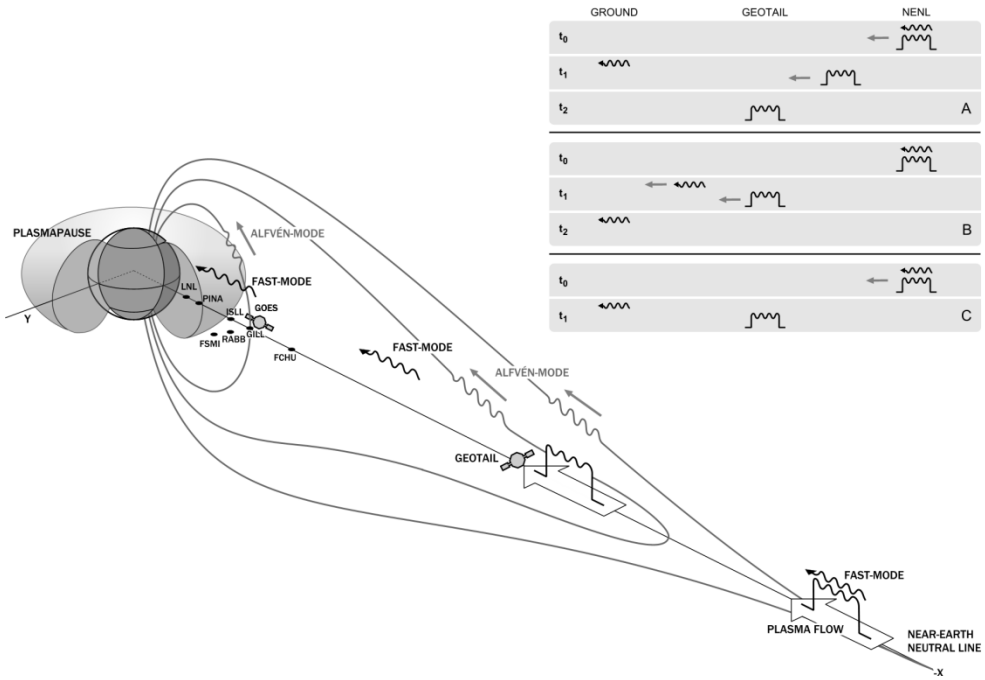

Figure 6.10: An illustration depicting a potential sequence of events subsequent to reconnection at the NENL. Reconnection at the NENL results in the release of a BBF, and the production of an earthward propagating fast-mode which couples to the background field generating Pi2 pulsations observed on the ground. The inset panels (a-c) show three possible time lines, for $t_0 \rightarrow t_1 \rightarrow t_2$ of the relative times of observing a Pi2 pulsation on the ground and the in-situ observation of a BBF in the CPS. See text for details. Image courtesy of Andy Kale.

In each of the above scenarios the individual BBF FBs and fast-mode fronts could have the same temporal spacing perhaps accounting for the high correlation between ground-based Pi2 waveforms and the series of FBs within a BBF. Moreover the travel time of the BBF and fast-mode is dependent on magnetospheric conditions (plasma density and magnetic field strength), and the fast-mode wave may travel at a group velocity faster than the observed BBF, or vice-versa. At mid- to high-latitudes if the fast-mode group velocity is larger than the BBF flow speed in the CPS it is possible that Pi2s could be observed on the ground before the BBF is observed in the magnetotail. This is consistent with the observation of Pi2 wavepackets at GILL, ISLL, RABB and FSMI ahead of Geotail $v_{\perp x}$, during our event. Conversely if the flow velocity exceeds the fast-mode group velocity, the BBF could be observed prior to the ground Pi2s, which is more consistent with the findings of Kepko and Kivelson [1999] and Kepko et al. [2001] who observed much greater BBF flow speeds than reported here. At low-latitudes (inside the plasmapause) the increase in density results in a decrease in both the fast-mode and

Alfvén velocities, as well as an increase in the travel time from the initial tail source region to the ionosphere [e.g., *Chi et al.*, 2001; and *Uozumi et al.*, 2000]. Thus at lower-latitudes, mapping close to and inside the plasmapause, it is possible for the ground Pi2s to be observed before, coincident with, or following the observation of the BBF flow in the tail. This would be consistent with waveform timings observed at PINA and LNL during the interval presented herein. Figure 6.10 is a pictorial representation of the two mechanisms described above. The different propagation paths of the modulated signals are depicted in the inset panels (a-c) of Figure 6.10. In case (a), the Pi2 is seen on the ground before the BBF FBs arrives at Geotail in the CPS; in case (b) the BBF FBs arrives at Geotail before the Pi2 is seen on the ground; and in case (c) the BBF FBs and the ground Pi2 are seen at the same time.

Typical Alfvén velocities in the inner magnetosphere are between ~4800 km/s outside of the plasmapause [e.g., *Burton and Russell*, 1970] and ~490 km/s inside the plasmapause. Further down the tail, the Alfvén velocity can be much more variable; during the interval of the BBF the derived Alfvén velocity in the CPS was ~450 km/s whilst the Alfvén velocity in the distant tail and lobes can often exceed 1000 km/s [e.g., *Burton and Russell*, 1970]. These velocities are consistent with the observations and as well the proposed BBF-Pi2 coupling mechanisms presented herein. Initially, the fast-mode may have had a group velocity similar to that of the BBF. As the fast-mode propagates toward the Earth the magnetic field strength increases resulting in an increase of the fast-mode velocity. Assuming that the BBF and fast-mode are generated concurrently and that the BBF velocity remains either constant or is decelerated, then at higher latitudes the Pi2 generated from the coupling of the fast-mode with the background magnetic field may be observed before the BBF in the mid-tail. At lower latitudes where the fast-mode and Alfvén velocities decrease, it is possible that the observation of the BBF and Pi2 are more closely coincident in time. Note, it is important to consider the group velocity of the fast-mode wave propagating in either the CPS or in the tail waveguide and further that the fast-mode wave energy may leak along the boundaries of the magnetotail waveguide thus making it difficult to observe any in-situ signature of the fast-mode wave [see e.g., *Allan and Wright*, 2000 for details].

It is important to note that the model we have proposed to relate Pi2s and the periodic structure of high-speed plasma flows in the central plasmasheet is consistent with both the current disruption (CD) and NENL substorm paradigms. In the CD model, NENL reconnection, perhaps triggered by the arrival of a rarefaction wave follows the initial expansion phase of the substorm which is driven by plasma instabilities in the near-Earth plasmasheet [e.g., *Huba et al.*, 1977; *Lui et al.*, 1995; *Roux et al.*, 1991]. The formation of the SCW in this CD model begins prior to reconnection at the NENL, and the generation of earthward propagating flows and fast-mode waves. In the NENL substorm model, reconnection initiates the substorm expansion phase. Flows in the magnetotail propagate toward the Earth disrupting the cross-tail current and diverting it into the ionosphere forming the SCW. In this scenario fast-flows in the CPS and the fast-mode launched at reconnection are observed prior to the formation of the SCW. In the CD paradigm, the Pi2s described by our model should be observed following the formation of the SCW and the observation of TR Pi2s. Conversely in the NENL model, the formation of the SCW, observation of TR Pi2s, and the Pi2s generated by the flows or fast-mode waves produced by reconnection should occur almost simultaneously. This provides a verifiable time-line, during both substorm paradigms, with which to test our proposed model.

6.4 Conclusions

Recent work by Kepko and Kivelson [1999] and Kepko et al. [2001] has shown that there is a high correlation between Pi2 pulsations observed during substorms and the internal FB structure of BBFs. These authors have suggested that the deceleration of FBs, intermittent peaks in flow velocity within a BBF, directly drive ground Pi2 pulsations. In their proposed model there is a one-to-one correlation between the multiple FBs and Pi2 wavetrain oscillations observed on the ground. We present a nightside conjunction between the Geotail spacecraft and the CARISMA magnetometer array on 31 May 1998 (0400-0800 UT), during an isolated small amplitude night-side activation which may be characterised as a small substorm of pseudo-breakup. During the Geotail-CARISMA conjunction, small amplitude Pi2 waves are observed by the CARISMA magnetometers and a high-speed plasma flow, BBF, is observed at the Geotail satellite. If the Kepko model is valid we expect the Pi2 waveforms and BBF FBs to have similar frequency

content, strong coherence and for the relative timing to support a causal relationship between FBs in the BBF in the tail and the waveform of the Pi2 seen on the ground.

In this case study we found that the ground Pi2 waves have similar frequency content and are very well-correlated with the FBs observed within the BBF; however, the causality of the proposed model is violated since the ground Pi2s are observed before the BBF flow in the CPS. We propose that the observed BBF FBs and Pi2 waveforms are similar because they are driven by a common source. Following bursts of NENL reconnection, either the BBF flows themselves or the reconnection region may excite fast-mode waves which then propagate Earthward and excite the Pi2s seen on the ground. Depending on magnetospheric conditions, the ground Pi2 generated by the fast-mode could be observed before the BBF is seen in-situ in the CPS or vice-versa. Such a hypothesis could account for the observed sequence of events presented herein, and also for those presented by Kepko and Kivelson [1999] and Kepko et al. [2001].

More studies utilising multi-point ground and magnetospheric observations are required to fully determine the extent of the BBF-Pi2 relation during pseudo-breakups and magnetic substorms. The Time History of Events and Macroscale Interactions During Substorm (THEMIS) [*Angelopoulos*, 2008]mission allows for a more extensive study of substorms and the sequence of events observed during expansion phase onset. Such measurements, using extensive ground observations from both magnetometers and all sky cameras as well as multi-point THEMIS probe observations in the magnetosphere, can be used to further test the validity of the model proposed here.

Chapter 7 Statistical Analysis of ULF Power During Substorm Expansion Phase

7.1 Introduction

Pi1 and Pi2 ULF waves, observed during the substorm expansion phase and described in detail in Chapter 5 and Chapter 6, were first classified by Jacobs et al. [1964]. Jacobs et al. [1964] described Pi1 and Pi2 waves as a subclass of irregular and impulsive ULF waves (referred to as Pi pulsations) in period ranges of 1-40 s and 40-150 s, respectively. Jacobs et al. [1964] noted that Pi pulsations were closely related to upper atmospheric phenomena (i.e. the aurora) and disturbances of the Earth's magnetic field (i.e. substorms). These authors described Pi2 pulsations as the dominant Pi waveform observed during magnetic substorms, while Pi1 waves were observed to have significantly smaller amplitudes than the longer period Pi2 waves having periods which seldom exceeded ~20 s.

Heacock [1967] adopted a similar classification scheme as Jacobs et al. [1964], characterising irregular and impulsive pulsations as Pi waves. However, the Pi subgroups were classified by Heacock [1967] as continuous pulsations, PiC, and broadband pulsations, PiB. The PiC pulsations described by Heacock were quasi-monochromatic waves associated mainly with the auroral electrojets, were well correlated with formation of H-component magnetic bays on the ground and were observed over a wide range of local time sectors spanning the pre-midnight and dawn sectors. PiB pulsations were categorised as broadband localised pulsations observed predominantly in the midnight sector near the onset of a magnetic bay or substorm. These PiB and PiC pulsations were postulated to be either the ionospheric response to bursts of charged particles entering the Earth's upper atmosphere, or the response of the Earth's magnetic field to a disturbance in the distant magnetotail.

More recently, a more complicated and mixed scheme has been adopted, using aspects of both the Jacobs et al. [1964] and Heacock [1967] classification schemes to characterise the ULF waves observed in relation to magnetic substorms. Impulsive Pi waves observed during the onset of a magnetic substorm are can be classified as PiB

waves [e.g., *Bösinger et al.*, 1981; *Heacock*, 1967], Pi1 waves [e.g., *Jacobs et al.*, 1964; *Milling et al.*, 2008], Pi1B waves [e.g. *Lessard et al.*, 2006; *Posch et al.*, 2007], Pi1/2 waves [e.g., *Murphy et al.*, 2009; *Rae et al.*, 2009a; *Rae et al.*, 2009b] or Pi2 waves [e.g., *Kepko and Kivelson*, 1999; *Olson*, 1999]. In general Pi2 waves are believed to be FACs responsible for the establishment of the SCW [*Olson*, 1999], though there is evidence that Pi2 waves can be directly driven by plasma flows in the magnetotail [*Kepko and Kivelson*, 1999; *Kepko et al.*, 2001] and it has also been postulated that Pi2 pulsations may be the result of bursty reconnection or the trapping of fast-mode wave energy in the magnetotail wave guide (see Chapter 6). Pi1B and PiB pulsations are typically associated with the onset of magnetic substorms and are in general considered to have periods on the order of seconds [*Bösinger et al.*, 1981; *Posch et al.*, 2007]. Lysak [1988] suggested that these waves were the result of wave energy coupling to the ionospheric Alfvén resonator, while Lessard et al. [2006] has suggested that Pi1B waves are generated in the tail as a fast-mode or compressional disturbance and become more transverse as they propagate down to the ground. Moreover, recent work on substorm timing utilising ground-based observations of the development of small-scale auroral features and ULF waves has shown that Pi1/2 waves with periods between ~16-96s, spanning both the Pi1 and Pi2 period bands, play an important role in identifying the initial expansion of magnetic substorms in the ionosphere [*Rae et al.*, 2009a; *Rae et al.*, 2009b]. Understanding whether differences or similarities exist between the different classifications of Pi pulsations is important for understanding the physical processes generating impulsive pulsations of different classifications and for understanding the coupling of the ionosphere and magnetosphere during magnetic substorms.

In this Chapter a statistical superposed epoch analysis of the ULF PSD spectra during the substorm expansion phase onset is presented to determine whether the different Pi1 and Pi2 bands of ULF waves are physically disparate phenomena, or whether the historical classification of ULF waves observed during magnetic substorms is in need of revision. In particular, we seek to establish whether Pi1 and Pi2 are both generated by the same physical process, and whether the Jacobs et al. [1964] or Heacock [1967] classification remains appropriate for distinguishing between ULF waves driven by different mechanisms during substorm expansion phase onset.

7.2 Methodology

Utilising both the CARISMA [*Mann et al.*, 2008] and CANMOS magnetometer arrays together with the IMAGE auroral substorm onsets in the Frey substorm database [*Frey et al.*, 2004; *Frey and Mende*, 2006], the ULF PSD spectra during the substorm expansion phase is characterised with respect to the location of the auroral brightening observed by the IMAGE satellite. The Frey substorm database identifies over 4000 substorms observed by the IMAGE-FUV camera between 16th May 2000 and 18th December 2005. Frey et al. [2004] and Frey and Mende [2006] categorised substorm onset in times by identifying the first FUV frame depicting the initial expansion and brightening of the aurora, the onset location being defined both geographically and geomagnetically (in latitude and longitude) by the brightest pixel in the onset frame. Recent work has shown that ULF power, specifically Pi1 wave power, rapidly decays away from the ionospheric location of substorm onset [*Posch et al.*, 2007]. Thus in order to adequately characterise the entire ULF spectrum a subset of the Frey substorms conjugate to the CARISMA and CANMOS magnetometer arrays is utilised. Conjugate substorms were identified as those lying between 220°-320° geographic longitude and occurring in approximately the midnight meridian (22-2 MLT). These criteria narrowed the Frey substorm database to 885 substorms spanning the interval from 20th May 2000-12th December 2005. The onset location of the 885 conjugate substorms identified in the Frey substorm database is illustrated in Figure 7.1 (purple asterisks) along with the geographic location of the CARISMA (red triangles) and CANMOS (red squares) magnetometers used in this study.

For each of the 885 substorms the geomagnetic latitudinal and longitudinal separation between the onset location and each of the available magnetometer stations with valid data (Figure 7.1) was calculated. The distance away from onset was calculated as the station geomagnetic latitude (longitude) minus the onset geomagnetic latitude (longitude) referred to as delta latitude or Δlat (delta longitude or $\Delta long$). A negative (positive) difference in geomagnetic latitude indicates that the station was south (north) of the auroral intensifications and a negative (positive) difference in geomagnetic longitude implies that the station was west (east) of the auroral intensification. The two-dimensional spatial distribution of stations with valid data with respect to distance in geomagnetic latitude and longitude away from auroral onset is shown in Figure 7.2,

where colour and numbers indicate the total number of events with valid magnetometer data within the given latitude and longitude bin. The latitude bins span 2° and longitude bins span 10° and the grid of event occurrence is centered with respect to the onset location, at (0,0) delta latitude, delta longitude. The densest distribution of magnetometers with valid data is located within approximately 85° west (delta longitude of -85°), 55° east (delta longitude of 55°) of the onset location. Latitudinally, Figure 7.2 shows a high concentration of stations with valid data between approximately 5° south of onset and 9° north of onset.

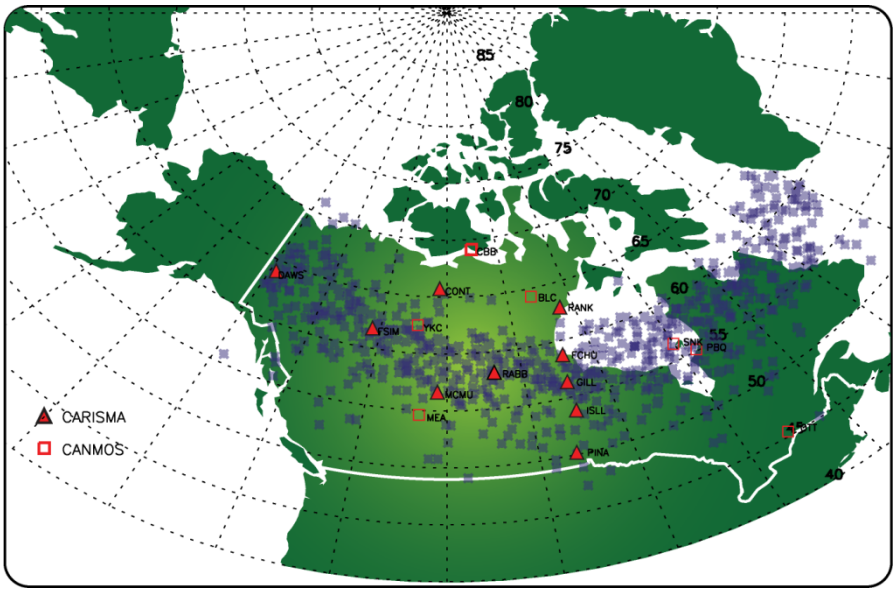

Figure 7.1: The location of the CARISMA and CANMOS magnetometer arrays. Over plotted in purple asterisk is the location of the subset of magnetic substorm identified in the Frey substorm database conjugate to the CARISMA and CANMOS magnetometers.

Typically, characterising whether a ULF wave is bursty or continuous in a statistical study is complicated since it requires an examination the waveform in the time domain. In general the properties of ULF waves are more easily quantified in a statistical study in the frequency domain. Thus we concentrate on characterising the spectral content of ULF waves observed during the time interval spanning substorm expansion phase onset. For each available magnetometer, the H and D PSD were calculated from a 40 minute time window centered on the onset time identified in the Frey substorm database.

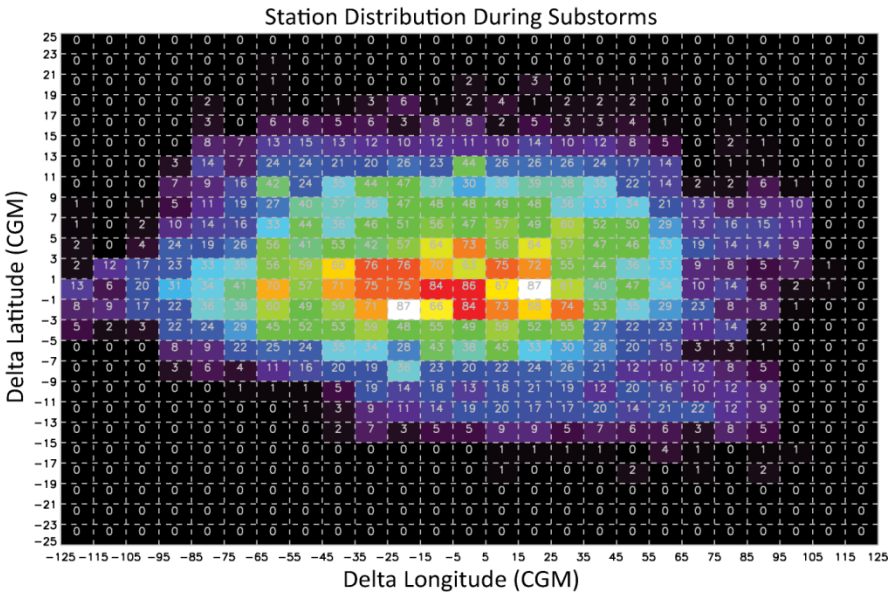

Figure 7.2: The two-dimensional distribution of magnetometer stations with respect to the distance in latitude and longitude of an individual station away from auroral onset. Negative indicates the station is west/south of auroral onset.

Prior to calculating the PSD, the mean was removed from the time series and the series was than highpass filtered (0-500 s) to remove the slowly varying background perturbation of the magnetic field as well as any bays resulting from the formation of the SCW in the ionosphere. Finally a Hanning window was applied to the time series and the PSD was calculated as defined in (3.10) using the appropriate winnowing correction. Note that any magnetometer time series with a data gap or erroneous values was not processed as the data was not considered valid for this statistical study. As shown in Chapter 5, ULF onset can precede the auroral onset defined in the Frey database by up to ~12 minutes. Consequently a 40 minute time series centered on the Frey onset time should ensure that the ULF waves observed during substorm expansion phase onset are encompassed by this window. For the 885 substorms, a total of 8109 valid PSD spectra were computed for both the H- and D-component magnetic fields. Together, the H- and D-component power spectra from each magnetometer, as well as the separation between the magnetometer and auroral onset locations, allowed the statistical characterisation of the spatial distribution of ULF PSD with relation to and during the substorm expansion phase onset.

With over 8000 spectra in both H and D and 240 spectral estimates in each spectrum, characterising the structure and features of the entire ULF spectrum can be difficult. Thus, only three bands of ULF PSD will be considered here and only in select cases will the complete PSD spectra be examined. The three bands considered are the Pi1 (10-40 s) and Pi2 (40-150 s) period bands as well as a band overlapping both the periods of Pi1 and Pi2 waves. As shown in Chapter 5 [also see, *Murphy et al.*, 2009; *Rae et al.*, 2009a; *Rae et al.*, 2009b], the ULF waves characterising the onset of a magnetic substorm are often observed first in the 24-96 s wavelet band, encompassing both the Pi1 and Pi2 periods. The 24-96 s period band, hereafter termed Pi1/2, is therefore the third ULF band which will be characterised in this Chapter. The PSD spectra are used to calculate the summed power in each of the three selected ULF bands allowing for a comparison between the characteristics of Pi1 power, Pi2 power and Pi1/2 power.

In this statistical study the spectra are binned based on the relative location of the station with respect to the Frey auroral intensification location (delta latitude and delta longitude, c.f. Figure 7.2). Power in the median and mean spectra, as well as the median and the mean summed spectra, will be considered in each of the three ULF bands. It is important to note that the CARISMA and CANMOS magnetometers are operated at different temporal cadences during intervals contained within the Frey database and hence in this study. Prior to the 5th April 2005, the CARISMA magnetometer array was operated as CANOPUS and the data was recorded at a 5 s cadence. Subsequent to the 5th April 2005, the primary data product from the CARISMA magnetometer array was upgraded to a 1 s cadence. For the duration of this study the CANMOS magnetometers all operated at a 1 s cadence. Due to the 5 s cadence of a subset of the CARISMA magnetometer data only part of the total 1 s PSDs are considered, specifically up to the Nyquist of a 5 s data set (10 s or 100 mHz). The 10 s Nyquist is within the period range of Pi1 waves. This is why when considering Pi1 waves in this study a 10-40 s period band is considered, rather than the historical 1-40 s period band.

7.3 Results

Figure 7.3 illustrates the two-dimensional spatial distribution of the log of the summed median spectrum in each of the three ULF bands as a function of delta latitude and delta longitude (c.f. Figure 7.2). For each of the spatial bins depicted in Figure 7.2 a median

power spectrum is calculated by determining the median value for each spectral estimate of PSD. The summed ULF spectra are then calculated for each of the Pi1, Pi1/2 and Pi2 bands by summing the median PSD spectra over the respective frequency (period) ranges. The color bar indicates the value of the summed median PSD in each spatial bin; green corresponding to a small power, blue medium and pink high. Apparent in Figure 7.3 is a clear localisation of summed median ULF power in all three of the ULF bands near the auroral onset region in both the H and D magnetic field components. Moving away from the location of the auroral onset, the ULF power rapidly fades, by approximately an order of magnitude, in both the H- and D-components. Moreover there is a consistent increase in the amplitude of the summed median PSD as the period of the ULF band increases. That is the Pi1 band exhibits the smallest amplitude summed median PSD, and the Pi2 band has the largest amplitude summed median PSD. The amplitude of the Pi1/2 PSD lies between that of the Pi1 and Pi2 bands. This is observed in both H- and D-component of the magnetic field. Also note that Figure 7.3 shows that the summed median PSD is typically larger in the H-component than in the D-component.

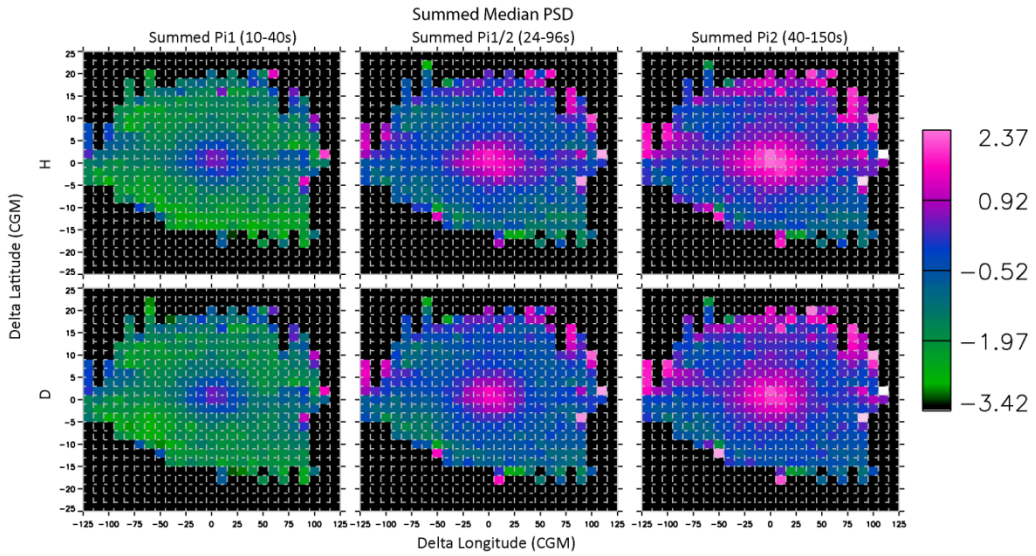

Figure 7.3: The spatial distribution of the logged summed median PSD. The median PSD value is determined for every spectral estimate. The summed median PSD is derived from the median value at each spectral estimate by summing over the required frequency range. The top row is the H-component PSD and the bottom the D-component. The left column depicts the summed Pi1 PSD, middle the Pi1/2 PSD and right the Pi2 PSD. The color bar on the right indicates the amplitude associated with color in figure.

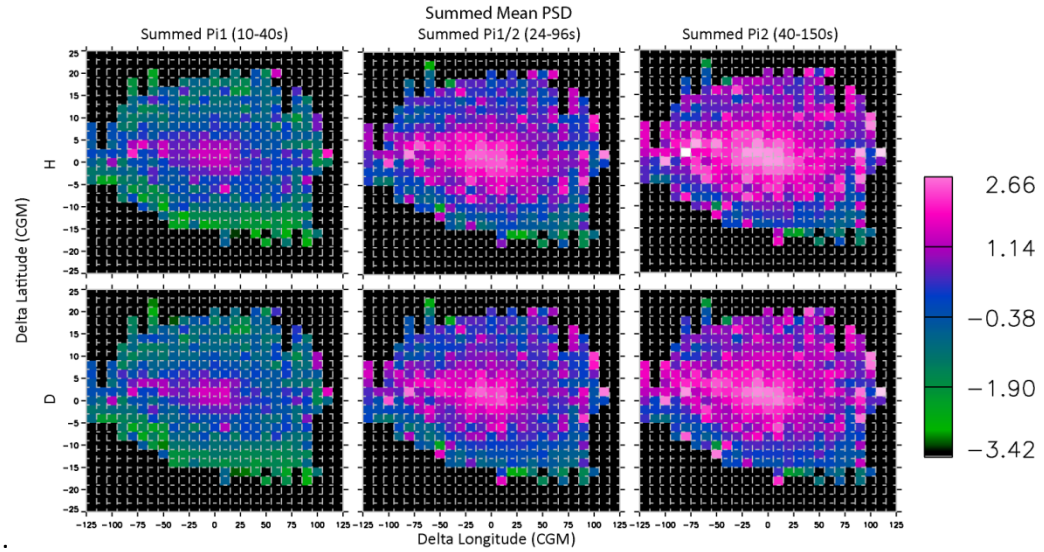

Figure 7.4: The spatial distribution of the logged summed mean power PSD. The figure is in the same format as Figure 7.3.

Figure 7.4 illustrates the distribution of the summed mean spectra. The spectra and summed PSDs are calculated in the same manner as used to create Figure 7.3 above, except that the mean value of PSD at each spectral estimate is used to derive the summed power in each frequency band rather than the median. Note that the amplitude of the summed mean PSD is in general larger than the amplitude of the summed median PSD (see the color scales of Figure 7.3 and Figure 7.4). This suggests that ULF power during expansion phase onset is non-uniformly distributed similar to a Poisson distribution where the mean of the distribution can be larger then median. Similar to Figure 7.3, the summed mean power in the H-component is in general larger than the summed mean power in the D-component. The summed mean ULF power in the long period Pi2 band is also larger than that in the shorter period Pi1/2 and Pi1 bands, similar to Figure 7.3. Moreover Figure 7.4 also depicts a clear localisation of the summed mean PSD in both H and D, and in all three ULF bands, near the auroral intensification. However unlike the summed median distribution there is also an additional localisation of ULF power west of the auroral intensification, along the latitude defining the location of the auroral bulge. The additional westward localisation of summed mean PSD is clearly depicted in the summed mean Pi1 PSD in both the H- and D-components. It is also observed in the Pi1/2 and Pi2 bands, although is not as clear as that of the Pi1 band due to the saturation of the color at high powers. The

westward expansion of summed mean ULF power appears visually to be spatially characteristic of the formation of the SCW and the development of the WTS during expansion phase onset.

Figure 7.3 and Figure 7.4 characterised the spatial distribution of summed mean and median ULF power as a function of the delta latitude and delta longitude in three frequency bands. In both the mean and median distributions, the ULF power appeared to be potentially concentrated in the longer period (shorter frequency) ULF bands, suggesting that there may be differences in the Pi1, Pi1/2 and Pi2 spectra. Figure 7.5 shows the mean, median, and upper and lower quartile power spectra from selected spatial bins in the vicinity of the auroral intensification for both the H and D magnetic field components. Evident in Figure 7.5 is that the mean, median and upper and lower quartile ULF spectra, in both the H and D components are characterised by a power law, that is a linear relation between the log of power (y-axis) and the log of the frequency (x-axis). All of the power spectra shown in Figure 7.5 are characterised by a slope of approximately -11/3. A random selection of a subset of the spatial bins shown in Figure 7.3 and Figure 7.4 indicates the ULF spectra are indicative of a power law with a characteristic slope between ~-3.2 and ~-3.6 encompassing the -11/3 power law observed near the auroral intensification. The statistical power law spectra are significant in that they clearly demonstrate that there is no break at 40 s period separating the Pi1 and Pi2 bands. Moreover there appears no statistically preferential frequency or frequency band during substorm expansion phase onset.

The power law distributions shown in Figure 7.5 also account for the differences in the amplitudes of the Pi1, Pi1/2 and Pi2 power as illustrated in Figure 7.3 and Figure 7.4. Figure 7.5 clearly shows that higher periods (lower frequencies) have more power then lower periods (higher frequency). Thus, unsurprisingly, the Pi2 band has more power than the Pi1/2 band which has more power than the Pi1 band. Moreover, and similar to Figure 7.3 and Figure 7.4, Figure 7.5 clearly shows that the amplitude of the mean PSD spectra is significantly larger than that of the median spectra and is of comparable amplitude to the upper quartile median spectrum. This suggests that during the substorm expansion phase the distribution of the number of events with specific ULF

power magnitude is non-uniform not only in the spatial domain, for instance the westward localisation of power in Figure 7.4, but also in the frequency domain.

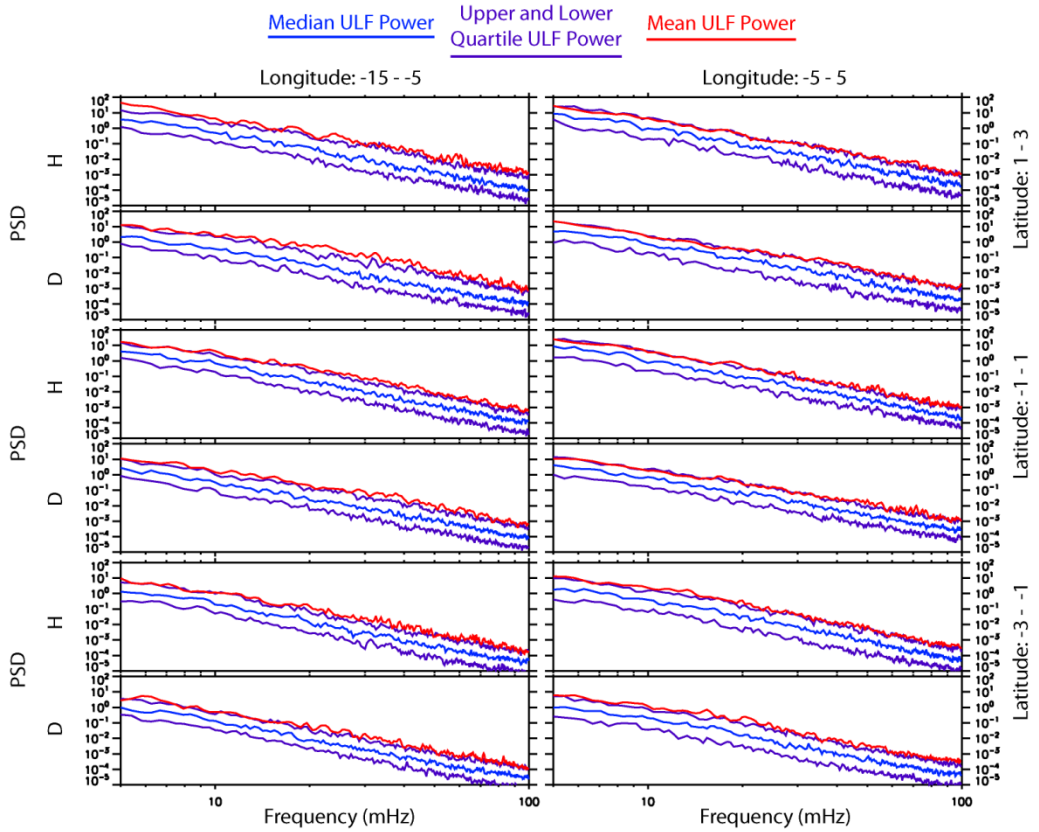

Figure 7.5: Mean (red), median (blue) and upper and lower quartile (purple) ULF PSD spectra for both the H and D magnetic component. The spectra are from select bins shown in Figure 7.1 near the auroral onset location. The title indicates the delta longitude bin and the y-axis title on the right indicates the respective delta latitude bin.

Whilst Figure 7.3 and Figure 7.4 characterise the median and mean ULF spectra observed during the substorm expansion phase, they provide no insight into a "typical" substorm event, since the mean and median power in adjacent spectral bins can come from totally different events. Figure 7.6 and Figure 7.7 are plotted in similar manner as Figure 7.3 and Figure 7.4; however Figure 7.6 and Figure 7.7 show the median and mean summed PSD in the Pi1, Pi1/2 and Pi2 ULF wave bands determined for each of the spatial bins illustrated in Figure 7.2. For each station the summed Pi1, Pi1/2 and Pi2 power is calculated and binned with respect to delta latitude and delta longitude of that station during the particular event. The median and mean values of the summed PSD in

each of the Pi1, Pi1/2 and Pi2 band is in turn determined for each of the spatial bins shown in Figure 7.2. Thus, the median and mean sums in the Pi1, Pi1/2 and Pi2 PSD characterise the PSD during a "typical" substorm expansion phase event. This allows the spatial distribution of power to be more readily characterised during a typical or average event; for instance, determining if the three ULF power bands are in fact non-uniformly distributed similar to a Poisson distribution where the mean value can be larger than the median value. Further the spatial ULF power decays in the Pi1, Pi1/2 and Pi2 are more readily quantified when considering the "typical" substorm expansion phase. The spatial power decays provide further insight into whether the three ULF bands are in fact physically disparate.

Figure 7.6 is in the same format as Figure 7.3 and plotted on the same color scale, however the PSD illustrated in Figure 7.6 is the median value of the summed Pi1, Pi1/2 and Pi2 PSD observed during each event in a specific spatial bin. Similar to Figure 7.3, the median summed distributions show a localisation of power near the auroral intensification and additionally clearly show that ULF power is concentrated in the longer period ULF bands in both the H and D magnetic field components. This is also consistent with Figure 7.4. Note that in contrast to the summed median Pi2 spectra shown in Figure 7.3, the median summed Pi2 spectra displays a low amplitude westward localisation of power, in both the H and D components, similar to that observed in Figure 7.4. It is also worth noting that in general the median summed PSD in each of the ULF bands are larger than the summed median PSD. These differences are most likely the result of a typical or median substorm event having a principal ULF wave of a specific frequency which dominates the spectrum, whereas the median spectra has no characteristic ULF wave with preferred frequency in the PSD spectra. This will in general increase the amplitude of the PSD over a discrete frequency range during a median or typical substorm event and thus the median summed power is typically larger than the summed median power which has no preferred frequency or frequency band.

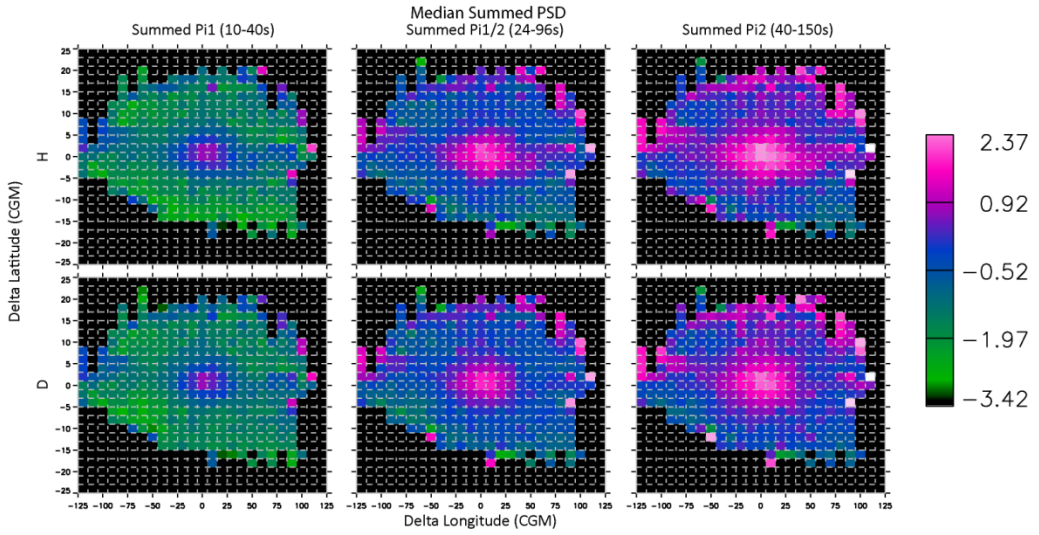

Figure 7.6: The spatial distribution of the logged median summed PSD. The figure is organised in the same format as Figure 7.3 and binned in the same way as Figure 7.2.

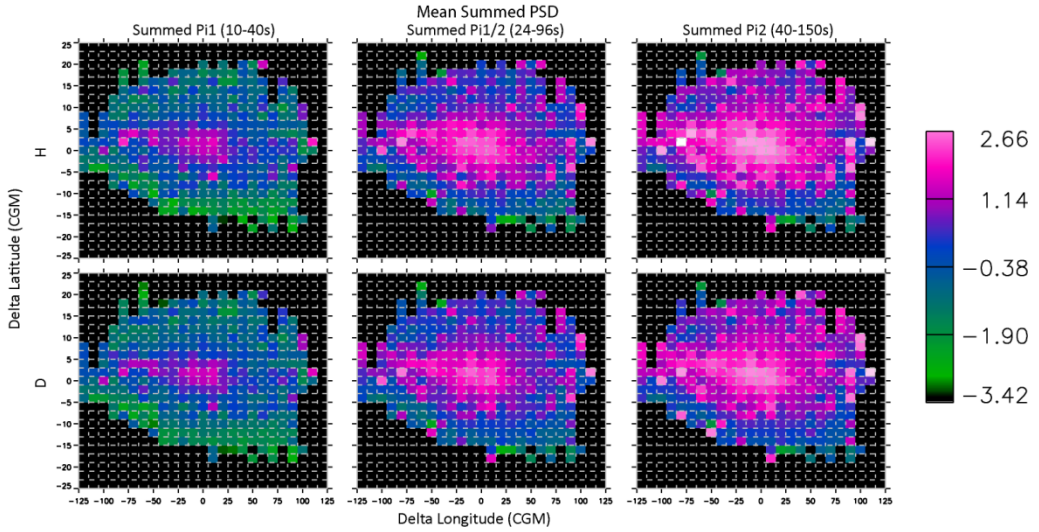

Figure 7.7: The PSD distribution of the logged mean summed PSD, organised in the same format as Figure 7.3.

Figure 7.4 and Figure 7.7 show almost identical distributions the summed mean PSD and mean summed PSD, respectively. The mean summed PSD depicted in Figure 7.7 clearly shows a localisation of ULF wave power in both H and D and in each of the three ULF wave bands near the location of the Frey auroral intensification as well as westward along the latitude approximately defining the auroral intensification. Furthermore, the mean summed PSD in the H component is larger than in the D component. ULF power is

also concentrated in the longer period ULF waves, peaking in the Pi2 band, and is a minimum in the Pi1 band. In the Pi1/2 band the amplitude of the summed mean PSD is larger than that of the Pi1 band and smaller than that of the Pi2 band. This is consistent with the ULF distribution of power illustrated in Figure 7.4 (the summed mean PSD spectra) and the power law spectra depicted in Figure 7.5.

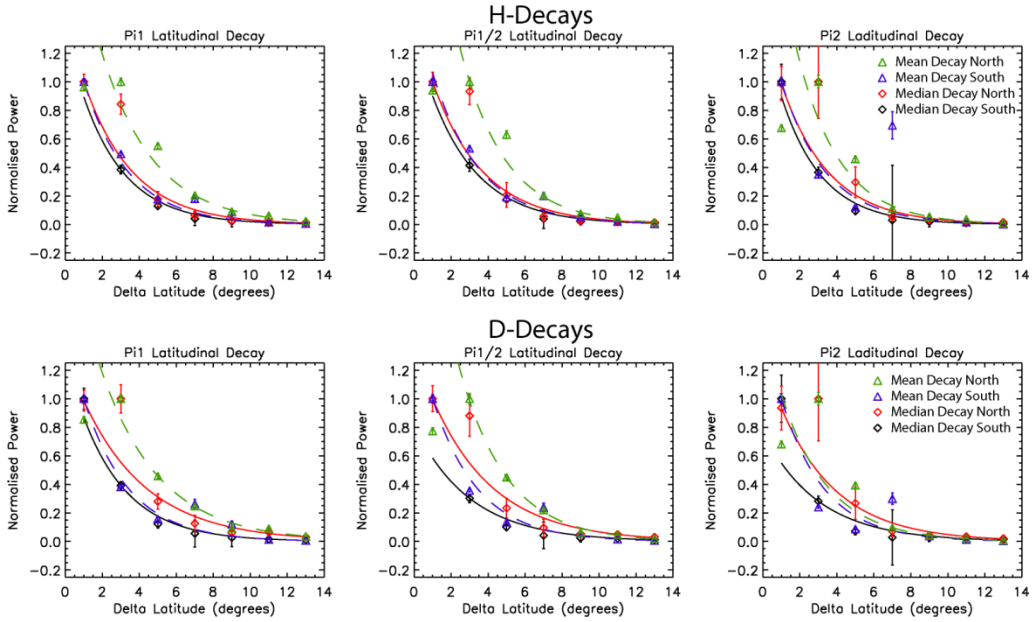

Figure 7.8: The latitudinal decay of mean and median summed PSD as a function of the absolute delta latitude. The y-axis is normalised power and the x-axis absolute delta latitude. Green (blue) diamonds are the mean north (south) PSD and the green (blue) dashed line is the fitted function. Red (black) diamonds are the median north (south) PSD and the solid black (red) line the fitted function. See text for details

We now turn to a quantitative analysis of how the ULF power varies with distance form the Frey auroral onset location. Using the PSD distributions illustrated in Figure 7.6 and Figure 7.7 it is possible to quantify the spatial decay of the Pi1, Pi1/2 and Pi2 ULF power away from the Frey auroral onset location. Figure 7.8 shows the north and south spatial decay of the mean and median summed Pi1, Pi1/2 and Pi2 PSD distributions (left, middle and right panels, respectively) along the meridian characterising the auroral intensification (defined by $|\Delta long|$ < 15 degrees, spanning three bins in delta longitude). Figure 7.8 shows the results from both H and D (upper and lower rows respectively) as a function of the absolute distance in delta latitude ($|\Delta lat\ |$) from the Frey auroral intensification. Note that because three longitudinal bins, centered on the

Frey onset meridian, are used to characterise the latitudinal decay of ULF power the average PSD value over these three longitude bins is plotted in Figure 7.8. At each latitude the error bar represents the average of the standard deviation of the mean in each of the longitudinal bins spanning the aurora intensifications. The mean and median amplitudes in both the north and south directions have further been normalised so that all four PSD profiles can be plotted on the same graph.

In each of three ULF bands the spatial decays of the mean summed power north (green triangles) and south decays (blue triangles) and the median summed power north (red diamonds) and south (black diamonds) are fitted to a curve of the form

$$Qe^{-|\Delta lat|/\Lambda_{lat}}, \tag{7.1}$$

which characterises the spatial decay of summed power with respect to latitude. In equation (7.1), Q is a constant and Λ_{lat} is the e-folding length, in degrees, of the respective PSD with respect to the absolute value of delta latitude away from auroral onset, Δlat. The latitudinal decay length (Λ_{lat}) for both the H and D magnetic field components and the three ULF spectral bands is summarised in Table 7.1. The respective curves are also plotted in Figure 7.8 for reference (see the caption for a description of curves in the legend). The latitudinal decay lengths in both the H and D magnetic field components are remarkably similar, and no significant difference in decay scales is seen between any of the ULF bands. Similarly the north and south decay rates of summed ULF power in general exhibit comparable scale lengths in all three bands.

Table 7.1: Mean and median values of Λ_{lat}, in degrees.

ULF	**Mean**				**Median**			
Band	**H**		**D**		**H**		**D**	
	North	**South**	**North**	**South**	**North**	**South**	**North**	**South**
Pi1	2.31	2.39	2.53	2.32	2.56	2.22	3.04	3.00
Pi1/2	2.44	2.50	2.56	2.44	2.73	2.58	3.32	3.03
Pi2	2.83	2.40	3.17	2.44	2.64	2.37	3.47	2.51

Figure 7.9 shows the longitudinal counterpart to Figure 7.8. Figure 7.9 illustrates the mean east and west (green and blue triangles respectively) and median east and west (red and black diamonds respectively) summed power as a function of the absolute longitudinal distance away from the location of the Frey auroral intensification

($|\Delta long|$). The mean and median values and errors are calculated the same as was those in Figure 7.8, however the averages are of course taken over the three latitudinal bins centered on the auroral intensification, defined by $|\Delta lat|$<3 degrees. Similar to the latitudinal decays shown in Figure 7.8 the longitudinal decays are fitted to a curve characterising the spatial decay of PSD with respect to longitude, Λ_{long}. The longitudinal decay scales are summarised in Table 7.2 and the fitted curves are over plotted in Figure 7.9 (see Figure 7.9 for a legend and description of the curves). In the median summed power both the H and D spatial decays are very similar. In contrast, the spatial decay in the H-component in the mean summed power is slower than in the D-component. In general the mean and median westward spatial decay is slower than the eastward decay. This is in agreement with the additional localisation of power observed westward of the location of the Frey auroral intensification.

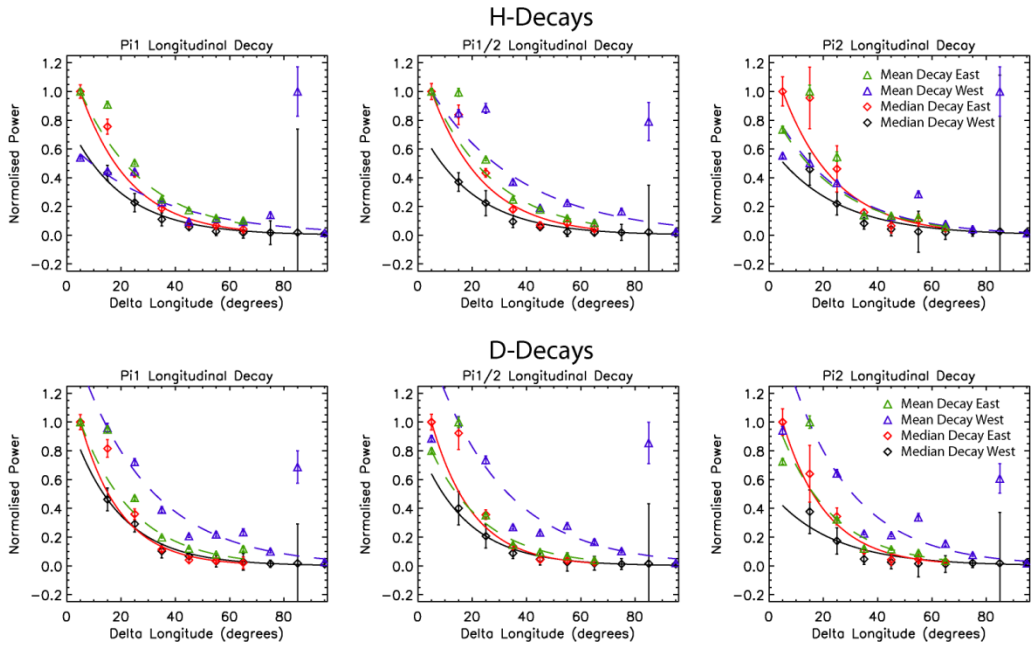

Figure 7.9: The longitudinal decay of summed power as a function of absolute delta longitude. The y-axis is normalised power and the x-axis absolute delta longitude. Green (blue) diamonds are the mean east (west) PSD and the green (blue) dashed line is the fitted function. Red (black) diamonds are the median east (west) PSD and the solid black (red) line the fitted function. See text for details.

Table 7.2: Mean and median values of Λ_{long}, in degrees.

ULF	Mean				Median			
Band	H		D		H		D	
	East	West	East	West	East	West	East	West
Pi1	23.87	24.50	19.49	23.21	23.80	19.81	16.11	22.67
Pi1/2	23.53	33.67	19.97	26.45	20.16	19.12	15.17	17.69
Pi2	23.68	33.39	19.78	26.64	19.72	18.44	14.91	17.84

The localisation of ULF power near auroral onset and along a constant latitude, similar to the latitude defining the auroral onset, as well as the differences between the median and mean spectra suggest that the amplitude ULF power during a magnetic substorm is non-uniformly distributed. Figure 7.11 and Figure 7.12 show the H and D summed Pi1, Pi1/2 and Pi2 (black, blue and red curves respectively) occurrence distribution of power along a cross centered on the latitude and longitude defining the auroral intensification (outlined region of Figure 7.11 and Figure 7.12) as well as select power occurrence distributions away from the cross (outside of the outlined region in Figure 7.11 and Figure 7.12). The location of the cross and each of the histograms is illustrated in Figure 7.10. Each bin is labelled by row and number for reference to the location of the histograms in Figure 7.11 and Figure 7.12. Figure 7.10 also indicates the number of events in each of the spatial bins. The center of the cross is labelled (0,0). Each histogram spans 25 degrees in delta longitude and 4 degrees in delta latitude. Note that these delta latitude and delta longitude bins are larger than the bins used in Figure 7.2. This provides a more accurate representation of the occurrence distributions shown in in Figure 7.11 and Figure 7.12 as each bin has a larger number of events.

Inside of the cross and in each of the three ULF bands there are more events with high-amplitude summed ULF wave power then events with low-amplitude summed ULF wave power. This distribution of the occurrence of power is characteristic of a Poisson distribution where the number of events on either side of the center or peak of the distribution is not equal. In this case, on the high power side of the peak (right of the peak) there are typically more events then on the low power side of the peak (left of the peak). Note this is observed in both the H (Figure 7.11) and D (Figure 7.12) magnetic field components. In general this will lead to the mean of the distribution being larger

the median of the distribution, consistent with Figure 7.3 and Figure 7.4, as well as Figure 7.6 and Figure 7.7.

Outside of the cross, toward the north and south, all three ULF bands show a more uniform distribution. That is on either side of the peak there are a similar number of low and high ULF power events. This is characteristic of both the H and D components, Figure 7.11 and Figure 7.12 respectively. The non-uniform occurrence distributions illustrated in Figure 7.11 and Figure 7.12 suggest that there is a preferential distribution of power near the auroral onset and along the latitude defining auroral onset where ULF wave power, during any given event, is in general observed to have larger values then those further away from the cross. This preferential region of high amplitude ULF wave power is characteristic of the spatial region defining the WTS along the electrojet.

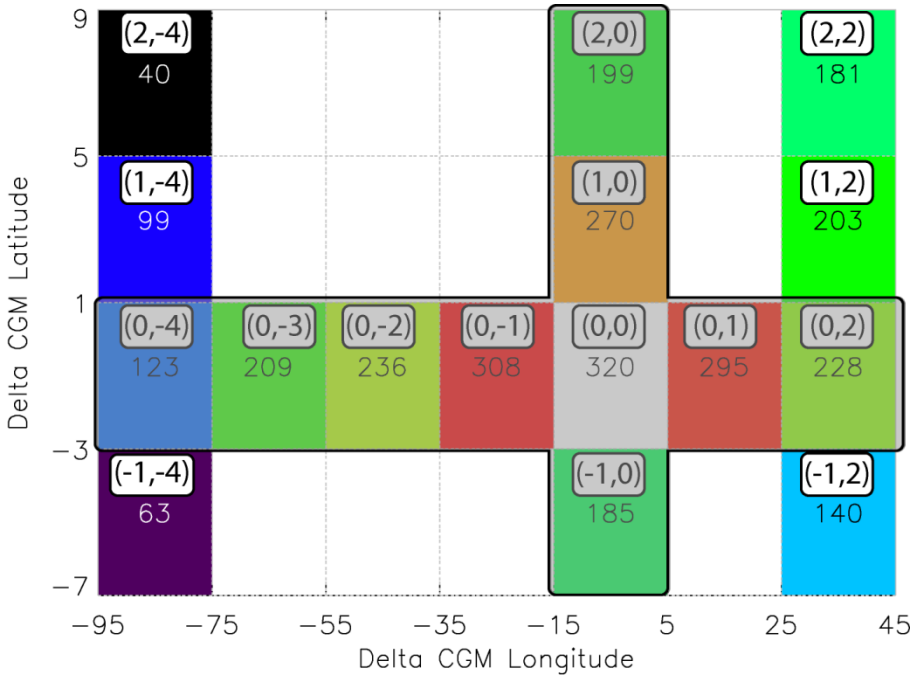

Figure 7.10: The location as well as the number of counts in each of the occurrence distributions shown in Figure 7.11 and Figure 7.12. The coordinates in each bin are for reference to the locations of the histograms in Figure 7.11 and Figure 7.12. The grey highlighted illustrates the region near auroral onset and westward along a constant geomagnetic latitude defining the latitude of the auroral intensification. This highlighted region is referred to as the “cross”.

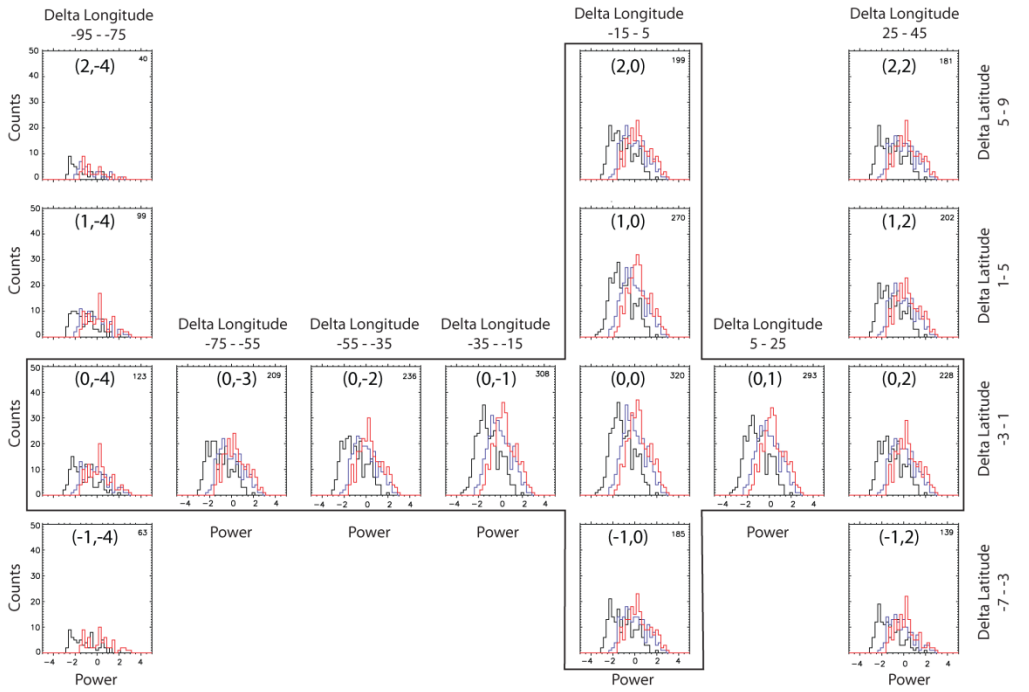

Figure 7.11: H-component occurrence distribution of logged summed Pi1 (black) Pi1/2 (blue) and Pi2 (red) power. The x-axis is the log of power and y-axis the counts in each bin. The total number of counts is illustrated in the top right corner. The coordinates at the center of each histogram depict the location of the histogram in reference to Figure 7.10 and the location of the Frey auroral onset.

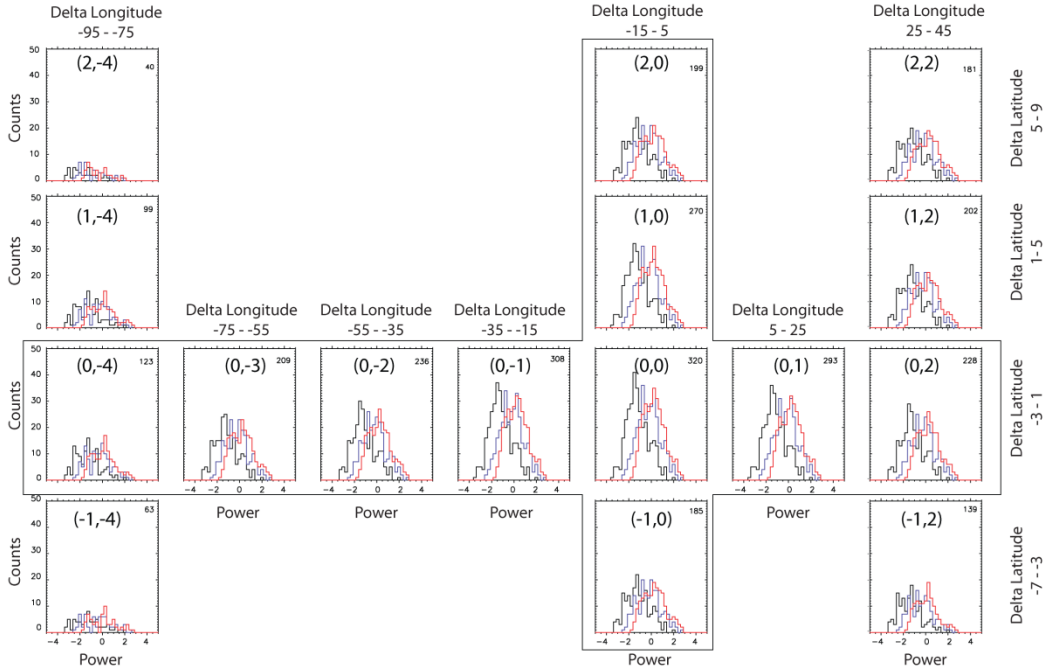

Figure 7.12: D-component distribution of logged summed ULF. Figure is organised the same as Figure 7.11

7.4 Discussion

This Chapter presents a statistical analysis of the spatial distribution of the ULF power in Pi1, Pi1/2 and Pi2 bands spectra observed during auroral substorm expansion phase onsets defined by Frey et al. [*Frey et al.*, 2004; *Wright and Mann*, 2006] and Frey and Mende [*Frey and Mende*, 2006]. Frey et al. [*Frey et al.*, 2004] and Frey and Mende [*Frey and Mende*, 2006] categorized over 4000 substorms with the IMAGE-FUV camera by identifying the time and spatial location of the initial brightening of the auroral oval, characteristic of the onset of the substorm expansion phase. Utilising the Frey substorm database over 800 substorms, spanning approximately five years, were identified which are conjugate with the CARISMA and CANMOS magnetometer arrays. Utilising this subset of conjugate substorms and data from the CARISMA and CANMOS magnetometer arrays a superposed epoch analysis of the ULF spectrum observed in ground-based magnetometers was performed as a function of the relative geomagnetic distance between the observing magnetometer and location of the Frey auroral intensification.

Similar statistical studies of ULF power have been conducted in that past in relation to Pc5 waves [*Mathie and Mann*, 2001; *Pahud et al.*, 2009]. However, in general these studies characterised continuous Pc5 waves (1-10 mHz) and summed ULF power as a function of solar wind [*Mathie and Mann*, 2001] and/or local time [*Pahud et al.*, 2009] rather than in relation to substorm onset. Moreover these studies concentrated on the dayside magnetosphere [*Mathie and Mann*, 2001] or on a band limited frequency range to specifically reduce the effects of magnetic substorms on the statistics of ULF power [*Pahud et al.*, 2009]. Similar to Mathie and Mann [2001] and Pahud et al. [2009] the study in this Chapter analysed summed ULF power distributions. However we concentrate specifically on the impulsive Pi ULF waveforms observed during expansion phase onset. Traditionally, the ULF waves observed during expansion phase onset have been classified by period as either Pi1 (1-40 s) or Pi2 (40-150 s) waves or in terms of their waveform as bursty (PiB) or continuous (PiC) pulsations. In general it is easier to statistically classify ULF waves in respect to their power spectrum. Thus in this study we considered the spatial distributions of summed wave power spanning the Pi1 and Pi2 bands. Note that recent work has also shown that ULF waves spanning both the Pi1 and

Pi2 bands are important for characterising the onset the substorm expansion phase [e.g., *Milling et al.*, 2008; *Murphy et al.*, 2009; *Rae et al.*, 2009a; *Rae et al.*, 2009b]. Thus, we also consider the summed power in the period range of 24-96 s, termed the Pi1/2 band.

Figures 7.3, 7.4, 7.6, 7.7, 7.11 and 7.12 all clearly illustrate that ULF power, in both the H- and D-components and in all three ULF wavebands described above, is strongly localised to the region containing the initial auroral brightening. Rae et al. [2009a; 2009b] have shown that the onset of ULF waves with periods between 24-96 s during expansion phase onset are closely conjugate in both space and time with small-scale auroral features and also with the location of the initial arc brightening observed by ASIs. Similarly, Posch et al. [2007] showed that Pi1B (~10 s periods) pulsations were highly correlated in space and time with the initial brightening identified in the Frey substorm database. Moreover Samson and Harrold [1995] have suggested, through an analysis of the phase velocities of Pi2 waves, that the Pi2 waveforms observed during substorms are likely connected with the initial brightening of the aurora. The results from each of these studies are consistent with the statistical characterisation of the spatial distribution of ULF power observed during the expansion phase onset presented here. Moreover these authors all made similar conclusions relating ULF waves to auroral onset. It is readily apparent in Figure 7.3, 7.4, 7.6 and 7.5 that UFL wave power localised close to the auroral intensification in all three ULF wave bands (Pi1, Pi1/2, and Pi2). This clearly illustrates the relationship of waves in all three bands to substorm expansion phase onset and shows that there is no statistically preferential band.

It is important to note that the localisation of ULF power observed in Figure 7.4 and Figure 7.5 is very similar to the epicentre and expansion of ULF waves observed during a single expansion phase onset as was shown in Chapter 5 [also see, *Milling et al.*, 2008; *Rae et al.*, 2009a; *Rae et al.*, 2009b]. It is possible that the localisation of high-amplitude ULF wave power near the auroral intensification is the spatial counterpart of the temporal expansion of ULF power observed during expansion phase onset, and that the region where ULF waves are first observed in the ionosphere (i.e. conjugate with the auroral onset) is also the region where ULF waves have the highest power. A more detailed study of the temporal evolution of the spatial distribution of ULF power with

respect to the auroral intensification will be required in order to confirm this. However, there is strong evidence to suggest that a correlation exists between the ULF onset and expansion, the auroral onset, and the subsequent total ULF wave power observed during the entire substorm expansion phase.

Figure 7.6 and Figure 7.7 further illustrate that high amplitude ULF power is not only distributed near the auroral surge but also westward along relatively constant latitude. This is also illustrated by Figure 7.9 and Table 7.2, which characterise the longitudinal decay of ULF power, and which clearly demonstrate that the spatial decay of ULF power to the west of the auroral onset occurs more gradually and over larger scales than the decay of ULF power to the east of the Frey location of auroral onset. Figure 7.11 and Figure 7.12 further show that along this westward localisation and near the auroral onset that occurrence distributions of ULF wave power is non-uniformly distributed. Along the highlighted cross in Figure 7.11 and Figure 7.12 the occurrence distribution of ULF power in the Pi1, Pi1/2 and Pi2 bands is characteristic of a Poisson distribution where there are typically more events with high-amplitude ULF wave power than there are events with low-amplitude ULF wave power. Further away from the westward localisation of power and the region characterising the location of the auroral onset the occurrence distribution of ULF wave power becomes increasingly more uniform. That is the number of events with low-amplitude ULF wave power is similar to the number of events which exhibit high-amplitude ULF wave power. This observed in both the H and D magnetic field components and in all three ULF bands. The westward localisation of ULF power observed in Figure 7.6, 7.7, and 7.9 appears to occur in the location where the WTS develops during the expansion phase. Additionally the large number events with high-amplitude ULF wave power, illustrated by the non-uniform occurrence distributions shown in Figure 7.11 and Figure 7.12, along the westward localisation of ULF power is further suggestive that there is a preferential region potentially related to the WTS where ULF wave power is intrinsically large.

One possible scenario which explains the ULF power distribution is the following. An initial and localised disturbance in the magnetosphere triggers the onset of the substorm expansion phase. This initial disturbance maps to a localised region of the ionosphere and auroral oval where the initial auroral intensification, the onset of ULF

waves and subsequently the largest-amplitude ULF wave power is observed. Following onset the SCW develops in the magnetosphere and in the ionosphere and the aurora expands westward forming the WTS. Together the SCW and WTS could be related to the region of high-amplitude ULF wave power which extends westward along the westward electrojet following onset. As mentioned above more work is required to determine if the symmetric spatial distribution of ULF wave power centered on the onset location is related to temporal expansion of ULF power characterised in Chapter 5. Similarly, more work is required in order to determine if the westward expansion of ULF power is related to the SCW and the WTS. This will undoubtedly be a major part of any future research. Significantly it is possible that the westward expansion of ULF wave power which extends along the electrojet is driven by a separate energy release process which produces the WTS.

Figure 7.5 clearly shows that the median and mean ULF spectra observed during the expansion phase onset is characteristic of a power law and potentially a scale-free process. There is no inherent break in spectrum between Pi1 and Pi2 bands and the difference in power observed in the three ULF bands is power-law frequency spectrum. The power law as characterised by both mean and median spectra observed during expansion phase onset, is in general characterised by a slope between -3.2 and -3.6. Moreover the spatial decays shown in Figure 7.8 and Figure 7.9 and summarised in Table 7.1 and Table 7.2 illustrate that the latitudinal and longitudinal decay scales, respectively, in each of the three ULF bands, in both the H and D-components, are also extremely similar. The only appreciable difference is observed in the westward spatial decay rate in the H-component of the magnetic field which shows that the decay of the Pi1/2 and Pi2 band is slower than the westward spatial decay of the Pi1 band. This is in agreement with Posch et al.[2007], who showed that Pi1B waves decayed very quickly as a function of the distance away from the auroral onset region. The similar decay scales observed in each of the three ULF bands, as well as the power-law spectra observed during the expansion phase onset, clearly demonstrate that any sub-classification of Pi waves based on period or frequency, for example Pi1 and Pi2, introduces an arbitrary boundary which appears to have no statistical relevance. Consequently we believe it likely that the energy sources for the Pi1 and pi2 waves are the same, and that waves in the Pi1 and Pi2 share the same driving process.

7.5 Conclusions

ULF waves have been associated with magnetic substorms for over 40 years. In general the ULF waveforms observed during the onset of the substorm expansion phase are impulsive in nature and are typically associated with the initial plasma sheet disturbance during the expansion phase onset. Traditionally these Pi waves have been sub-classified by specific period bands as either Pi1 (1-40 s) or Pi2 (40-150 s) waves [*Jacobs et al.*, 1964], or by using the characteristics of the observed waveform as either a bursty, PiB, or continuous, PiC, pulsation [*Heacock*, 1967]. In this Chapter we have presented the results of a statistical analysis of the ULF power during substorm expansion phase onset. Specifically, ULF power in three frequency bands is characterised as a function of the relative distance away from an auroral intensification identified by the IMAGE-FUV instrument [*Frey et al.*, 2004; *Frey and Mende*, 2006]. We sought to determine whether the Pi1, Pi2 and a Pi1/2 (24-96 s) bands were in fact physically disparate, and whether the traditional definitions of these waves into sub-classifications was is in need of revision.

In this study it has been clearly demonstrated that Ulf waves in the Pi1, Pi2 and Pi1/2 period bands all exhibit a similar spatial distribution of power during the substorm expansion phase. In each of these three bands ULF wave power was observed to be localised near the region of auroral intensification as well as westward of the auroral intensification along the electrojet, in a region of the ionosphere indicative of where the WTS forms. In addition in the region where high-amplitude ULF power is localised, the occurrence distribution of ULF wave power illustrates that in general a magnetometer along a region characteristic of the WTS will observes higher-amplitude ULF wave power than a magnetometer further away from the region characteristic of the WTS. This further suggests that there exists a preferential location characteristic of where the WTS forms along the electrojet.

We have also shown that the Pi1, Pi1/2 and Pi2 bands spatially decay at similar rates in both latitude and longitude. Most notably it has been demonstrated that the mean and median ULF power spectra observed at substorm expansion phase onset is characteristic of a power-law and potentially a scale free process. Statistically, there is no distinguishable break in the power-law spectra at 40 s which separates the Pi1 and Pi2

bands, nor at any other period in the ULF spectra observed during the expansion phase. This is strong evidence that the classification of Pi1 and Pi2 waves by Jacobs et al. [1964] is unnecessary, potentially biasing studies of the ULF spectrum observed during the expansion phase onset by introducing a band separation in spectrum which has no statistical significance. A more appropriate classification may be that proposed by Heacock [1967] which classifies the impulsive ULF waves observed during substorm expansion phase onset as either bursty or continuous pulsations rather than by discrete frequency bands. If the Jacobs et al. [1964] classification of impulsive ULF waves is to continue to be used it must be stressed that both the Pi1 and Pi2 ULF wavebands be taken into account when studying magnetic substorms since there is no statistical reason to differentiate between waves in these two bands as they appear to have an identical and one single continuous morphology.

Chapter 8 Future Work

In this thesis we have highlighted the importance of impulsive ULF waves during magnetic substorms and in particular during expansion phase onset. Specifically we have shown that the automated wavelet estimation of substorm onset and magnetic events (AWESOME) technique described in Chapter 5 offers the capability to provide a high temporal resolution (~20-40 s) diagnosis of the first ionospheric signatures of ULF waves at substorm expansion phase onset, as well as characterise the spatial and temporal onset of these ULF waves on continent scales. The technique has proved to be an excellent means to characterise the ground-based ULF signatures of expansion phase onset but has yet to be thoroughly tested and studied with respect to ULF wave timing of in-situ observations. The physical mechanism responsible for triggering substorm onset is still controversial consequently further studies of substorm expansion phase onset with the AWESOME algorithm incorporating in-situ observations, specifically those from the THEMIS probes, as well as ground-based observations could potentially be used to examine the most likely mechanism for triggering substorm expansion phase onset. Specifically perhaps Pi1 ULF waves can be used to examine both the inside-to-out and outside-to-in hypotheses for substorm onset (c.f. the discussion in Chapter 5)

Further observations of Pi2 waves and BBFs are also required in order to determine if the relation between Pi2 waveforms observed by ground-based magnetometers and large amplitude variations in the plasma velocity, FBs, within a BBF. Specifically, multi-point observations of plasma flows in the magnetosphere could be used to determine the length scales over which small-scale structures, such as FBs, remain coherent within a BBF. Quantifying the spatial scale over which a BBF remains coherent will help to determine whether the most likely relation between BBFs and Pi2s is the directly driven model [*Kepko and Kivelson*, 1999; *Kepko et al.*, 2001] or whether Pi2s and BBF are indirectly related by via magnetic reconnection in the magnetotail or the coupling of fast mode energy with plasma flows and the Earth's magnetic field (such as suggested in the work presented in Chapter 6). The THEMIS mission provides multi-point in-situ observations of the Earth's magnetosphere from five identical satellites. During the tail-season of the THEMIS mission the five probes align in the night-side magnetosphere between distances of ~4-30 R_E. The alignment of the THEMIS probes in the magnetotail

could be used to potentially determine the spatial extent of BBFs in the magnetosphere, the scales which BBF structures remain coherent in the magnetotail, and hence the potential role of BBFs in directly driving Pi2s. The multi-point observations provided by data from the THEMIS probes may be able to determine whether BBFs are able to directly drive Pi2 oscillations or whether the two phenomena are indirectly related, perhaps by a common source in the magnetotail.

Finally there are several ways that the statistical study of ULF power during the expansion phase onset presented in Chapter 7 can be extended. Of most importance is explaining the localisation of ULF power observed near auroral onset and its extension along a localised latitudinal region characteristic of the SCW and WTS. This could be achieved by additionally characterising the very slowly varying magnetic bay fluctuations of both the H- D- and Z-components of the magnetic field during the substorm expansion phase onset. By comparing the statistical background deflections of the Earth's magnetic field to a modeled SCW [e.g., *Cramoysan et al.*, 1995] it may be possible to determine the relationship between SCW bays and the polarisation and power characteristics of Pi1 and Pi2 pulsations. Note that this was done on a case study basis in Chapter 5. Similarly, by utilising the IMAGE-FUV camera it may be possible to characterise the extent to which the aurora expands during each magnetic substorm. This could be used to define statistically the size of the region of expansion of the aurora and size of the WTS during the expansion phase. The ability to characterise the SCW and WTS on a statistical basis will help to confirm whether the localised region of westward extending ULF power is to related to the SCW or WTS, and may explain why there is a preferential location in the ionosphere where ULF power is consistently high. For instance, is the concentration of ULF power correlated with the SCW current system, with auroral phenomenon and the WTS, or possibly with both phenomena? Understanding the physical reason why ULF power is concentrated in a particular region of the ionosphere may also provide insight into the mechanism or mechanisms not only triggering the substorm expansion phase onset, but also for determining more details about the physical processes controlling energy storage and release during substorm, especially those processes mapping to the region of the WTS.

Bibliography

Akasofu, S. I. (1964), The development of the auroral substorm, *Planet. Space Sci.*, 273-282.

Akasofu, S. I., et al. (1965), The polar electrojet, *J. Atmos. Terr. Phys.*, 1275-1305.

Akasofu, S. I. (1977), *Physics of Magnetospheric Substorms*, D. Reidel Publishing Company, Dordrecht.

Alfvén , H. (1942), Existence of electromagnetic-hydrodynamic waves, *Nature*, *150*, 405-406.

Allan, W., and A. N. Wright (1998), Hydromagnetic wave propagation and coupling in a magnetotail waveguide, *J. Geophys. Res.*, *103*, 2359-2368.

Allan, W., and A. N. Wright (2000), Magnetotail waveguide: Fast and Alfvén waves in the plasma sheet boundary layer and lobe, *J. Geophys. Res.*, *105*, 317-328.

Angelopoulos, V., et al. (1992), Bursty Bulk Flows in the Inner Central Plasma Sheet, *J. Geophys. Res.*, *97*(A4), 4027-4039.

Angelopoulos, V., et al. (1994), Statistical Characteristics of Bursty Bulk Flow Events, *J. Geophys. Res.*, *99*, 21257-21280.

Angelopoulos, V. (2008), The THEMIS Mission, *Space Sci. Rev.*, *141*, 4-34.

Angelopoulos, V., et al. (2008), First Results from the THEMIS Mission, *Space Sci. Rev.*, *141*, 453-476.

Auster, H. U., et al. (2008), The THEMIS Fluxgate Magnetometer, *Space Sci. Rev.*, *141*, 235-264.

Baker, D. N., et al. (1996), Neutral line model of substorms: Past results and present view, *J. Geophys. Res.*, *101*(A6), 12975-13010.

Baumjohann, W., et al. (1989), Average plasma properties in the central plasma sheet, *J. Geophys. Res.*, *94*, 6597-6606.

Baumjohann, W., et al. (1990), Characteristics of high-speed ion flows in the plasma sheet, *J. Geophys. Res.*, *95*, 3801-3809.

Baumjohann, W., and R. Treumann (1997), *Basic Space Plasma Physics*, Imperial College Press, London.

Bösinger, T., et al. (1981), Correlation between Pi type magnetic micropulsations, auroras, and equivalent current structures during two isolated substorms, *J. Atmos. Terr. Phys.*, *43*(9), 933-945.

Burton, R. K., and C. T. Russell (1970), The Alfvén Velocity in the Magnetosphere and Its Relationship to ELF Emission, *J. Geophys. Res.*, *75*, 5582-5586.

Carroll, B. W., and D. A. Ostlie (1996), *Modern Astrophysics*, Addison-Wesley Publishing Company.

Chen, F. F. (1984), *Introduction To Plasma Physics and Controlled Fusion, Volume 1: Plasma Physics*, Springer.

Chen, L., and A. Hasegawa (1974), A Theory of Long-Period Magnetic Pulsations 2. Impulse Excitation of Surface Eigenmode, *J. Geophys. Res.*, *79*, 1033-1037.

Chi, P. J., and C. T. Russell (1998), Phase Skipping and Poynting Flux of Continuous Pulsations, *J. Geophys. Res.*, *103*, 29479-29492.

Chi, P. J., et al. (2001), Propagation of the preliminary reverse impulse of sudden commencements to low latitudes, *J. Geophys. Res.*, *106*, 18857-18864.

Clauer, R. C., and R. L. McPherron (1974), Mapping the Local Time-Universal Time Development of Magnetospheric Substorms Using Mid-Latitude Magnetic Observations, *J. Geophys. Res.*, 2811-2820.

Cramoysan, M., et al. (1995), The use of a model current wedge in the determination of the position of substorm current systems, *Ann. Geophys.*, *13*, 583-594.

Daubechies, I. (1988), Orthonormal bases of compactly supported wavelets, *Commun. Pure Appl. Math.*, *41*, 909-996.

Donovan, E. F., et al. (2006), The azimuthal evolution of the substorm expansive phase onset aurora, *Proceeding of ICS8*, 55-60.

Dungey, J. W. (1961), Interplanetary magnetic field and the auroral zones, *Phys. Rev. Lett.*, 47-48.

Frank, L. A., et al. (1994), The Comprehensive Plasma Instrumentation (CPI) for the Geotail spacecraft, *J. of Geomag. Geoelect.*, *46*, 23-37.

Frey, H. U., et al. (2004), Substorm onset observations by IMAGE-FUV, *J. Geophys. Res.*, *109*.

Frey, H. U., and S. B. Mende (2006), Substorm onsets as observed by IMAGE-FUV, *Proceeding of ICS8*, 71-75.

Gurnett, D. A., and A. Bhattacharjee (2005), *Introduction to plasma physics: with space and laboratory applications*, Cambridge University Press.

Haerendel, G. (1992), Disruption, ballooning or auroral avalanche: On the cause of substorms, *Proceeding of ICS1*, 417-420.

Heacock, R. R. (1967), Two Subtypes of Type Pi Micropulsations, *J. Geophys. Res.*, *72*, 3905-3917.

Huba, J. D., et al. (1977), The lower-hybrid-drift instability as a source of anomalous resistivity for magnetic field line reconnection, *Geophys. Res. Lett.*, *4*, 125-128.

Jacobs, J. A., et al. (1964), Classification of Geomagnetic Micropulsations, *J. Geophys. Res.*, *69*(1), 180-181.

Kepko, L., and M. G. Kivelson (1999), Generation of Pi2 pulsations by bursty bulk flows, *J. Geophys. Res.*, *104*, 25021-25034.

Kepko, L., et al. (2001), Flow bursts, braking, and Pi2 pulsations, *J. Geophys. Res.*, *106*, 1903-1915.

Kisabeth, J. L., and G. Rostoker (1977), Modelling of 3-dimensional current systems associated with magnetospheric substorms, *Geophys. J. R. Astron. Soc.*, *49*(3), 655-683.

Kivelson, M. G., and C. T. Russell (1995), *Introduction to Space Physics*, Cambridge University Press, Cambridge.

Kokubun, S., et al. (1994), The GEOTAIL Magnetic Field Experiment, *J. of Geomag. Geoelect.*, *46*, 7-21.

Lessard, M. R., et al. (2006), Nature of Pi1B pulsations as inferred from ground and satellite observations, *Geophys. Res. Lett.*, *33*.

Lester, M. R., et al. (1983), Polarization patterns of Pi 2 magnetic pulsations and the substorm current wedge, *J. Geophys. Res.*, *88*, 7958-7966.

Liang, J., et al. (2008), Intensification of preexisting auroral arc at substorm expansion phase onset: Wave-like disruption during the first tens of seconds, *Geophys. Res. Lett.*, *35*(L17S19).

Lui, A. T. Y., et al. (1995), Preliminary nonlocal analysis of cross-field current instability for substorm expansion onset, *J. Geophys. Res.*, *100*, 19147-19154.

Lui, A. T. Y. (1996), Current disruption in the Earth's magnetosphere: Observations and models, *J. Geophys. Res.*, *101*, 13067-13088.

Lyons, L. R. (1995), A new theory for magnetospheric substorms, *J. Geophys. Res.*, *100*, 19147-19154.

Lysak, R. L. (1988), Theory of Auroral Zone PiB Pulsation Spectra, *J. Geophys. Res.*, *93*, 5942-5946.

Mann, I. R., et al. (1999), Excitation of magnetospheric waveguide modes by magnetosheath flows, *J. Geophys. Res.*, *104*, 333-353.

Mann, I. R., et al. (2008), The Upgraded CARISMA Magnetometer Array in the THEMIS Era, *Space Sci. Rev.*, *141*, 413-451.

Mathie, R. A., and I. R. Mann (2000), Observations of Pc5 field line resonance azimuthal phase speeds: A diagnostic of their excitation mechanism, *J. Geophys. Res.*, *105*, 10713-10728.

Mathie, R. A., and I. R. Mann (2001), On the solar wind control of Pc5 ULF pulsations power at mid-latitudes: implications for MeV electron acceleration in the outer radiation belt, *J. Geophys. Res.*, *106*, 29783-29796.

McPherron, R. L. (1970), Growth Phase of Magnetospheric Substorms, *J. Geophys. Res.*, 5592-5599.

McPherron, R. L. (1979), Magnetospheric Substorms, *Rev. Geophys. Space Phys.*, *17*, 657-681.

Mende, S. B., et al. (2000), Far Ultraviolet Imaging from the Image Spacecraft. 1. System Design, *Space Sci. Rev.*, *91*, 243-270.

Meyer, Y. (1989), Orthonormal Wavelets, in *Wavelets*, edited by J. M. Combes, et al., Springer, Berlin.

Mier-Jedrzejowicz, W. A. C., and W. J. Hughes (1980), Phase Skipping and Packet Structure in Geomagnetic Pulsation Signals, *J. Geophys. Res.*, *85*, 6888-6892.

Milling, D. K., et al. (2008), Ionospheric localisation and expansion of long-period Pi1 pulsations at substorm onset, *Geophys. Res. Lett.*, *35*(L17S20).

Mukai, T., et al. (1994), The low energy particle (LEP) experiment onboard the Geotail satellite, *J. of Geomag. Geoelect.*, *46*, 669-692.

Murphy, K. R., et al. (2009), Wavelet-based ULF wave diagnosis of substorm expansion phase onset, *J. Geophys. Res.*, *114*.

Nose, M., et al. (1998), Automated detection of Pi 2 pulsations using wavelet analysis: 1. Method and application for substorm monitoring, *Earth Planets Space*, *50*, 773-783.

Olson, J. V. (1999), Pi2 Pulsations and substorm onsets: A review, *J. Geophys. Res.*, *104*, 17499-17520.

Østgaard, N., et al. (2004), Interplanetary magnetic field control of the location of substorm onset and auroral features in the conjugate hemispheres, *J. Geophys. Res.*, *109*.

Østgaard, N., et al. (2006), Auroral conjugacy studies based on global imaging, *J. Atmos. Sol. Terr. Phys.*, *69*(3), 249-255.

Pahud, D. M., et al. (2009), Ground-based Pc5 ULF wave Power: Solar wind speed and MLT dependence, *J. Atmos. Sol. Terr. Phys.*, *71*, 1082-1092.

Parker, E. N. (1958), Dynamics of the interplanetary gas and magnetic fields, *Astrophysical Journal*, 664-676.

Petrukovich, A. A., and A. G. Yahnin (2006), The substorm onset location controversy, *Space Sci. Rev.*, *122*, 81-87.

Posch, J. L., et al. (2007), Statistical observations of spatial characteristics of Pi1B pulsations, *J. Atmos. Terr. Phys.*, *69*(15), 1775-1796.

Press, W. H., et al. (1992), *Numerical Recipes in C: The Art of Scientific Computing Second Edition* Cambridge University Press.

Rae, I. J., et al. (2005), Evolution and characteristics of global Pc5 ULF waves during a high solar wind speed interval, *J. Geophys. Res.*, *110*(A12211).

Rae, I. J., et al. (2006), Pi2 pulsations: Field Line resonances of a Driven Response, *Proceeding of ICS8*, 253-258.

Rae, I. J., et al. (2009a), Near-Earth Initiation of a Terrestrial Substorm, *J. Geophys. Res.*, doi:10.1029/2008JA013771.

Rae, I. J., et al. (2009b), Timing and localization of ionospheric signatures associated with substorm expansion phase onset, *J. Geophys. Res.*, *114*(A00C09).

Raj, A., et al. (2002), Wind survey of high-speed bulk flows and field-aligned beams in the near-Earth plasma sheet, *J. Geophys. Res.*, *107*.

Rostoker, G., et al. (1995), Canopus - A ground-based instrument array for remotes sensing the high latitude ionosphere during the ISTP/GGS program, *Space Sci. Rev.*, *41*, 743-760.

Roux, A., et al. (1991), Plasma sheet instability related to the westward travelling surge, *J. Geophys. Res.*, *96*, 17697-17714.

Russell, C. T., and R. L. McPherron (1973), The Magnetotail and Substorms, *Space Sci. Rev.*, *15*, 205-266.

Russell, C. T., et al. (2008), THEMIS Ground-based Magnetometers, *Space Sci. Rev.*, *141*, 389-412.

Saito, T. (1969), Geomagnetic Pulsations, *Space Sci. Rev.*, *10*, 319-412.

Saito, T., et al. (1976), Mechanism of association between Pi2 pulsation and magnetospheric substorm, *J. Atmos. Terr. Phys.*, *38*, 1265-1277.

Samson, J. C., et al. (1971), Latitude-Dependent Characteristics of Long-Period Geomagnetic Micropulsations, *J. Geophys. Res.*, *76*, 3675-3683.

Samson, J. C., and G. Harrold (1995), Characteristic time constants and velocities of high-latitude Pi2s, *J. Geophys. Res.*, *90*(NA12), 2173-2181.

Shiokawa, K., et al. (1997), Braking of high-speed flows in the near-Earth tail, *Geophys. Res. Lett.*, *24*, 1179-1182.

Shiokawa, K., et al. (1998), High-speed ion flow, substorm current wedge, and multiple Pi2 pulsations, *J. Geophys. Res.*, *103*(A3), 4491-4507.

Shumway, R. H., and D. S. Stoffer (2006), *Time Series Analysis and Its Applications: Second Edition*, Springer, New York.

Smith, A. J., et al. (2002), VLF, magnetic bay, and Pi2 substorm signatures at auroral and midlatitude ground stations, *J. Geophys. Res.*, *107*(A12).

Southwood, D. J. (1974), Some Features of Field Line Resonances in the Magnetosphere, *Planet. Space Sci.*, *22*, 483-491.

Sutcliffe, P. R., and K. Yumoto (1991), On the Cavity Mode Nature of Low-Latitude Pi 2 Pulsations, *J. Geophys. Res.*, *96*(1543-1551).

Tamao, T. (1964), The structure of three-dimensional hydromagnetic waves in a uniform cold plasma, *J. Geomag. Geoelectr.*, *18*, 89-114.

Tsyganenko, N. A. (1989), A magnetospheric magnetic field model with a warped tail current sheet, *Planet Space Sci.*, *37*, 5-20.

Tsyganenko, N. A. (1995), Modeling the Earths magnetospheric magnetic-field confined within a realistic magnetopause, *J. Geophys. Res.*, *100*(A4), 5599-5612.

Uozumi, T., et al. (2000), Characteristics of Energy Transfer of Pi 2 Magnetic Pulsations: Latitudinal Dependence, *Geophys. Res. Lett.*, *27*, 1619-1622.

Vasyliunas, V. M. (1970), Mathematical models of magnetospheric convection and its coupling to the ionosphere, in *Particles and Fields in the Magnetosphere*, edited by B. M. McCormac and D. Reidel, pp. 60-71, Norwell Mass.

Voronkov, I. O., et al. (2003), Observations of the phases of the substorm, *J. Geophys. Res.*, *108*(A2).

Waters, C. L. (2000), ULF Resonance Structure in the Magnetosphere, *Adv. Space Res.*, *25*, 1541-1558.

Wright, A. N., et al. (1999), Phase mixing and phase motion of Alfvén wave on tail-like and dipole-like magnetic field lines *J. Geophys. Res.*, *104*, 10159.

Wright, A. N., and I. R. Mann (2006), Global MHD Eigenmodes of the Outer Magnetosphere, in *Magnetospheric ULF Waves, Synthesis and New Directions*, edited by K. Takahashi, et al., pp. 51-72.

Yeoman, T. K., 7, and D. Orr (1989), Phase and spectral power of mid-latitude Pi2pulsations: Evidence for a plasmaspheric cavity resonance, *Planet Space Sci.*, *37*, 1367-1383.